Surface wear reduction of bulk solids handling equipment using bionic design

Chen, Guangming

DOI
10.4233/uuid:b60cb231-222d-434d-b987-cf36605bc719

Publication date
2017

Document Version
Final published version

Citation (APA)
Chen, G. (2017). *Surface wear reduction of bulk solids handling equipment using bionic design*. [Dissertation (TU Delft), Delft University of Technology]. TRAIL Research School. https://doi.org/10.4233/uuid:b60cb231-222d-434d-b987-cf36605bc719

Important note
To cite this publication, please use the final published version (if applicable).
Please check the document version above.

Surface Wear Reduction of Bulk Solids Handling Equipment Using Bionic Design

Proefschrift

ter verkrijging van de graad van doctor
aan de Technische Universiteit Delft,
op gezag van de Rector Magnificus prof. ir. K. C. A. M. Luyben,
voorzitter van het College voor Promoties,
in het openbaar te verdedigen op

dinsdag 27 juni 2017 om 10:00 uur

door

Guangming CHEN

Master of Engineering in Agricultural Mechanization Engineering,
Jilin University, China

geboren te Wuyang, Henan, China

Dit proefschrift is goedgekeurd door de promotor:
Prof. dr. ir. G. Lodewijks

en copromotor:
Dr. ir. D. L. Schott

Samenstelling promotiecommisie:

Rector Magnificus,	voorzitter
Prof. dr. ir. G. Lodewijks,	Technische Universiteit Delft, promotor
Dr. ir. D. L. Schott,	Technische Universiteit Delft, copromotor

onafhankelijke leden:

Prof. dr. J. Li,	Jilin University (China)
Prof. dr. ing. A. Katterfeld,	Otto-von-Guericke-Universität Magdeburg (Germany)
Prof. dr. P. C. Rem,	Technische Universiteit Delft
Prof. dr. ir. P. Breedveld,	Technische Universiteit Delft
Dr. C. Wheeler,	University of Newcastle (Australia)

Summary

Bulk solids handling continues to play an important role in a number of industries. One of the issues during bulk solids handling processes is equipment surface wear. Wear results in high economic loss and increases downtime. Current wear reduction methods such as optimizing transfer conditions or using wear-resistant materials, have brought notable progress. Nevertheless, the wear loss is still significant. Therefore, new solutions for reducing the surface wear must be investigated.

Because wear also occurs to the surfaces of many biological organisms, inspirations for wear reduction can be obtained from biology. In this research, the bionic design method is explored to reduce the surface wear of bulk solids handling equipment.

This thesis firstly illustrates the analytical wear models in bulks solids handling. Hence, the wear phenomena in biology are investigated. Based on the analogies between biology and bulk solids handling, a bionic design method for wear reduction of bulk solids handling equipment surfaces is developed. Furthermore, two bionic models for reducing abrasive and erosive wear respectively, are proposed for the applications of bulk solids handling equipment surfaces.

To model the effects of applying bionic models on the surface wear of bulk solids handling equipment, the discrete element method (DEM) is utilized. Using the parameter values obtained from experiments, the wear of bionic surfaces and conventional smooth surfaces is successfully modeled.

By comparing predicted wear loss from bionic surfaces and smooth surfaces, the effectiveness of reducing wear by application of bionic models are successfully demonstrated. Moreover, parametric studies on geometrical parameters of bionic models were also carried out. The results demonstrate that as biological wear reduction mechanisms are implemented, wear reduction of bulk solids handling equipment surfaces can be achieved. It is shown that abrasive wear loss can be reduced by up to 63% whilst erosive wear loss can be reduced by up to 26%.

Samenvatting

In verschillende industrieën neemt bulk solids handling een zeer prominente rol in. Een van de belangrijkste knelpunten gedurende het proces is de slijtage op het transporterende oppervlak van het apparaat. De gevolgen hiervan zijn grote economische verliezen en dat het apparaat uit roulatie gehaald moet worden voor een bepaald tijdsperiode. De huidige slijtage verminderings methoden zoals geoptimalisereerde overslag condities of gebruikmaken van slijtage werende materialen hebben er niet toe geleid dat het benodigde verschil in slijtage vermindering te merken is. Vandaar dat er onderzoek nodig is naar nieuwe oplossingen die oppervlakslijtage verder significant kunnen reduceren.

Omdat bij vele biologische organismen slijtage aan het oppervlak voorkomt, kan er inspiratie getrokken wordt uit de biologie om dit te verminderen. In dit onderzoek worden ontwerp methode van de biotechniek onderzocht om de slijtage van de Bulk Solids handeling werktuigen te verminderen.

Mijn scriptie belicht in het begin de analytische slijtage modellen aan in bulk solids handling. Daarna word het fenomeen slijtage in de biologie onderzocht. Op basis van overeenkomsten tussen biologie en bulk solids handling is het ontwerpmethode voor slijtage reductie aan het oppervlak van bulk solids handling apparaten ontwikkeld. Verder worden twee biotechniek modellen voorgedragen voor vermindering van respectievelijk de schuur - en de erosieve slijtage op het oppervlak van bulk handling apparaten.

Discrete Element Method (DEM) van biotechniek modellen modelleert de effecten die voortkomen uit slijtage aan het oppervlak van de bulk solids handling. De parameter waarden verkregen uit experimenten worden succesvol gemodelleerd in de slijtage van de biotechniek en de conventionele gladde oppervlakken.

Door het slijtage verlies van biotechniek en gladde oppervlakken met elkaar te verge-lijken, wordt de geschiktheid van de toepassing van biotechniek succesvol aangetoond. Verder werden studies uitgevoerd op geometrische parameters van

modellen uit de biotechnoloogie. De resultaten laten zien dat slijtage aan op-
pervalakken van bulk solids handling apparatuur kan worden gereduceerd door
toepassing van mechanismen van slijtagevermindering uit de biologie. Uit de
verkregen resultaten volgt dat een reductie van 63% voor schuur-slijtage en 26%
voor erosieve slijtage kan worden bereikt.

Contents

1 | CHAPTER

Introduction

1.1 Background

Bulk solids handling consists of the transportation, transfer, transshipment, and storage of various amounts of particulate solids (e.g. powders and grains) [1]. Bulk solids handling plays an important role in a range of industries, such as the agricultural, chemical and mining industries.

In the mining industry, for example, iron ore is exploited intensively to supply the base material for steel productions. Figure 1.1 depicts a part of an iron ore handling process by using a belt conveyor at Kolomela mine [2]. Driven by economic growth, the demand of iron ore continues to increase [3], resulting in a large-scale iron ore handling industry.

Figure 1.1: Handling of iron ore using a belt conveyor at Kolomela mine [2].

On account of the abrasive nature of the particulate solids such as iron ore, large-scale handling commonly causes high wear on the surfaces of handling equipment. Several locations of heavy wear are found on, for instances, silo walls and chute bottoms [4]. Wear causes volume loss from the surfaces of handling equipment and consequently accelerates the damage of equipment. The maintenance

of wear areas not only introduces high economic cost, but also increases the down time. To save economic cost and reduce downtime, the surface wear of bulk solids handling equipment must be reduced.

Several methods are applied to reduce the surface wear. For instance, optimizing chute profiles based on analytical predictions of their wear rates [4]. Another example is applying wear-resistant materials to the wearing surfaces [5]. However, wear reduction is still insufficient and high wear rate is a big issue especially considering the expansion of bulk solids handling industry. To further reduce the surface wear, a new solution need to be investigated.

Due to the fact that wear also occurs to the surfaces of many biological organisms, inspiration for wear reduction can be obtained from biology. This is because, as a result of evolution, biological organisms can minimize their surface wear to cope with their living environments. Thus far, scientists have discovered several surface morphologies (e.g. convexes [6], ribs [7] and scales [8]) that can achieve lower wear rates compared to engineering smooth surfaces [9–11].

Figure 1.2 (a) shows a scale morphology from a desert snake body surface [8]. Figure 1.2 (b) presents a bio-inspired scale-like engineering steel surface [11]. Experimental tests demonstrate that the scale-like surface can reduce dry sliding friction forces by more than 40% in comparison to an untextured smooth surface [11]. As a result of friction force reduction, a reduction of surface wear can also be achieved.
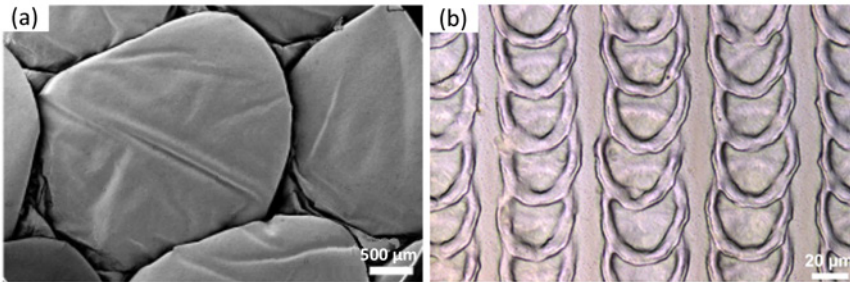
Figure 1.2: A bio-inspired morphology for friction and wear reduction (a) scales of a desert snake [8] (b) a fabricated scale-like surface [11].

To apply a biologically morphological effect to industry, the bionic design [12, 13] method can be used. Bionic design is also called biomimetic design [14], bio-inspired design [15] or biomimicry [16], which is used for transferring a biological function to an industrial product [10, 17, 18].

In the field of particulate solids interacting with equipment, bionic design was firstly used by Ren et al. [6] for soil resistance reduction. In their research [6, 19], the convex morphology on the head of a dung beetle was applied to the surface of an agricultural instrument. Results showed that resistance is reduced by 13% on average. Bulk solids handling industry has similarities with agricultural industry. Nevertheless, bionic design has not yet been introduced to bulk solids handling.

1.2   Research objective

This research is to investigate the ability of surface wear reduction of bulk solids handling equipment using bionic design. By this research, the wear reduction mechanisms from biological morphologies will be identified. Besides, a bionic design method for surface wear reduction of bulk solids handling equipment will be developed. Using this bionic design method, the bionic models of lower wear rates will be proposed and the wear reduction abilities corresponding to the bionic surfaces will be demonstrated. In addition, a range of parameter values of the bionic models for wear reduction of bulk solids handling equipment will be obtained.

1.3   Problem statement

As severe wear occurs to the surfaces of bulk solids handling equipment, bionic design will be investigated to transfer the morphological effect of wear reduction to the surfaces of bulk solids handling equipment.

However, from biology to bulk solids handling, the wear characteristics vary in three aspects: particulate solids, worn surface and wear conditions. Therefore, a superficial copy of a biological morphology to an engineering surface is not usually satisfying, cf. Vincent's [14] warning:

"The transfer of a concept or mechanism from living to nonliving systems is not trivial. A simple and direct replica of the biological prototype is rarely successful, even if it is possible with current technology" [14].

In particular, the scales of biologically functional morphologies are of high deviations from those in bulk solids handling. In general, the size ranges in biology are nanometers to millimeters. By contrast, the ranges are generally in centimeters and meters for bulk solids handling equipment. Therefore, extending morphological effects from biological scales to industrial levels is another challenge [20].

1.4   Research questions

In order to reduce the surface wear of bulk solids handling equipment, the main question is formulated as follows:

   Can bionic design reduce surface wear of bulk solids handling equipment?

To answer the main research question, six key subquestions are derived:

(1) Which analytical wear models can be used to quantify the surface wear of bulk solids handling equipment?

(2) How to develop a bionic design method to reduce the surface wear of bulk solids handling equipment?

(3) What experiments can be used to determine the DEM parameters for modeling wear in bulk solids handling?

(4) How to predict the surface wear of bulk solids handling equipment by using the DEM simulations?

(5) What are the effects of applying bionic surfaces on abrasive wear reduction?

(6) What are the effects of applying bionic surfaces on erosive wear reduction?

1.5 Outline of thesis

Based on the above six subquestions, the structure of this thesis is organized as follows.

Chapter 2 presents a literature review study on the analytical wear models in bulk solids handling. It elaborates two main wear types, namely, abrasive and erosive wear. Using the analytical wear models, examples to quantify abrasive and erosive wear are provided.

Chapter 3 describes a bionic design method for surface wear reduction of bulk solids handling equipment. Based on this bionic design method, two bionic models for reducing abrasive and erosive wear are proposed.

In **Chapter 4**, experimental studies for evaluating wear parameters are provided. This chapter illustrates three experimental tests, which are hardness test, pin-on-disk wear test and inclining surface test.

Chapter 5 illustrates the verifications of two DEM simulation models for predicting wear by single particle, namely, particle sliding wear and particle impact wear. These two models will be respectively used for modeling abrasive wear and erosive wear.

Chapter 6 provides abrasive wear predictions on bionic surfaces of a bulk solids handling equipment subjected to a set of sizes of a bionic model. For comparison, the abrasive wear prediction for a conventional smooth surface is also included.

Chapter 7 gives erosive wear predictions on bionic surfaces of a bulk solids handling equipment with regard to a range of sizes of a bionic model. This chapter also provides the erosive wear prediction of a smooth surface.

Finally, **Chapter 8** summaries the conclusions and gives recommendations for future work.

The organization of this thesis is also represented in Figure 1.3.

Introduction
Chapter 1

Analytical wear models in
bulk solids handling
abrasive wear, erosive wear
Chapter 2

Bionic design method for
wear reduction in bulk
solids handling
bionic models for wear reduction
Chapter 3

Experimental studies for
determinations of DEM
parameters
hardness test, wear test, inclining test
Chapter 4

Verification of wear
prediction by the discrete
element method
sliding wear, impact wear
Chapter 5

Abrasive wear reduction of
bulk solids handling
equipment surfaces
bionic design for abrasive wear reduction
Chapter 6

Erosive wear reduction of
bulk solids handling
equipment surfaces
bionic design for erosive wear reduction
Chapter 7

Conclusions and
recommendations
Chapter 8

Figure 1.3: Outline of thesis.

2 | CHAPTER

Analytical wear models in bulk solids handling

$\mathbf{A}$s was introduced by Chapter 1, analytical wear models are used to quantify the surface wear of bulk solids handling equipment. Previous research provided basic equations for estimating wear in bulk solids handling. Nevertheless, it is still difficult to select appropriate wear models to quantify wear under bulk solids handling conditions. Therefore, to effectively predict wear, a comprehensive analysis on the available analytical wear models must be carried out.

This chapter presents a comprehensive study on the analytical wear models in bulk solids handling. It includes the most relevant wear equations and wear test apparatus. This chapter is composed of seven sections. Section 2.1 describes wear characteristics from three aspects of particulate solids, equipment surface and wear conditions. Section 2.2 presents wear mechanisms for abrasive wear and erosive wear. Section 2.3 illustrates wear equations with respect to ductile and brittle surfaces. In section 2.4, examples of wear estimation are illustrated. In section 2.5, the most commonly used wear test apparatus are compared. The limitations on the prediction of wear in bulk solids handing are discussed in section 2.6. Finally, conclusions are given in section 2.7.

2.1 Wear aspects in bulk solids handling

This research focuses on the mechanical wear caused by relative movements between bulk solids and equipment surfaces. Categorizing wear aspects is used to define wear types and understand wear mechanisms. To overview the wear aspects in bulk solids handling, three aspects, namely, particulate solids, equipment surface and wear conditions [21] are described.

2.1.1   Particulate solids

A bulk solid material consists of any number of discrete particulate solids or particles. The individual particles are either in contact or near contact with their immediate neighbors [1]. The following seven particle characteristics affect wear.

(1) Particle size and particle size distribution: Particles can be fines or lumps. The wear rates can vary by different particle size distributions [22]. Figure 2.1 shows a sample of Sishen iron ore bulk solids and its particle size distribution.

(a)   (b)
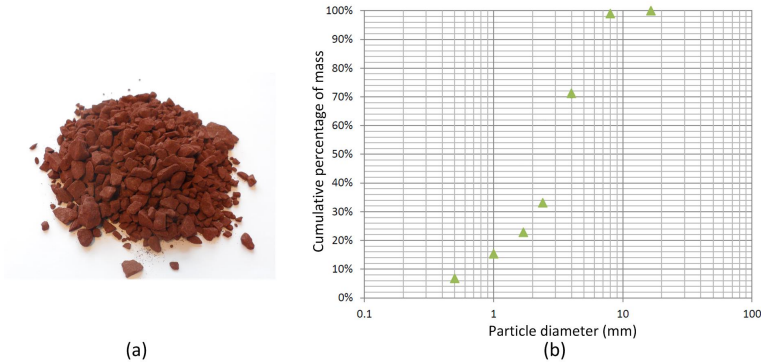
Figure 2.1: A sample of bulk solids (a) Sishen iron ore (b) particle size distribution [23]

(2) Particle shapes: The shape of a particle can be spherical, ellipsoidal or irregular. Particle shape affects the deformation of equipment surface [24] and thus affects wear [25].

(3) Velocity: Particle can have a translational and also a rotational motion. The velocity of particles affect impact energy and contact orientation of bulk solids in regard to equipment surface [26].

(4) Density: The density of particle or bulk solids affects contact force and impact energy with respect to equipment surface [27].

(5) Particle hardness: Hardness means the ability of a surface resisting the deformations subjected to loads applied on an indenter [28]. During particle indentation, an equipment surface is deformed when the hardness ratio of particle to equipment surface $H_p > 1.2H_e$ [28] (Figure 2.2).

(6) Particle frangibility: Brittle particles can fracture or fragment when the applied force exceeds a critical level [29, 30].

(7) Particle surface roughness: Particle surface roughness affects profiles of contact in regard to an equipment surface [28]. It is also noted that the surface roughness degrades as a result of mechanical interactions with equipment surface [31].
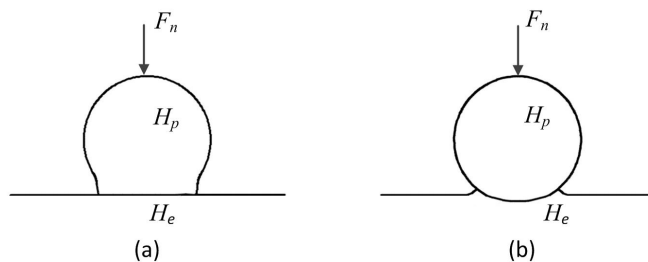
Figure 2.2: Critical hardness ratio (a) $H_p/H_e \leq 1.2$ (b) $H_p/H_e > 1.2$

2.1.2 Equipment surface

For assessing wear, the surface materials of bulk solids handling equipment are assumed to be either ductile or brittle [32], which are referred to as ductile surface or brittle surface in this research. The following five characteristics from equipment surface affect wear.

(1) Surface ductility or toughness: Under increasing normal forces, ductile surface materials undergo elastic and plastic deformations, whereas brittle surface materials mainly suffer from plastic deformation and fracture [24, 28]. Figure 2.3 illustrates the indentation response for a ductile surface material using a spherical indenter [33]. Figure 2.4 schematics the formations of plastic deformation (P), median (M) and lateral (L) cracks on a brittle surface by a sharp indenter (i.e. point load) [34].
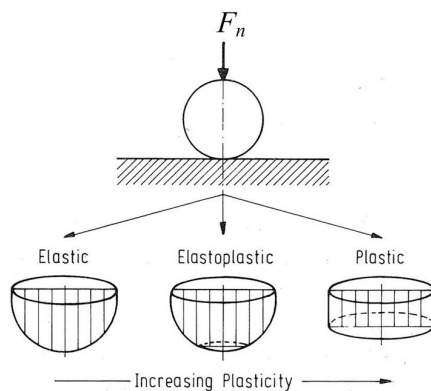
Figure 2.3: Schematic illustration for indentations by a spherical indenter [33]

(2) Surface roughness: The surfaces of equipment are not ideally smooth or flat. Thus realistic contacts between particle and equipment surface occur via asperities [35, 36].
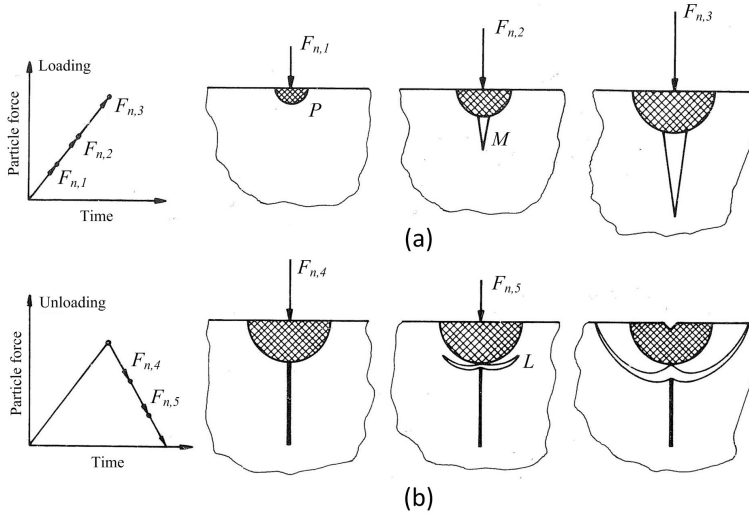
Figure 2.4: Responses of a brittle surface indented by a sharp indenter with respect to (a) loading and (b) unloading [33]

(3) Surface hardness: An equipment surface suffers deformation (Figure 2.2) when the critical hardness ratio is reached (Figure 2.2). For particle sliding wear, the wear rate increases when hardness ratio range is $1.2 \leq H_p/H_e \leq 1.9$, and approximately maintains constant at $H_p/H_e > 1.9$ [37].

(4) Surface work-hardening: For metal surfaces that undergo ductile failures, their wear rates change when the material hardens [35].

(5) Surface thermal conductivity: The mechanical wear by dry bulk solids generates heat and causes temperature rise, which in turn affects wear rate [38].

2.1.3   Wear conditions

The wear conditions influence wear either directly or indirectly. Four characteristics of wear conditions are illustrated below.

(1) Handling operations: The conditions for handling operations involve transport speed, transport capacity and gas pressure in pneumatic conveying systems [27], which can significantly influence wear of equipment surfaces.

(2) Environmental factors: The environmental factors (e.g. temperature, humidity) can affect mechanical properties for both particulate solids and equipment surfaces and thus influence wear rates [38].

(3) Nonuniform properties: During the handling process, particles segregate as a result of the differences of sizes and densities [31, 39]. Besides, when particles suffer from uneven forces, the rotating motion is generated. In addition, the stick-slip motion can increases wear due to inconstant shear force [40].

(4) Particle self-wear: For certain conditions (e.g. using magnetic forces or modi-
fying surface topography [35]), particles are attached or bonded on equipment
surface, then the wear of equipment surface decreases as a result of the in-
creased chances of particle-particle interactions [38]. Besides, when particles
are highly concentrated at the pipe bends of pneumatic conveying systems,
wear rate decreases due to the enhanced shielding effect [27, 41].

2.2 Wear mechanisms

Based on the three wear aspects described in section 2.1, the main wear of bulk
solids handling equipment surfaces is categorized into two wear types, which
are abrasive wear and erosive wear. To enable the deviation of wear equations
to quantify the volume loss, the wear mechanisms for these two wear types are
discussed below.

2.2.1 Abrasive wear

Abrasive wear is caused by relative sliding and rolling of particles against equip-
ment surfaces [35, 42]. Abrasive wear occurs in the two forms of the two-body
abrasion and three-body abrasion [35, 42]. Two-body abrasion is also referred to as
sliding wear, which occurs simply by particle sliding. To trigger solely sliding of
particles, the contact pressure is thus high (Figure 2.5(a)). Three-body abrasion oc-
curs by both sliding and rolling, which has relatively low contact pressure to per-
mit rolling of particles (Figure 2.5(b)). Consequently, two-body abrasion causes
more volume loss than three-body abrasion. Depending on handling operations,
equipment surface can suffer from both two-body and three-body abrasion.
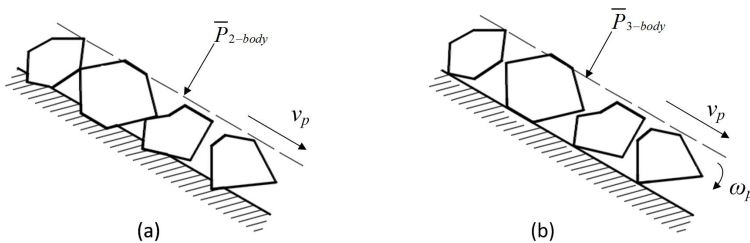
Figure 2.5: Schematic illustration of abrasive wear (a) two-body abrasion or slid-
ing wear (b) three-body abrasion

Figure 2.6 illustrates the four wear mechanisms for the material removal by abra-
sive wear, which are micro-ploughing micro-cutting, micro-fatigue and micro-
cracking [33]. According to section 2.1.2, the first three wear mechanisms can
occur on ductile surfaces as well as brittle surfaces. However, micro-cracking can
be triggered on a brittle material surface when the applied force exceeds a critical
level [34, 43]. The abrasive wear in bulk solids handling commonly occurs to bins,
silos and chutes [4, 21].
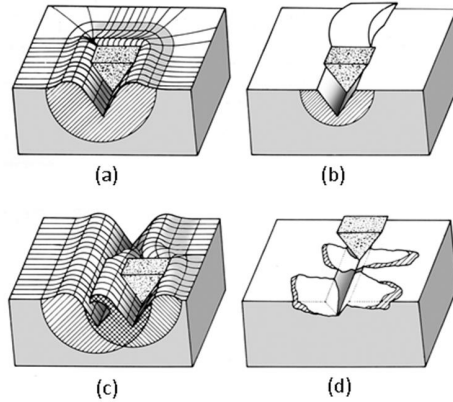
Figure 2.6: Abrasive wear mechanisms (a) micro-ploughing (b) micro-cutting (c) micro-fatigue (d) micro-cracking [33]

2.2.2   Erosive wear

Erosive wear is interpreted as a process of material removal from equipment surfaces or subsurfaces by succeeding particle impacts [42] (Figure 2.7). The impacting particles usually have a translational velocity and can also have a rotational motion. Two scenarios of erosive wear are identified subjected to different particle impact angles. One scenario is that a particle scratches the surface and leaves off at low impact angles. The other is that a particle remains at the surface after impact. Accordingly, erosive wear is categorized into two wear forms: namely, low angle impact and high angle impact (Figure 2.8 (a-b)).
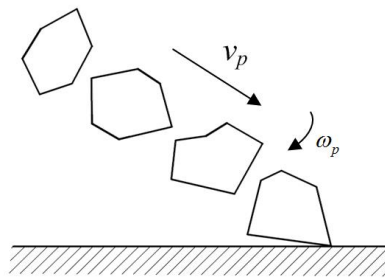
Figure 2.7: Schematic illustration of erosive wear in bulk solids handling

The erosive wear causes material removals from two wear mechanisms: cutting wear and deformation wear [32]. Cutting wear is dominant at low impact angles (Figure 2.8 (a)) whilst deformation wear becomes the principal component at high impact angles (Figure 2.8 (b)) [32]. Similar to that of sliding wear, the cutting and deformation wear can cause ductile failures for both ductile and brittle surfaces when particle impact stress is low. Otherwise, erosive wear triggers fracture on

brittle surface (Figure 2.8(c)). Erosive wear commonly occurs to curved plates at discharge points, and pipe bends in pneumatic conveying systems [27, 35, 42].
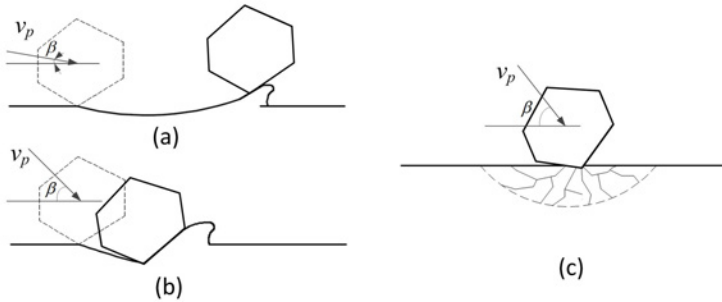
Figure 2.8: Schematic illustration of erosive wear (a) low angle impact (b) high angle impact (c) brittle fracture caused by particle impact [33]

2.3 Wear equations

Based on the wear mechanisms as discussed in section 2.2, the analytical wear models in bulk solids handling can be developed, on which basis the equations to quantify wear can be derived. Many existing equations can be used for quantifying abrasive wear and erosive wear [44]. However, in this research, the most relevant equations to quantify wear under bulk solids handling conditions are illustrated.

2.3.1 Abrasive wear

As was illustrated in section 2.2.1, abrasive wear involves the two wear models of the two-body abrasion (sliding wear) and three-body abrasion. Each model has distinctive equations for quantifying wear volumes. With respect to ductile and brittle surfaces, the equations for quantifying wear loss by single particle are firstly illustrated, then wear equations by bulk solids are presented. Finally, combined equations for estimating abrasive wear volumes are provided.

Ductile surface

For the abrasive wear on a ductile surface, the following notations are used to represent wear volumes W_V.

$W_{V,d,p,s,t}$: Wear Volume of Ductile failure by Particle Sliding at Transient state

$W_{V,d,p,s,s}$: Wear Volume of Ductile failure by Particle Sliding at Steady state

$W_{V,d,b,s,s}$: Wear Volume of Ductile failure by Bulk solids Sliding at Steady state

$W_{V,d,p,r}$: Wear Volume of Ductile failure by Particle Rolling

$W_{V,d,b,r}$: Wear Volume of Ductile failure by Bulk solids Rolling

$W_{V,d,b,a,s}$: Wear Volume of Ductile failure by Bulk solids Abrasive wear at Steady state

The sliding wear on a ductile surface undergoes the two important wear phases: namely, transient and steady-state, which are shown in Figure 2.9 [45]. For the transient-state, the wear volume can be evaluated by Equation 2.1 [45],
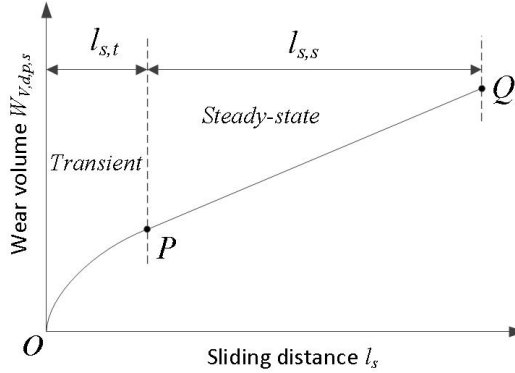
Figure 2.9: Two wear phases of sliding wear [45]

$$W_{V,d,p,s,t} = A_0[1 - e^{-B_0 l_{s,t}}] \tag{2.1}$$

in which A_0 and B_0 are constants; $l_{s,t}$ is the sliding distance for transient state.

For the sliding wear at steady-state, a generalized equation to quantify volume loss is given by Equation 2.2 [35, 42, 46].

$$W_{V,d,p,s,s} = \kappa_1 \frac{F_n}{H_e} l_{s,s} \tag{2.2}$$

in which κ_1 is a dimensionless coefficient; F_n is the normal force applied to an equipment surface and $l_{s,s}$ is the sliding distance for the steady state. By introducing $\alpha_s = \frac{\kappa_1}{H_e}$, Equation 2.2 is simplified as,

$$W_{V,d,p,s,s} = \alpha_s F_n l_{s,s} \tag{2.3}$$

in which α_s is defined as the coefficient of sliding wear.

Equation 2.2 was originally derived by Archard [46] by assuming that wear loss is the accumulative detachment of materials from hemispherical particle asperities after three wear stages. Figure 2.10(a-c) illustrates the three wear stages that two hemispherical particle asperities slide against each other. Archard's derivation provides $\kappa_1 = \frac{\phi_1}{3}$ [46].

Later, Equation 2.2 was also derived based on the assumption that a conical particle tip slides against a flat surface [35, 42]. Figure 2.11 illustrates the sliding wear

model, in which a normal force F_n applies on a conical tip and results in the indention depth z_1 and the circle projection with the radius a_1. This deviation gives $\kappa_1 = \frac{2\phi_2}{\pi \tan \theta_1}$ [35, 42].
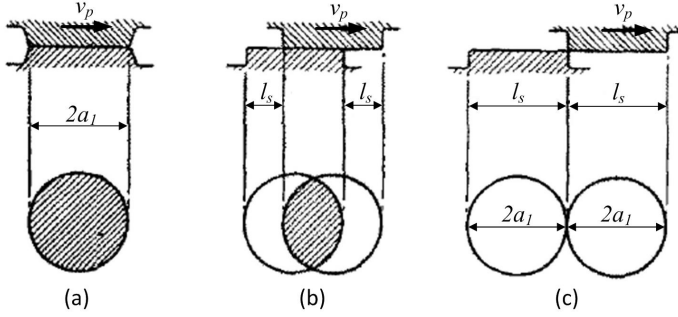
Figure 2.10: Idealized conception of single contact for two sliding particle tips with an equal size (a) two particle tips are fully contacted (b) a relatively sliding distance (c) two particle tips apart [5, 46]
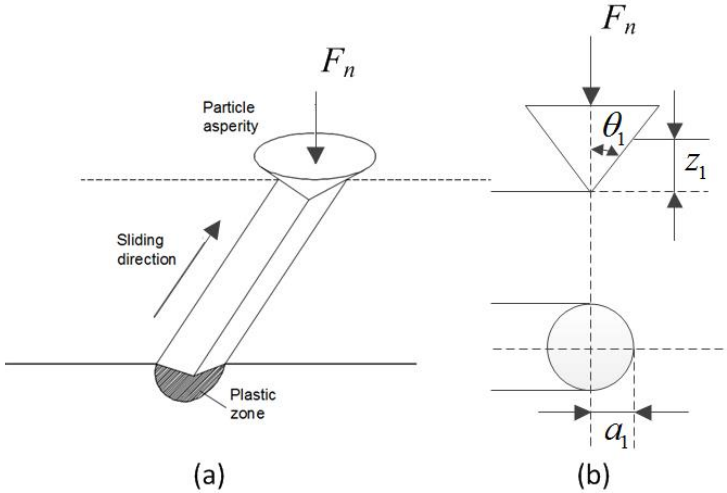
Figure 2.11: Schematic illustration of sliding wear model (a) a sliding particle tip on a flat surface (b) two-dimensional illustration [35, 42]

To estimate the wear volume subjected to bulk solids, N_p is used to represent the number of particles that are in contact with equipment surface. By assuming that the contact area A_b is formed by a square packing distribution of uniform particle diameter d_p, then N_p is expressed by,

$$N_p = \frac{A_b}{d_p^2} \tag{2.4}$$

By postulating that equal pressure $\bar{P}$ applies on each particle that is in contact with equipment surface. Using Equation 2.4, the normal force is expressed by,

$$F_n = \frac{F_N}{N_p} = \bar{P}d_p^2 \tag{2.5}$$

Using Equation 2.5, Equation 2.2 is converted to Equation 2.6 to estimate wear volume by bulk solids at the steady-state,

$$W_{V,d,b,s,s} = \kappa_1 \frac{F_n N_p}{H_e} l_s = \kappa_1 \frac{\bar{P} A_b}{H_e} l_{s,s} \tag{2.6}$$

Thus far, the equations for estimating sliding wear (two-body abrasion) with respect to a ductile surface are illustrated. For three-body abrasion, the rolling wear must be accounted for. Figure 2.12 illustrates the rolling wear model that an irregular particle rotates against a flat surface. The wear volume by particle rolling can be estimated by Equation 2.7 [47].
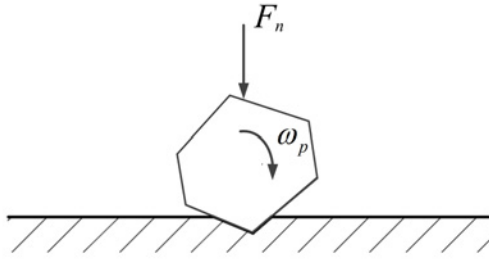
Figure 2.12: Rolling wear model

$$W_{V,d,p,r} = \frac{\phi_3 F_n z_1 N_i l_r}{3\pi H_e N_c d_p} \tag{2.7}$$

in which ϕ_3 is a fraction of the volume of indentation after N_c indentations; N_i is the number of indentations per particle rotation. N_c is expressed by a modified Coffin-Manson equation [48]:

$$N_c = \left(\frac{\epsilon_C}{\epsilon_P}\right)^\upsilon \tag{2.8}$$

where ϵ_C is critical failure strain, ϵ_P is mean plastic strain per particle indentation. υ is applied by 1 for accumulated plastic strain, and by 2 corresponding to fatigue failure, and by a value between 1 and 2 for a mixed failure model.

Using Equation 2.5 and introducing the coefficient of κ_2, which is,

$$\kappa_2 = \frac{\phi_3 z_1 N_i}{3\pi N_c d_p} \tag{2.9}$$

Equation 2.7 is modified to Equation 2.10 to estimate wear volume by bulk solids rolling,

$$W_{V,d,b,r} = \kappa_2 \frac{\bar{P}A_b}{H_e} l_r \tag{2.10}$$

In bulk solids handling, the wear rate for transient state is slightly higher than the steady-state [35, 42], which is also implied by Figure 2.9. Thus Equation 2.6 is also applied for approximating wear of transient-state. In combination with the rolling wear Equation, 2.10 for sliding and rolling wear by bulk solids, Equation 2.11 was derived to quantify abrasive wear volume for bulk solids handling equipment surface,

$$W_{V,d,b,a} = \kappa_1 \frac{\bar{P}A_b}{H_e} l_s + \kappa_2 \frac{\bar{P}A_b}{H_e} l_r \tag{2.11}$$

Equation 2.11 is used to estimate the absolute wear volumes. However, for simply evaluating wear rates under different bulk solids handling conditions, Roberts [4, 21] proposed abrasive wear factors (parameters) (Equations 2.12 and 2.13) to estimate wear loss of several bulk solids handling equipment.

To represent the relative abrasive wear, the following two notations are used.

$f_{a,s}$: Factor for evaluating Abrasive wear rate on Straight surface

$f_{a,c}$: Factor for evaluating Abrasive wear rate on Chute surfaces for any chute profile

Equation 2.12 shows a factor to evaluate the abrasive wear rates on the surfaces of bins, silos and straight chutes [21].

$$f_{a,s} = \frac{\sigma_e v_s \tan\theta_w}{\sigma_l} \tag{2.12}$$

where σ_e is the normal pressure at equipment surface; v_s is the relative sliding velocity of particulate solids in contact with equipment surfaces; θ_w is the wall friction angle between bulk solids and equipment surface; σ_l is the linear wear factor. σ_l depends on the interactive properties of the equipment surface and the bulk solid and is experimentally determined by conducting wear test of the lining material [21].

Equation 2.13 shows another factor to evaluate abrasive wear rates on the surfaces of curved and straight chutes [4],

$$f_{a,c} = \frac{q_b v_a \tan\theta_w}{v_s B_c} J_n \tag{2.13}$$

in which q_b is the flow rate by mass, v_a is the average stream velocity at section considered; B_c is chute width; J_n is the normal acceleration of bulk material to contact of the transfer chute surface. For a curved chute J_n is,

$$J_n = \frac{v_a^2}{R_1} + g \sin \theta_L \tag{2.14}$$

where R_1 is the radius of transfer chute and θ_L is the angle between tangential velocity of bulk solid and gravity g. For inclined straight chute, J_n is,

$$J_n = g \sin \theta_L \tag{2.15}$$

Brittle surface

As was discussed in Section 2.2.1, a brittle surface suffers from ductile failure when the loading fore is low. For this condition, Equation 2.6 is applied to estimate wear volume. However, on the condition that the loading force F_n reaches a critical value $F_{n,C}$ [34, 43], the abrasive wear on a brittle material causes brittle failure. Figure 2.13 illustrates the brittle failure caused by sliding wear corresponding to Model I (Figure 2.4). It indicates that along the wear path, the surface and subsurface fracture through median (M) and lateral (L) cracks. z_2 and c_l are respectively the height and the length by lateral crack.
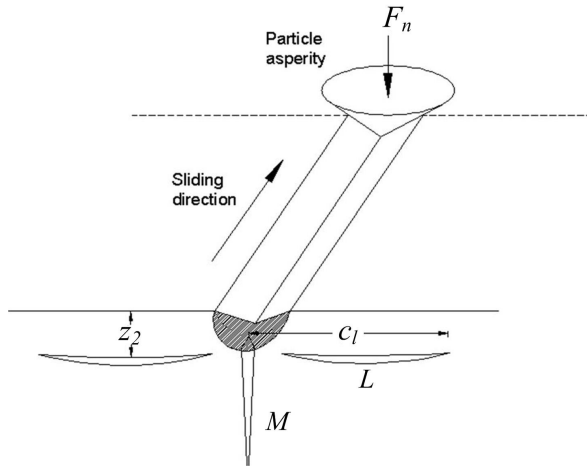
Figure 2.13: Wear of brittle failure by single particle

For abrasive wear on a brittle surface material, the following notations are used to represent different wear volumes.

$W_{V,b,p,s}$: Wear Volume of Brittle Failure by Particle Sliding

$W_{V,b,b,s}$: Wear Volume of Brittle Failure by Bulk solids Sliding

Available equations to estimate brittle wear volumes are mainly studied by Evans et al. [49–51]. A generalized equation to estimate the wear volume of brittle failure is expressed by Equation 2.16,

$$W_{V,b,p,s} = \lambda_i \frac{F_n^{u_i}}{K_{I,C}^{v_i} H_e^{w_i}} \left(\frac{E_e}{H_e}\right)^{x_i} l_s \tag{2.16}$$

where $K_{I,C}$ is fracture toughness for a brittle failure. The values of $K_{I,C}$ for a range of brittle materials are given in [35, 52]. u, v, w and x are the power exponents. Three groups of values for the power exponents were derived, which are presented in Table 2.1 [49–51].

Table 2.1: Power exponents of wear equations for brittle failure [49–51]

Literature sources	u_i	v_i	w_i	x_i
Evans and Wilshaw [49]	5/4	3/4	1/2	0
Evans [50]	7/6	2/3	1/2	0
Marshall, Lawn and Evans [51]	9/8	1/2	5/8	3/4

The power exponents in the first row of Table 2.1 were derived using laboratory tests for sapphire, spinel, silicon nitride and zinc selenite [49]. Thus these power exponents are applicable to those materials. The derivation of the power exponents in the second row utilizes Vicker's indentation tests [50]. For the third row, the ratio Young's modulus to hardness (E_e/H_e) was used by accounting for elastic/plastic boundary [51]. Both the second and third rows are applicable for ceramic materials.

By summing over all particles that are in contact with equipment surface and using Equations 2.4 and 2.5, the wear loss on a brittle material surface triggered by bulk solids is expressed by Equation 2.17,

$$W_{V,b,p,s} = \frac{\lambda_i F_n^{u_i} N_p}{K_{I,C}^{v_i} H_e^{w_i}} \left(\frac{E_e}{H_e}\right)^{x_i} l_s \tag{2.17}$$

Using Equation 2.5, Equation 2.17 is converted to Equation 2.18,

$$W_{V,b,p,s} = \frac{\lambda_i (\bar{P} d_p^2)^{u_i} A_b}{K_{I,C}^{v_i} H_e^{w_i} d_p^2} \left(\frac{E_e}{H_e}\right)^{x_i} l_s = \frac{\lambda_i \bar{P}^{u_i} A_b d_p^{2(u_i-1)}}{K_{I,C}^{v_i} H_e^{w_i}} \left(\frac{E_e}{H_e}\right)^{x_i} l_s \tag{2.18}$$

Table 2.1 demonstrates that $2(u_i - 1) > 0$ and referring to Equation 2.18, it means that for brittle materials the sliding wear volume increases with increasing particle diameter d_p [35].

To this end, the analytical wear models for abrasive wear on ductile and brittle surfaces are elaborated. A generalized graph to illustrate abrasive wear consequences of ductile and brittle surfaces with respect to applied normal force is shown in Figure 2.14. In bulk solids handling, abrasive wear commonly causes ductile failure for the ductile and also for brittle surfaces. Table 2.2 summaries the wear equations for calculating abrasive wear of bulk solids handling equipment surfaces.
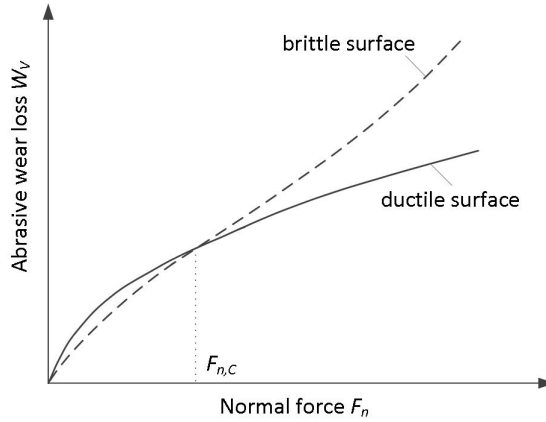
Figure 2.14: Generalized graph to illustrate abrasive wear for ductile and brittle surfaces subjected to different applied forces

Table 2.2: Equations for calculating abrasive wear loss caused by bulk solids

Wear loss	Wear equations	Applications
Absolute	$\kappa_1 \frac{\bar{P}_e A_b}{H_e} l_s$	sliding of bulk solids [35]
	$\kappa_1 \frac{\bar{P}_e A_b}{H_e} l_s + \kappa_2 \frac{\bar{P}_e A_b}{H_e} l_r$	sliding and rolling of bulk solids [35, 47]
Relative	$\frac{\sigma_e v_s \tan \theta_e}{\sigma_l}$	sliding of bulk solids against straight surface [21]
	$\frac{q_b v_b \tan \theta_e}{v_s B_c} J_n$	sliding against straight and curved surfaces [4]

2.3.2   Erosive wear

As was elaborated in section 2.2.2, erosive wear consists of a cutting mechanism and a deformation mechanism. Accordingly, the erosive wear equations are illustrated from a cutting model and a deformation model. Then the equations to quantify both cutting wear and deformation wear are presented. Similar to abrasive wear, the erosive wear equations are illustrated for ductile and brittle surfaces, ranging from single particle to bulk solids.

Ductile surface

Figure 2.15 shows a cutting wear model with respect to a ductile surface. As was discussed in section 2.2, two scenarios are distinguished, subjected to particle impact angles. To quantify the wear loss of these two scenarios, the commonly used wear equations derived by Finnie [53–55], Bitter [56, 57], Neilson and Gilchrist [58] are illustrated as below.

To represent the volumes W_V by erosive wear on ductile surfaces, the following notations are used.

$W_{V,d,p,c}$: Wear Volume of Ductile failure by Particle Cutting

$W_{V,d,b,c}$: Wear Volume of Ductile failure by Bulk solids Cutting

$W_{V,d,p,d}$: Wear Volume of Ductile failure by Particle deformation

$W_{V,d,b,d}$: Wear Volume of Ductile failure by Bulk solids Deformation

$W_{V,d,p,e}$: Wear Volume of Ductile failure by Particle Erosive wear

$W_{V,d,b,e}$: Wear Volume of Ductile failure by Bulk solids Erosive wear

$W_{V,d,p,e,90}$: Wear Volume of Ductile failure by Particle Erosive wear at 90° impact angle

$W_{V,d,b,e,90}$: Wear Volume of Ductile failure by Bulk solids Erosive wear at 90° impact angle
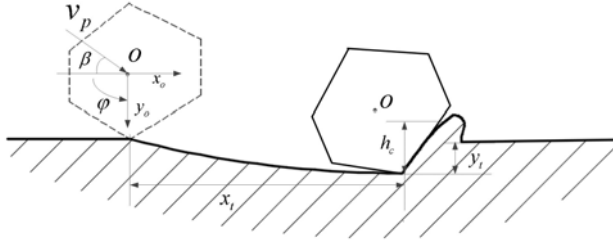
Figure 2.15: Cutting wear model of single particle impact based on [53]

The earliest equations to quantify the cutting wear were derived by Finnie [53–55], which are summarized as Equation 2.19.

$$W_{V,d,p,c} = K_e \cdot \zeta(\beta) = \frac{m_p v_p^2}{2} \cdot \zeta(\beta) \tag{2.19}$$

One group for $\zeta(\beta)$ is shown by Equations 2.20a and 2.20b [53],

$\beta \leq \beta_0 = \tan^{-1}(C_0/6)$,

$$\zeta(\beta) = \frac{2}{P_h \psi C_0}[\sin(2\beta) - \frac{6}{C_0}\sin^2\beta] \tag{2.20a}$$

$\beta \geq \beta_0 = \tan^{-1}(C_0/6)$,

$$\zeta(\beta) = \frac{\cos^2\beta}{3P_h\psi} \tag{2.20b}$$

where C_0 is the ratio of the vertical component to the horizontal component of impact force. C_0 is considered as constant which is close to 2 for any impact angles [53]. P_h is the horizontal component of the contact pressure between the particle and the worn surface. P_h is given by a Hertzian treatment of purely elastic collisions (Equation 2.21) [26, 59]. ψ is the ratio of the contact height h_c between the particle and the target surface to the indentation depth y_t (Figure 2.15).

$$P_h = \frac{2}{3}\left(\frac{40}{\pi^4}\rho_p\right)^{1/5}\left(\frac{1-q_p^2}{E_p} + \frac{1-q_e^2}{E_e}\right)^{(-4/5)}(v_p\cos\beta)^{2/5} \tag{2.21}$$

Later, Finnie et al. [54, 55] accounted for the moment of particle inertia and derived another group of $\zeta(\beta)$, which is given by Equations 2.22(a-b) subjected to low and high impact angles,

$$\beta \leq \beta_0 = \tan\left\{\frac{C_0}{2[1+(m_pd_p^2/4I_p)]}\right\}^{-1},$$

$$\zeta(\beta) = \frac{C_1}{P_hC_0}\left[\sin(2\beta) - \frac{2(1+m_pd_p^2/4I_p)\sin^2\beta}{C_0}\right] \tag{2.22a}$$

$$\beta \geq \beta_0 = \tan\left\{\frac{C_0}{2[1+(m_pd_p^2/4I_p)]}\right\}^{-1},$$

$$\zeta(\beta) = \frac{C_1\cos^2\beta}{2P_h(1+(m_pd_p^2/4I_p)} \tag{2.22b}$$

in which C_1 is an empirical constant which is defined as the fraction of particles cutting in an idealized manner, C_1 can be expressed by [32],

$$C_1 = \frac{P_h\psi i_c C_0}{m_p} \tag{2.23}$$

where i_c is the average cutting width by the asperity of an impact particle.

Besides Finnie's cutting wear Equations 2.19 and 2.22, Bitter [56, 57] also derived cutting wear equations subjected to low and high impact angles, which are expressed by Equations 2.24(a-b):

$\beta \leq \beta_0$,

$$W_{V,d,p,c} = \frac{2m_pC_2(v_p\sin\beta - v_e)^2}{\sqrt{v_p\sin\beta}}\left[v_p\cos\beta - \frac{C_2(v_p\sin\beta - v_e)^2}{\sqrt{v_p\sin\beta}}\varepsilon_c\right] \tag{2.24a}$$

$\beta \geq \beta_0$,

$$W_{V,d,p,c} = \frac{m_p[v_p^2\cos^2\beta - C_3(v_p\sin\beta - v_e)^{3/2}]}{2\varepsilon_c} \tag{2.24b}$$

where ε_c is the cutting factor which is defined as the required energy that triggers unit volume failure from eroded surface; v_e is the maximum particle velocity at which the collision still is purely elastic; C_2 and C_3 are constants. C_2 and C_3 are given by Equations 2.25 and 2.26, respectively,

$$C_2 = \frac{0.288}{gY_e}\left(\frac{\rho_p}{Y_e}\right)^{1/4} \tag{2.25}$$

$$C_3 = 0.82gY_e^2 \left(\frac{Y_e}{\rho_p}\right)^{1/4} \left(\frac{1-q_p^2}{E_p} + \frac{1-q_e^2}{E_e}\right) \tag{2.26}$$

in which Y_e is the elastic load limit.

In the Equations 2.24a and 2.24b, v_e is expressed by Equation 2.27 [57]. Noted that v_e is independent of particle shapes.

$$v_e = \frac{\pi^2}{200\sqrt{10}}(1.59Y_e)^{5/2}\left(\frac{1}{\rho_p}\right)^{1/2}\left(\frac{1-q_p^2}{E_p} + \frac{1-q_e^2}{E_e}\right)^2 \tag{2.27}$$

By comparing Bitter's Equations 2.24 and 2.22 with Finnie's Equation 2.20, it implies that Finnie neglected the elastic deformation during particle impact [56, 57].

Neilson and Gilchrist [58] simplified Bitter's cutting wear Equation 2.24 into 2.28, $\beta \leq \beta_0$,

$$W_{V,d,p,c} = \frac{m_p v_p^2 \cos^2\beta \sin(k_0\beta)}{2\varepsilon_c} \tag{2.28a}$$

$\beta \geq \beta_0$,

$$W_{V,d,p,c} = \frac{m_p v_p^2 \cos^2\beta}{2\varepsilon_c} \tag{2.28b}$$

where k_0 is a constant. When $\beta = \beta_0$, $\sin(k_0\beta_0) = 1$, i.e., $\beta_0 = 90^o/k_0$.

Up to now, the commonly used equations for quantifying cutting wear are presented. To calculate deformation wear loss, Bitter developed Equation 2.29 [56],

$$W_{V,d,p,d} = \frac{m_p(v_p \sin\beta - v_e)^2}{2\varepsilon_d} \tag{2.29}$$

in which ε_d is the deformation wear factor, which means the energy required to remove a unit volume of material from the target surface.

Using the above equations to quantify cutting and deformation wear, the erosive wear loss can be quantified by,

$$W_{V,d,p,e} = W_{V,d,p,c} + W_{V,d,p,d} \tag{2.30}$$

Besides Equation 2.30, O'Flynn et al. [60] and Mbabazi et al. [61] respectively developed the combined erosive equations that account for both cutting and deformation wear.

Equation 2.31 presents the combined equation developed by O´Flynn et al. [60]. This equation was validated by using fine olivine sand to impact heat-treated steels. However, the authors [60] concluded that this model must be improved to predict accurate results.

$$W_{V,d,p,e} = \frac{m_p v_p{}^2}{\eta_1 \varepsilon_d}(\kappa_c \cos^4 \beta + \kappa_d \sin^2 \beta) \tag{2.31}$$

where η_1 is the material dependency of the efficiency of material removal, κ_c and κ_d are constants respectively for cutting and deformation wear models.

The erosive wear equation derived by Mbabazi et al. [61] is shown by Equation 2.32, which was validated by the impact of steel surfaces subjected to boiler fly ash particles.

$$W_{V,d,p,e} = \frac{\eta_2 m_p \rho_p{}^{1/2} v_p{}^3 \sin^3 \beta}{H_e^{3/2}} \tag{2.32}$$

in which η_2 is the overall coefficient in this erosive wear model.

For the erosive wear at 90° impact angle, the wear loss is contributed completely by particle deformation mechanism. It is postulated that the surface material becomes fatigued by cyclic plastic deformation [48, 62] or detached when the accumulated plastic strain reaches a critical value [63]. Without taking into account the thermo-physical properties of the target material, for both cases the impact of spherical particles on the wear loss can be estimated by Equation 2.33 [42, 62, 63].

$$W_{V,d,p,e,90^o} = \eta_3 \frac{m_p \rho_p{}^{1/2} v_p{}^3}{\epsilon_C^2 H_e^{3/2}} \tag{2.33}$$

where η_3 is the ratio of the volume of material which is plastically strained by each particle impact to the total energy dissipated to the equipment surface.

By assuming that all impact particles make contact with equipment surface, then the erosive wear loss is taken as m_b/m_p times to that by a single particle [53]. That is, the equations to estimate erosive wear loss by bulk solids are obtained by using m_b to replace m_p in the erosive wear equations for single particle. In bulk solids handling, Finnie's cutting wear Equation 2.22, Neilson and Gilchrist's Equation 2.28, and Bitter's deformation wear Equation 2.27 were applied (e.g. [26, 59, 64]).

In addition to the equations for calculating absolute volume, a factor is used to estimate erosive wear at the loading point of a conveyor belt [4], which is given by Equation 2.34. Note:

$f_{e,l}$: Factor for evaluating Erosive wear rate on a Loading conveyor belt surface

$$f_{e,b} = \mu_b v_x \rho_b v_y^2 = \rho_b v_p^3 \mu_b \sin \beta \cos^2 \beta \tag{2.34}$$

where μ_b is the coefficient of friction between bulk solid and conveyor belt surface; v_x is the relative horizontal velocity of bulk solid with respect to the movement of conveyor belt, and v_y is the vertical velocity of bulk solid at the loading point of belt surface.

Brittle surface

Similar to abrasive wear for brittle surfaces, the equations for estimating erosive wear of ductile surfaces are also applicable when simply suffering from ductile failure. However, for brittle failure caused by erosive wear, the equations below can be applied, which are based on quasi-static models [30, 35].

For brittle failure by erosive wear on brittle surfaces, the following notation is used to represent wear volume.

$W_{V,b,p,e,90}$: Wear Volume of Brittle failure by Particle Erosive wear at 90° impact angle

$W_{V,b,p,e,90}$: Wear Volume of Brittle failure by Bulk solids Erosive wear at 90° impact angle

A generalized form for calculating brittle fracture by single particle at 90° impact angle is given by Equation 2.35 [35, 49, 51]. The values for the power exponents are listed in Table 2.3.

$$W_{V,b,p,e,90} = \chi_j G_e^{k_j} m_p^{l_j} v_p^{n_j} \frac{H_e^{p_j}}{K_{I,C}^{q_j} d_p^{r_j}} \left(\frac{E_e}{H_e}\right)^{s_j} \tag{2.35}$$

Table 2.3: Exponents in Equation 2.35 for calculating fracture by particle impact

Literature sources	k_j	l_j	n_j	p_j	q_j	r_j	s_j
Evans and Wilshaw [49]	4/5	6/5	12/5	1/2	3/2	2/5	0
Marshal, Lawn and Evans [51]	0	7/6	7/3	1/6	1	0	5/4
Hilgraf [35]	0	11/9	22/9	1/9	4/3	0	0

In the Table 2.3, the values in the first row apply to a conservative calculation of erosive wear volume with respect to severe impact conditions (e.g. $F_n > 10F_{I,C}$ [49]). The second row is for low particle velocities and low impact forces (e.g. $F_n \leq 10F_{I,C}$ [51]). The third row is an approximate wear evaluation using impulse-momentum theory and the fracture model subjected to Vicker's indentation [35, 50].

Similar to quantifying erosive wear for ductile failure by bulk solids, the erosive wear for brittle failure is derived by substituting m_p in Equation 2.35 with m_b, and v_p with v_b. Noticed that the exponent r_j for particle diameter in the first row is positive, which indicates that for equal amount of bulk solids, the wear loss decreases with increasing particle radius.

Thus far, the erosive wear equations for both ductile and brittle surfaces are illustrated with respect to non-rotating particles. For particles that have rotational motion, the impact angle and velocity must be correspondingly modified using equations in [26, 65].

To this end, a generalized graph to illustrate erosive wear consequences of ductile and brittle failures is given in Figure 2.16. It shows that for ductile surface the highest wear rate occurs at a low impact angle, whereas for brittle surface at

normal incidence. In bulk solids handling, erosive wear commonly causes ductile failure for both ductile and brittle equipment surfaces. Therefore, the erosive wear equations and applications in bulk solids handling are summarized in Table 2.6.
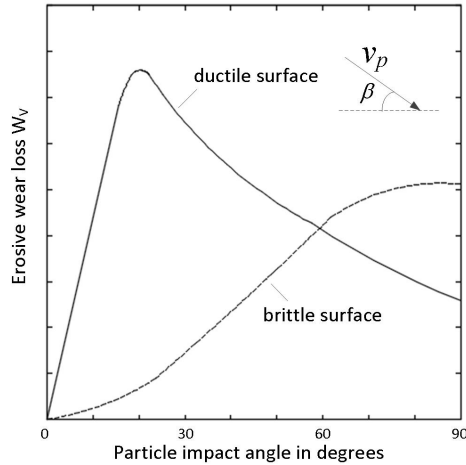
Figure 2.16: Generalized graph to illustrate erosive wear for ductile and brittle surfaces subjected to different impact angles

2.4 Application examples

The previous section illustrated the wear equations for both ductile and brittle surfaces. It also summarized the applications of wear equations in bulk solids handling. In this section, two wear scenarios in bulk solids handling are presented. Additionally, the wear loss for these two scenarios are theoretically predicted.

2.4.1 Abrasive wear

At a bulk terminal, a transfer chute is an important bulk solids handling equipment that can be used to accelerate placement of bulk solids onto a conveyor belt. Figure 2.17 (a) shows a transfer process in a belt conveying system with a flow rate of q_b for handling iron ore [4]. This transfer process involves four necessary equipment items: the feeder, acceleration belt, chute and conveyor. The speed of the accelerating belt is limited to 0.3 m/s [4]. This chute has a constant cross-section. The dimensions and positions of these four equipment are indicated in Figures 2.17(b).

To estimate the sliding wear on the surface on chute bottom surface, the bulk flow model is presented in Figure 2.18 [4]. According to the sliding wear Equation 2.2, the wear volume by the element mass Δm_b for the distance dl_s is calculated by Equation 2.36,

Table 2.6: Equations for calculating wear loss of erosive wear by bulk solids

Wear loss	Impact angle	Wear equations	Application conditions
	$0 < \beta \le \beta_0$	$\frac{m_b v_p^2}{P_h \psi C_0}\left[\sin(2\beta) - \frac{6}{C_0}\sin^2\beta\right] + \frac{m_b(v_p\sin\beta - v_e)^2}{2\varepsilon_d}$	metals, no account of particle inertia [53]
		$\frac{C_1 m_b v_p^2}{2P_h C_0}\left[\sin(2\beta) - \frac{2(1+m_b d_p^2/4I_p)\sin^2\beta}{C_0}\right] + \frac{m_b(v_p\sin\beta - v_e)^2}{2\varepsilon_d}$	metals, accounting particle inertia [54, 55]
		$\frac{2m_b C_2(v_p\sin\beta - v_e)^2}{\sqrt{v_p\sin\beta}}\left[v_p\cos\beta - \frac{C_2(v_b\sin\beta - v_e)^2\varepsilon_c}{\sqrt{v_p\sin\beta}}\right] + \frac{m_b(v_p\sin\beta - v_e)^2}{2\varepsilon_d}$	ductile and brittle materials [57]
Absolute		$\frac{m_b v_p^2\cos^2\beta\sin(k_0\beta)}{2\varepsilon_c} + \frac{m_b(v_p\sin\beta - v_e)^2}{2\varepsilon_d}$	ductile materials [58, 66]
	$\beta_0 \le \beta \le 90^o$	$\frac{m_b v_p^2\cos^2\beta}{6P_h\psi C_0} + \frac{m_b(v_p\sin\beta - v_e)^2}{2\varepsilon_d}$	metals, no account of particle inertia [53]
		$\frac{C_1 m_b v_p^2\cos^2\beta}{4P_h(1+(m_b d_p^2/4I_p))} + \frac{m_b(v_p\sin\beta - v_e)^2}{2\varepsilon_d}$	metals, accounting particle inertia [54, 55]
		$\frac{m_b[v_p^2\cos^2\beta - K_2(v_p\sin\beta - v_e)^{3/2}]}{2\varepsilon_c} + \frac{m_b(v_p\sin\beta - v_e)^2}{2\varepsilon_d}$	ductile and brittle materials [57]
		$\frac{m_b v_p^2\cos^2\beta}{2\varepsilon_c} + \frac{m_b(v_p\sin\beta - v_e)^2}{2\varepsilon_d}$	ductile materials [58, 66]
	$0 < \beta \le \beta_0$	$\frac{m_b v_p^2}{\eta_0\varepsilon_d}\left(\kappa_c\cos^4\beta + \kappa_d\sin^2\beta\right)$	metals, however high deviations exist [60]
		$\frac{\eta_2 m_b\rho_p^{1/2} v_p^3\sin^3\beta}{H_e^{3/2}}$	mild steel impacted by boiler fly ash [61]
	$\beta = 90^o$	$\frac{\eta_3 m_b\rho_p^{1/2} v_p^3}{\epsilon_C^2 H_e^{3/2}}$	metals impacted by spherical particles [42]
Relative	$0 < \beta \le 90^o$	$\rho_b v_p^3\mu_b\sin\beta\cos^2\beta$	impact by bulk solids, e.g. conveyor belt [4]
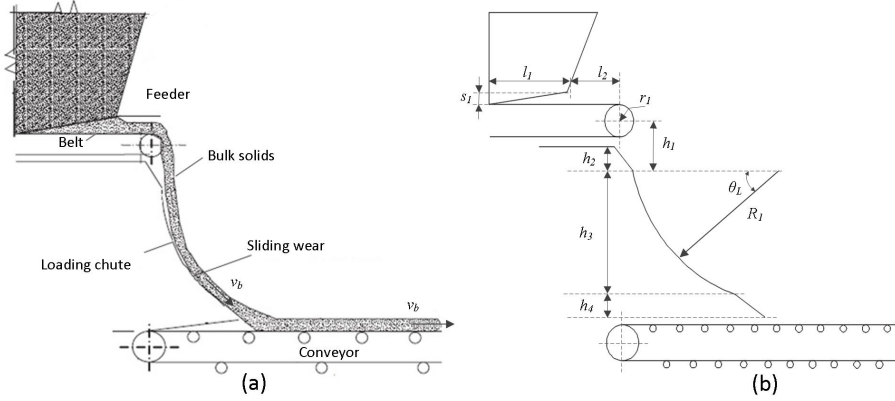
Figure 2.17: A transfer process in a belt conveying system (a) Feeding and transfer to a conveyor belt (b) Positions and dimensions
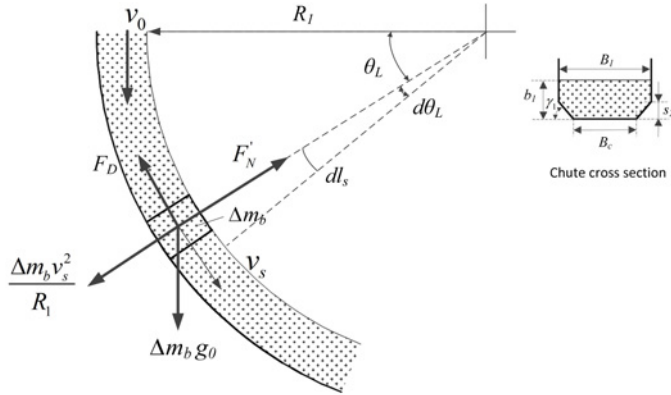
Figure 2.18: Bulk flow model on a loading chute [4]

$$\Delta W_{\Delta m_b, s} = \kappa_1 \frac{\bar{P}_e \Delta A_b}{H_e} dl_s = \kappa_1 \frac{\Delta F_b}{H_e} dl_s \tag{2.36}$$

in which ΔF_b is the applied normal on the elemental mass Δm_b. Using Equation 2.14, ΔF_b becomes,

$$\Delta F_b = \Delta m_b J_n = \Delta m_b \cdot \left[\frac{v_s(\theta_L)^2}{R_1} + g \sin \theta_L \right] \tag{2.37}$$

dl_s is given by,

$$dl_s = R_1 d\theta_L \tag{2.38}$$

Using Equations 2.37 and 2.38, Equation 2.36 becomes,

$$\Delta W_{\Delta m_b,s} = \frac{\kappa_1 \Delta m_b}{H_e}[v_s(\theta_L)^2 + R_1 g \sin\theta_L]d\theta_L \tag{2.39}$$

The wear for the element mass Δm_b moving through the curved chute is expressed by the integral from $\theta_L = 0$ to $\theta_L = \theta_{L,m}$,

$$W_{\Delta m_b,s} = \frac{\kappa_1 \Delta m_b}{H_e} \int_0^{\theta_{L,m}} [v_s(\theta_L)^2 + R_1 g \sin\theta_L]d\theta_L \tag{2.40}$$

Substitute Δm_b with q_b in Equation 2.40, the wear rate (which is wear volume per second) is obtained,

$$Q_{q_b,s} = \frac{\kappa_1 q_b}{H_e} \int_0^{\theta_{L,m}} [v_s(\theta_L)^2 + R_1 g \sin\theta_L]d\theta_L \tag{2.41}$$

Assuming $v_s = v_0$ at $\theta_L = 0$, then $v_s(\theta_L)^2$ is given by [4].

$$v_s(\theta_L)^2 = \frac{2gR_1}{4\mu_e^2 + 1}[(1 - 2\mu_e^2)\sin\theta_L + 3\mu_e \cos\theta_L] + (v_0{}^2 - \frac{6\mu_e gR_1}{4\mu_e^2 + 1})e^{-\mu_e\theta_L} \tag{2.42}$$

where μ_e is equivalent friction factor which combines the coefficient of friction between the bulks solids and the chute surface; μ_e is expressed by [4],

$$\mu_e = \mu_s(1 + \varpi \frac{b_1}{B_1}) \tag{2.43}$$

in which ϖ is pressure ratio, which lies in 0.4-0.6 [4].

v_0 is calculated by,

$$v_0 = \sqrt{v_{x,0}^2 + v_{y,0}^2} \tag{2.44}$$

in which $v_{y,0}$ is given as,

$$v_{y,0} = \sqrt{v_{x,0}^2 + \frac{g^2(h_1 + r_1)^2}{v_{x,0}^2}} \tag{2.45}$$

Using Equation 2.42, the integral of Equation 2.41 leads to the sliding wear rate (wear volume per second), as expressed by Equation 2.46,

$$Q_{q_b,s} = \frac{\kappa_1 q_b}{H_e} \left[\frac{6 R_L g \mu_e \sin\theta_{L,m}}{4\mu_e^2 + 1} + \frac{4 R_L g \mu_e^2 (\cos\theta_{L,m} - 1)}{4\mu_e^2 + 1} - \frac{2 R_L g (\cos\theta_{L,m} - 1)}{4\mu_e^2 + 1} \right.$$
$$\left. + \left(\frac{6 R_L g}{4\mu_e^2 + 1} - \frac{v_0^2}{\mu_e} \right) (e^{-\theta_{L,m}\mu_e} - 1) - R_L g (\cos\theta_{L,m} - 1) \right]$$

$$(2.46)$$

2.4.2   Erosive wear

To transfer bulk solids from one conveyor belt to the next equipment, the curved impact chute can be utilized. Figure 2.19(a) shows a transfer chute in a belt conveying system [4]. It can be perceived that bulk solids impact against the curved plate. After that the bulk solids are directed onto a conveyor. A dribble chute is applied to collect and transfer cohesive bulk solids that are carried back during the discharging motion. The dimensions and positions of the used equipment are shown in Figure 2.19(b) and Figure 2.20.
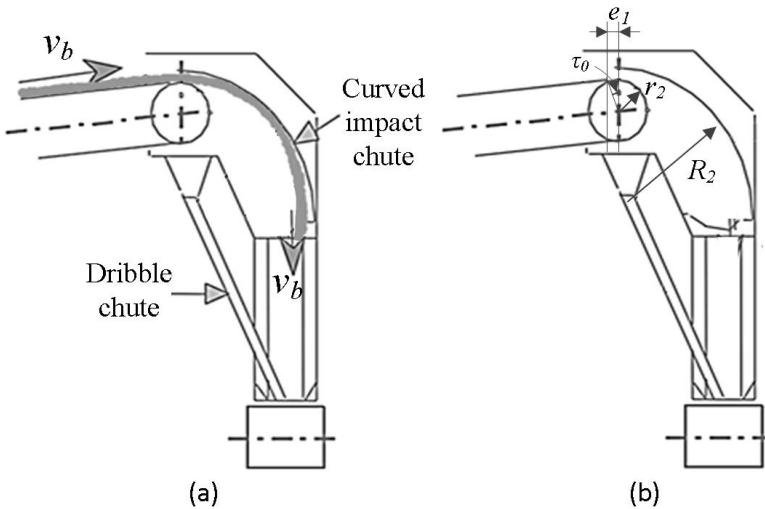
Figure 2.19: Curved impact chute (a) a part of discharging process (b) dimensions and positions of the used equipment [4]

To predict wear volume on the curved impact chute, the bulk flow model is illustrated in Figure 2.20 [4, 67]. It is predicted by the bulk flow model (Figure 2.20) that the rotations of particles can be neglected. Thus, Neilson and Gilchrist's Equation 2.28 and Bitter's Equation 2.27 can be applied to calculate cutting and deformation
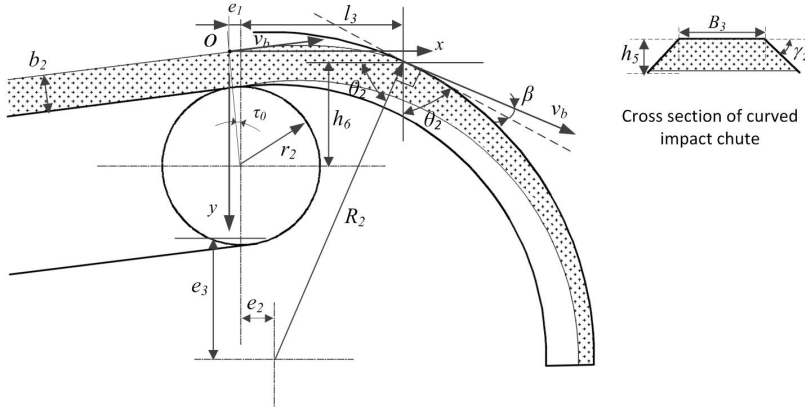
Figure 2.20: Erosive wear on a curved impact chute [4]

wear volumes. By applying Equation 2.28 and Equation 2.27 to Equation 2.30, it obtains,

for $\beta \leq \beta_0$,

$$W_{V,e} = \frac{m_b v_b^2 \cos^2\beta \sin(k_0\beta)}{2\varepsilon_c} + \frac{m_b(v_b \sin\beta - v_e)^2}{2\varepsilon_d} \tag{2.47a}$$

for $\beta \geq \beta_0$,

$$W_{V,e} = \frac{m_b v_b^2 \cos^2\beta}{2\varepsilon_c} + \frac{m_b(v_b \sin\beta - v_e)^2}{2\varepsilon_d} \tag{2.47b}$$

Substituting m_b with q_b, the following Equations 2.48(a-b) are used to express the wear rate (wear volume per second) on the impact chute.

for $\beta \leq \beta_0$,

$$Q_{q_b,e} = \frac{q_b v_b^2 \cos^2\beta \sin(k_0\beta)}{2\varepsilon_c} + \frac{q_b(v_b \sin\beta - v_e)^2}{2\varepsilon_d} \tag{2.48a}$$

for $\beta \geq \beta_0$,

$$Q_{q_b,e} = \frac{q_b v_b^2 \cos^2\beta}{2\varepsilon_c} + \frac{q_b(v_b \sin\beta - v_e)^2}{2\varepsilon_d} \tag{2.48b}$$

in which v_e is given by Equation 2.27. By neglecting air drag force, the impact velocity v_p can be expressed by,

$$v_p = \sqrt{v_{p,x}^2 + v_{p,y}^2} = \sqrt{v_b^2 \cos^2\tau_0 + \left[\frac{g_0(x_0 + e_1)}{v_b \cos\tau_0} - v_b \sin\tau_0\right]^2} \tag{2.49}$$

where e_1 is calculated by,

$$e_1 = (r_2 + h_6)\sin\tau_0 \tag{2.50}$$

The impact angle β can be obtained from,

$$\beta + \theta_2 = \arctan \frac{v_{p,x}}{v_{p,y}} = \arctan \frac{v_b \cos \tau_0}{g_0(x_0 + e_1)/(v_b \cos \tau_0) - v_b \sin \tau_0} \tag{2.51}$$

in which θ_2 is known by,

$$\theta_2 = \arctan \frac{h_6 + r_2 + e_3}{l_3} \tag{2.52}$$

The cutting and deformation factors (ε_c and ε_d) in the Equation 2.48 are assumed to be constant [64]. The deformation wear factor ε_d can be determined from the wear loss at 90° impact angle by using Equation 2.53,

$$\varepsilon_d = \frac{\rho_e m_b (v_p \sin \beta - v_e)^2}{2W_{M,b,d,d}} \tag{2.53}$$

By applying the obtained deformation wear factor ε_d, the deformation wear at a given angle can be determined by using Equation 2.29. Thus the cutting wear volume can be obtained by subtracting the deformation wear from total wear loss using Equation 2.30b). Finally, the cutting factor is calculated by Equation 2.54,

$$\varepsilon_c = \frac{\rho_e m_p v_p^2 \cos \beta}{2(W_{M,d,p,e} - W_{M,d,p,d})} \tag{2.54}$$

In summary, this section illustrates two examples respectively of predicting abrasive and erosive wear of bulk solids handling equipment surfaces. To estimate the wear in practice, all parameters in theoretical equations must be determined. To do so, wear test apparatuses are used to analyze wear parameters.

2.5   Wear test apparatus

This section summarizes the most commonly used apparatuses for abrasive and erosive wear tests by single particle and bulk solids based on bulk solids handling conditions. To find out appropriate wear apparatus for performing test, the advantages and disadvantages of each apparatus are discussed.

2.5.1   Abrasive wear test apparatus

Figure 2.21 illustrates a pin-on-disk tribometer [68] that can be used to obtain sliding wear loss of a sample surface by single particle. The wear tester consists of three parts: operating computer, pin-on-disk device and infrared camera. The operating computer is to operate the pin-on-disk device and infrared camera. The

pin-on-disk device is designed based on standard test method [69] for conduct-
ing particle sliding wear test. The infrared camera is used to capture the dynamic
temperature on the tested sample.
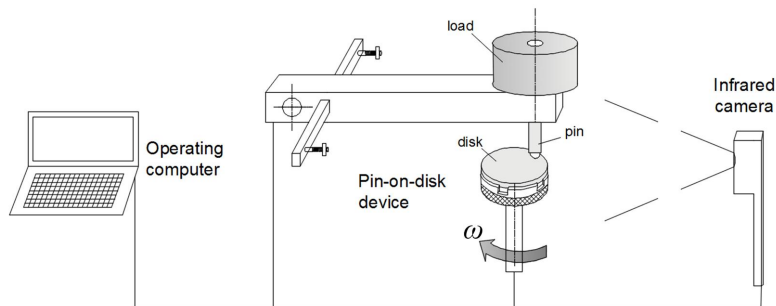
Figure 2.21: Schematic of a pin-on-disk tribometer

The advantages of this wear test apparatus are summarized as follows.

(1) Wear can be obtained at any given distances.

(2) Wear by various particle shapes can be measured.

(3) The friction force and particle penetration depth can be recorded.

(4) The temperature variances on certain area of disk surface can be monitored by
    the infrared camera.

Two disadvantages of this wear test apparatus are:

(1) To avoid severe vibrations, the applied maximum sliding speed is lower than
    that of the bulk solid speed in practice.

(2) The temperature rise is influenced by environmental conditions.

To measure abrasive wear by bulk solids, the linear belt [21, 70, 71] and the circle
bed wear test apparatuses [72] are widely used. The linear belt wear test appara-
tus is shown in Figure 2.22 [21]. It is built on the basis of a belt conveying system.
A storage bin is used for continuous supply of bulk solids. A bucket elevator as
well as a return chute is used to collect and reuse the bulk solids. The normal load
originates from the weight on the sample holding bracket. The shear forces are
monitored by a shear load cell [72].

The advantages of this linear belt wear test apparatus are [72]:

(1) It continuously supply a random collection of bulk solids to the underside of
    the test specimen;

(2) A small proportion of bulk material compared to the total is used for wearing specimen;

(3) Constant belt velocity is achieved under the test specimen.
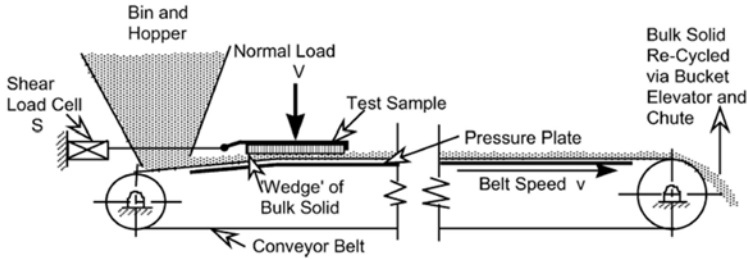
Figure 2.22: Linear belt wear test apparatus [21]

The disadvantages of the linear belt wear test apparatus are given as follows [72].

(1) It lacks operation reliability (e.g. inconstant flow of the wear media in the feed bin);

(2) Wear media changes due to the involvement of contaminants;

(3) Wear media can also degrade;

(4) Dust and spillage is triggered;

(5) Wear media depth can be too small to enable self alignment of the particles.

The circle bed wear test apparatus presented in Figure 2.23, which is available in the university of Newcastle, Australia. In this tester, the rotating annular bed is used to transport bulk solids and provide the wear velocity. Moderate loads can be applied on the test sample via a counterweighted load-arm. A passive plough and a grading mixing system are used to sufficiently mix the wear composites and a passive consolidator to increase density of bulk solids. The mechanical power and various velocities are provided by the hydraulic drive [72].

The circular bed wear test apparatus also has the first two advantages that the linear belt has. Besides, it has the following advantages [72]:

(1) It has a high factor of reliability due to usage of single drive unit;

(2) It causes relatively low production of dust, noise and spillage;

(3) It is convenient to clean after test and thus avoid introducing contaminants;

(4) A small amount of wear media is required to conduct a test;

(5) A wide range wear velocity can be achieved.

Figure 2.23: Circle bed wear tester [72] (picture provided by G. Lodewijks)

The disadvantages with the circular bed wear test apparatus are [72]:

(1) It is difficult to determine the maximum normal load that can be applied to the specimen holder;

(2) The bed speed has a variation of approximately ±7 %;

(3) Much dust can be produced at high speeds.

2.5.2   Erosive wear test apparatus

Figure 2.24 shows a test apparatus to measure impact wear by single particle [66]. This test apparatus consists of a gas reservoir, a fast acting valve, a launch tube, a stopping plate and a target assembly. The target assembly contains the sample holder which is to be impacted by single particle. An acrylic piston is applied to direct the accelerated particles to impact the sample holder. A transducer is used to measure the projectile velocity. To minimize gas cushioning in front of the piston, a vacuum pump is fixed at the target assembly end to the launch tube.
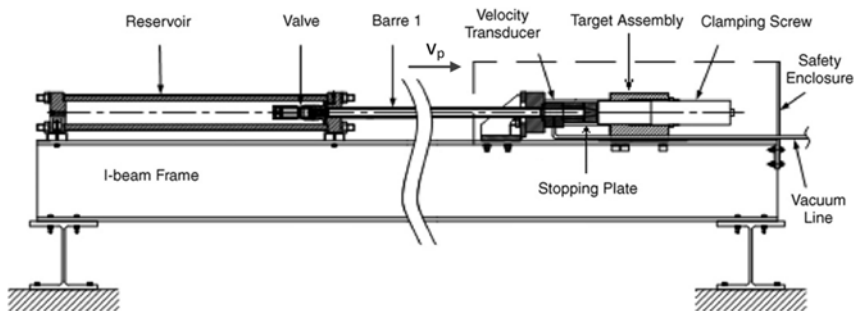
Figure 2.24: Schematic of a gas gun used for performing particle impact [66]

The advantages of this tester are:

(1) Any desired impact angle can be achieved by rotating the sample holder;

(2) No hazard occurs to environment when pure nitrogen gas is used;

(3) Particle velocity can be accelerated to a very high level (up to 600 m/s).

The disadvantages of this tester are:

(1) Pretests are required to obtain consistent impact velocity;

(2) It is difficult to accurately adjust particle velocity, and thus in each test multiple particles are used to achieve identical impact velocity.

The most frequently used apparatuses for measuring erosive wear by bulk solids are the gas-blast [73–75] and the centrifugal accelerator [76]. Figure 2.25 shows the gas-blast erosive wear test apparatus. This apparatus contains a boron carbide nozzle to guide the impacting particles. A screw feeder is used to feed bulk solids into the injector housing. The target holder is mounted on a rotational table to achieve an adjustable impact angle. Two control valves are used to adjust the acceleration of bulk solids. One is used to control the dispersion of bulk solids and the other is to control the speed of bulk solids by adjusting the capacity of the used gas [73].
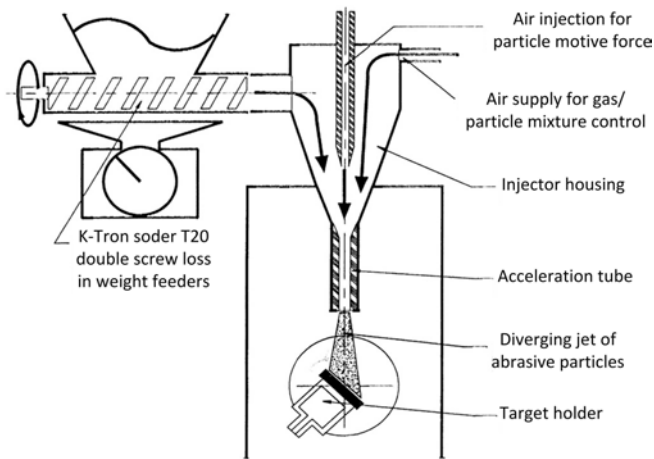
Figure 2.25: Gas-blast erosive wear test apparatus [73]

The advantages of gas-blast erosive wear test apparatus are [73]:

(1) The test duration is relatively short;

(2) Few controllable parameters and thus results analysis is simple.

The disadvantages of this gas-blast test apparatus are [73]:

(1) It is difficult to assess when steady-state impact begins;

(2) It is difficult to assess particle velocity;

(3) It causes high influences of adverse gas on particle motions

(4) For each test, wear takes place solely for one impact angle.

(5) It is difficult to model high capability of particle concentration.

The centrifugal-accelerator erosion test apparatus is shown in Figure 2.26 [73, 74]. This test apparatus consists of a balanced disc whose rotating velocity can be varied continuously. A mechanical arrangement ensures even splitting of the abrasive flow into six acceleration tubes respectively for six target specimens. Bulk solids can be fed by using a vibratory feeder [73] or a conical hopper feeder [74].
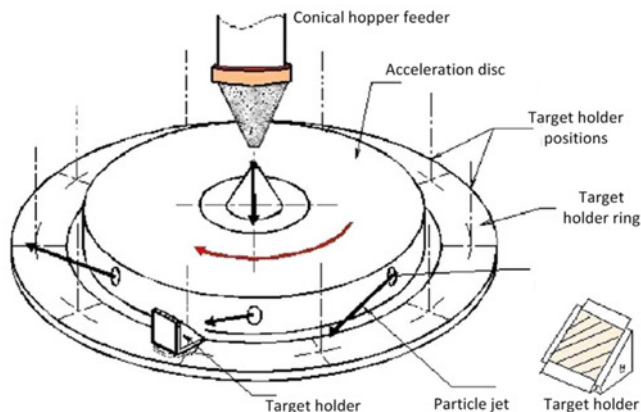
Figure 2.26: Centrifugal-accelerator erosive wear test apparatus [74]

The advantages of the centrifugal accelerator test apparatus are [74],

(1) Multiple tests on several target specimen and different impact angles can be carried out simultaneously;

(2) Impact velocity can be simply determined;

(3) A reasonable range of particle concentration capacity can be achieved;

(4) The influence of gas on particle motions is minimal;

(5) Steady-state erosion conditions can be easily determined.

The disadvantages of centrifugal accelerator test apparatus are [74]:

(1) It is difficult to assess the mass of bulk solids that strike each target;

(2) Test duration is long because of the time to check erosion history of each target.

Thus far the most commonly used wear test apparatuses used in bulk solids handling are compared. Choice of wear apparatus for determining a wear parameter depends on the bulk solids handling conditions and selected wear equations.

2.6   Limitations of evaluating practical wear

Using the analytical wear models to predict wear in bulk solids handling, the limitations of the following five points must be considered. They are: the bulk solids, equipment surface, wear conditions, failure types and wear test apparatuses.

(1) Wear models are based on generalized characteristics of bulk solids. Bulk solids normally have a variety of particle shapes, which trigger different contact area and contact stress. Moreover, the degradation and segregation of bulk solids reduce surface roughness and sizes. These variances are not incorporated in deriving wear equations.

(2) Wear models are based on simplified characteristics of equipment surfaces. The surfaces of equipment are not ideally flat and the material properties are not necessarily homogeneous. Besides, equipment surfaces may suffer from strain hardening during wear process, which makes the wear equations unsuitable.

(3) Wear models cannot fully comprise the variances of wear conditions. For instance, wear models are not capable of accounting for nonuniform properties of bulk flow. Furthermore, the environment factors such as temperature increase, vibrations, etc are not incorporated in the wear equations.

(4) Wear consequences are categorized according to simplified failure types. In this research it is assumed that failure types are either ductile or brittle. However, certain failures are neither ductile nor brittle [58]. Furthermore, all wear equations for brittle failure are based fracture model I, whereas, other failure models are also possible.

(5) Due to the disadvantages with every wear apparatus, experimental tests cannot accurately predict volume loss in regard to bulk solids handling conditions, thus affecting the reliability of determined wear parameters and wear equations.

2.7   Conclusions

To answer the subquestion of *"Which analytical wear models can be used to quantify the surface wear of bulk solids handling equipment?"*, this chapter gives an overview of the wear characteristics in bulk solids handling and available wear models to assess wear of bulk solids. Four conclusions are drawn as below.

(1) In bulk solids handling, two main wear types are identified, namely, the abrasive wear and erosive wear. Both wear types generally trigger ductile failures on the ductile and brittle surfaces of bulk solids handling equipment. However, a brittle surface equipment can also suffer from brittle failures.

(2) With respect to ductile and brittle surfaces, the equations for quantifying absolute wear by bulk solids are developed on the basis of the absolute wear volume loss for single particle. Besides, wear factors can also be used for comparing wear rates by bulk solids.

(3) Based on simplifications of the three aspects, namely, particulate solids, equipment surface and wear conditions, the abrasive and erosive wear in bulk solids handling can be theoretically predicted using analytical wear models.

(4) The parameters for wear equations can be determined by selecting appropriate test apparatuses. Nevertheless, due to disadvantages of wear test apparatuses, discrepancies of parameter determinations by experiments have to be reconciled.

This chapter presented a comprehensive study on the analytical wear models in bulk solids handling. The analytical wear models are used to quantify wear and also to investigate the wear reduction mechanisms in biology. In the next chapter, the potential application of bionic design to reduce the wear in bulk solids handling will be explored.

3 | CHAPTER

Bionic design method for wear reduction in bulk solids handling[*]

Chapter 2 analyzes the abrasive wear and erosive wear models in bulk solids handling. In order to obtain further reduction of the surface wear of bulk solids handling equipment, a new solution must be explored.

This chapter develops a bionic design method for the surface wear reduction of bulk solids handling equipment. In this chapter, section 3.1 summarizes the conventional methods for the surface wear reduction. Section 3.2 characterizes the surface morphologies from biologically wear-resistant surfaces. Section 3.3 illustrates the available bionic models for wear reduction. Section 3.4 formulates a bionic design method for wear reduction in bulks solids handling. Section 3.5 provides two bionic models for the abrasive and the erosive wear reduction, respectively. Finally, the conclusions are presented in section 3.6.

3.1 Conventional methods for wear reduction

The literature on wear reduction of bulk solids handling equipment has highlighted five conventional methods, which are given as follows.

(1) Using theoretical predictions of wear loss to design equipment profiles. For instance, Roberts [4] optimized the curvature of transfer chutes based on the predictions of particle flow trajectories under bulk solids handling conditions;

(2) Utilizing wear-resistant materials or linings to protect equipment surfaces that suffer from severe wear. For example, incorporating a lining component within an impact plate [78].

(3) Adding assistant components to utilize self-wear mechanism by the transported bulk solids. For instance, adding perpendicular ribs on chute bottom relative to bulk flow direction [79, 80], as shown in Figure 3.1 (a).
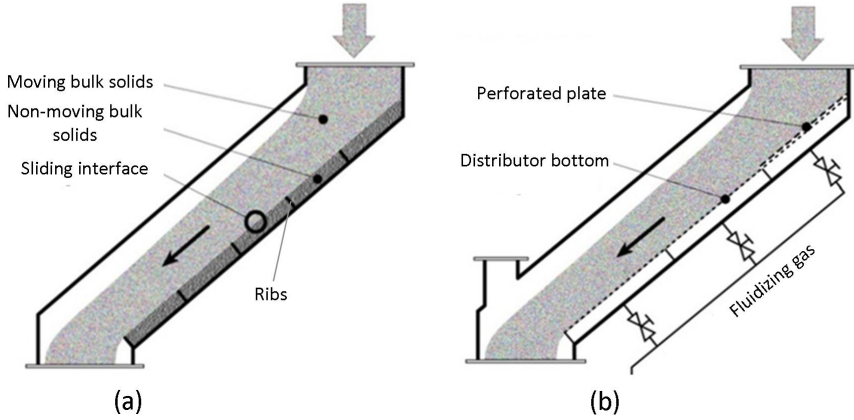
Figure 3.1: Two traditional methods to reduce wear (a) utilizing self-wear mechanism (b) using fluidized gas [79, 80]

(4) Supplying additional power to reduce the contact force between particulate solids and equipment surface. An illustration of supplying air to chute bottom during transporting process is shown in Figure 3.1 (b) [1, 35].

(5) Fabricating surface geometry patterns based on empirical evidence [81, 82]. Figure 3.2 shows wavy ribs on a grab surface, which is assumed to be capable of reducing grabbing resistance with respect to bulk solids [83].
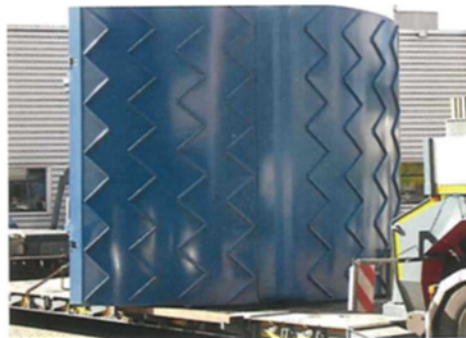
Figure 3.2: Array riblet pattern on the surface of grab [83]

To date, in literature, bionic design method has not yet been used for the surface wear reduction of bulk solids handling equipment. To introduce bionic design method to bulk solids handling for surface wear reduction, the biological wear-resistant surfaces are analyzed in the next section.

3.2 Biologically wear-resistant surfaces

Biological surfaces have optimized characteristics as a result of evolution over millions of years. The surface morphology is an important characteristic for biological organs to reduce wear in accordance with their living environment. This section summarizes the morphologies from biologically wear-resistant surfaces. Moreover, the biologically wear-resistant mechanisms in relation to the surface morphologies are analyzed.

3.2.1 Wear-resistant surface morphologies

The biological wear-resistant surfaces are discovered from the living creatures that inhibit soil [6, 7, 13, 84, 85] and sand environments [40, 86–91]. In biology, due to interactions (e.g., rolling, sliding and impact) between biological surfaces and their living (soil and sand) environments, the biological surfaces are effective in reducing the wear by particulate solids. To develop a bionic design method for wear reduction in bulk solids handling, the biological morphologies are characterized with respect to reducing abrasive wear and erosive wear.

Figure 3.3 presents nine wear-resistant surfaces from several soil and sand living creatures. Figure 3.3(a) shows the convex morphology on the head of a dung beetle [6, 13]; 3.3(b) shows concave morphology on the back of ground beetle [13]; Figure 3.3 (c) shows the ribs on a pangolin scale [7]; Figure 3.3 (d) shows the dorsal body of a desert sandfish [86], which has squama morphology. Figure 3.3 (e) shows the ribs with nodes of a shell surface [84]; Figure 3.3 (f) shows the lamellar micro-ornamentation from a desert snake [40]; Figure 3.3 (g) shows the corrugated scales of desert lizard [92]; Figure 3.3 (h) shows a surface of the back body of a desert scorpion, which has the morphology of intermediate grooves [87]; Figure 3.3 (i) shows the micro-ridges [93], which have nano-spikes between the micro-ridges [94].

As seen in Figure 3.3, the morphologies of these biological wear-resistant surfaces are non-smooth, and are distributed by discrete elements such as convexes [6]. The biological morphologies have sizes ranging from nanometer to millimeter. These non-smooth surface morphologies form the biological structures that can significantly affect wear resistance [13, 14, 85]. In order to apply wear-resistant morphologies to engineering, the underlying wear-resistant mechanisms corresponding to the non-smooth biological morphologies must be analyzed [95, 96].

3.2.2 Biologically wear-resistant mechanisms

Based on the abrasive and erosive wear models in chapter 2, it is postulated that non-smooth morphologies can enable reduction of friction (resistance) and contact forces (stress), thus reducing wear. In the two aspects of abrasive and erosive wear reduction, Table 3.1 presents the wear-resistant mechanisms corresponding to the biological morphologies presented in Figure 3.3.
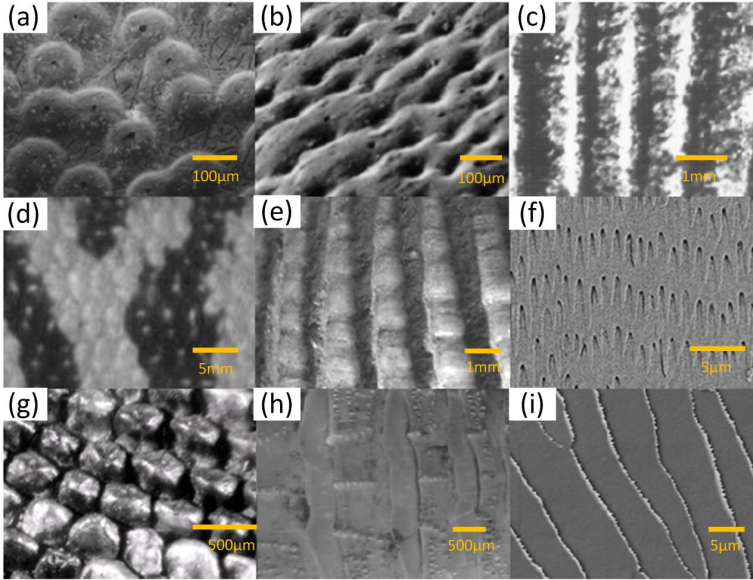
Figure 3.3: Biological wear-resistant surface morphologies (a) convex domes from dung beetle [13] (b) concave pits from ground beetle [13] (c) ribs on a pangolin scale [7] (d) convex scales on the body of a desert sandfish [86] (e) ribs with nodes of a shell surface [85] (f) lamellar micro-ornamentation from a desert snake cite [40]; (g) corrugated scales of desert lizard [87, 92]; (h) grooves on the body surface a desert scorpion [87]; (i) micro-ridges on the scales of sandfish [93, 94]

Table 3.1: Biological morphologies and wear-resistant mechanisms

	Biological morphologies	Wear-resistant mechanisms
Abrasive wear reduction	convex domes and concaves ribs lamellar strips convex scales	reduce adhesion and resistance force [6, 19, 97, 98] generate guiding and rolling effects [7] create friction directionality, reduce stick-slip [40] create friction directionality [8, 11]
Erosive wear reduction	grooves inverted "V" ridges nano-spikes semi-ellipsoidal ridges	decompose particle cutting force [89] reduce cutting force by dispersing particles [93] reduce contact area [94] resist critical stress [94] and enhance particle-particle impact [99]

3.3 Analysis of bionic models for wear reduction

A bionic model can be designed by mimicking an existing natural object, or by modifying nature's model to achieve a desirable function [14]. In order to understand that bionic design can be used for wear reduction, this section illustrates three bionic models for abrasive wear reduction and two bionic models for erosive wear reduction.

3.3.1 Bionic models for abrasive wear reduction

The three bionic models for abrasive wear reduction are the bionic bulldozing plates, bionic disk ploughs and bionic rib models. These three models are designed based on morphologies of convexes, concaves and ribs, which were summarized in Table 3.1.

A bionic bulldozing model [6] is presented in Figure 3.4. To demonstrate the soil resistance reduction of bionic bulldozing plates, experimental tests were conducted using an optimal design method of D-optimum theory [6]. Accordingly, twenty-two bionic bulldozing plates and a conventional (smooth) plate were fabricated. In comparison with the smooth plate, the soil resistance acting on bionic bulldozing plates was reduced by 13% on average. The configuration for the most optimal plate are 7 mm in height and 25 mm in base diameter, 45 in number, and parallelogram arrangement of the convex shapes.[6]. In addition, it is theoretically predicted that a bionic plate of parallelogram arrangement can reduce soil resistance by up to 18%.

The reason for soil resistance reduction is that the convex domes break the continuous forces between soil material and the surface of bulldozing plates[6]. Resultantly, the abrasive wear on tool surfaces can be reduced. In the experimental tests, the particulate solids, worn surface and wear conditions are as follows:
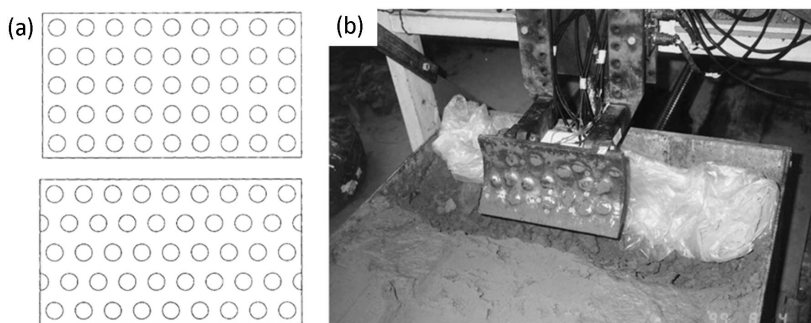
Figure 3.4: Application of convex domes on a bulldozing plate surface (a) geometrical design (b) bionic model [6, 97]

(a) Particulate solids: A clay soil with an average moisture content of 27.8% (dry basis) was used. The particle size distribution of the used soil is shown in Table 3.2.

Table 3.2: Particle size distribution of experimental soil [6]

Size (mm)	> 0.05	0.05-0.01	0.01-0.005	< 0.001
% wt	20.94	18.18	7.91	37.16

(b) Worn surface: Two types of bionic surfaces of rectangle and parallelogram arrangements were designed, which are shown in Figure 3(a). Based on the

ratio of the area occupied by convex domes to the total area 45%, the height and the base diameter of convex dome are set in the range of 2-8 mm and 16-32 mm, respectively. The number of convex domes are in the range of 20-50. The size of the matrix for all bulldozing plates is 400 mm in length and 200 mm in width. All bulldozing plates are made of plain carbon steel.

(c) Wear conditions: The soil-engaging tests were proceeded in an indoor soil bin as shown in the Figure 3.4. The soil resistance was measured using a SR-30C data recorder [6]. During the twenty-two groups of experimental tests, the wear parameters of cut angle, cut depth, forward speed and soil particle size distribution remained constant.

Two bionic disk ploughs [98] are shown in Figure 3.5, which respectively has convex and concave morphologies. To evaluate the soil resistance reduction, nine groups of tests are designed, which include one plain, four convex and four concave disk ploughs with different morphological parameters are designed. These nine tests were carried out in an indoor soil bin. Results showed that for the sliding speeds higher than 0.56 m/s, all the designed bionic disk ploughs have a significant reduction compared to the conventional one. In general, bionic convex disk ploughs give higher reduction compared to concave ones. The maximum reduction of wear was achieved at 19% by a bionic convex disk plough. The corresponding values of geometrical parameters are: convex height 3mm and bionic unit density 30%.

This wear reduction mechanism is attributed to that the non-smooth bionic units of convexes and concaves reduce the contact areas between soil and disk plough surfaces and thus weaken the continuity of soil. As a result, the adhesive forces between soil and the surface of disk plough are reduced [6]. In the experimental tests, the particulate solids, worn surface and wear conditions are as shown below:
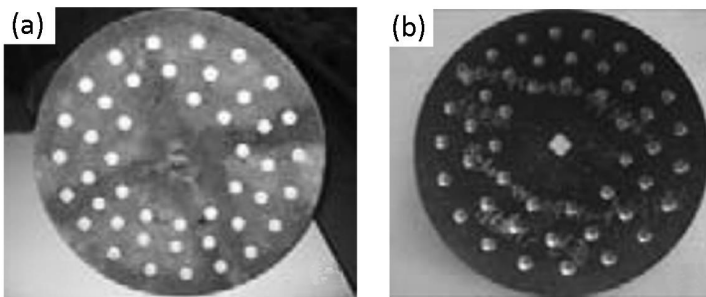
Figure 3.5: Bionic disk ploughs (a) a bionic convex disk plough (b) a bionic concave disk plough [98]

(1) Particulate solids: Black clay soil was used and a proper fitting process was proceeded. The average moisture is 23.25% (dry basis) and the bulk density is 1620 kg/m^3. The particle size distribution of this soil is shown in Table 3.3.

Table 3.3: Particle size distribution of the experimental soil [98]

Size (mm)	> 0.074-0.05	0.05-0.01	0.01-0.005	< 0.005-0.002
Weight (%)	33	42.5	15.5	9

(2) Worn surface: All the bionic units of convexes and concaves for the disk ploughs have the base radius of 10 mm. Both the convexes and concaves on the bionic surfaces have two levels of height, namely, 1 mm and 3 mm. The densities of bionic units have two levels of 10% and 30%. A parallelogram arrangement is utilized as shown in Figure 3.5. All the disc ploughs are made of 65Mn steel. The dimensions for the matrix of the disc ploughs are 440 mm in diameter, 60 mm for concavity and 5.5 mm in thickness.

(3) Wear conditions: In the experiments, the used driving power is an electric carriage which moves on rail tracks. It connects the soil bin from two sides. The speeds of the electric carriage are in the range of 0.3-1.2 m/s. A sensor is applied to measure the horizontal forces acting on disk ploughs. Each test is repeated three times and the average is used. The constant conditions for the experiments contains: tilt angle 15°, disc angle 45° and ploughing depth 150 mm.

A bionic rib model [100] is depicted in Figure 3.6. Abrasive wear tests on the bionic rib surfaces were carried out to investigate the influences of geometrical and wear parameters. Results showed that in general, bionic models with the rib distance less than 30 mm, promote a lower wear rate, in comparison to a conventional smooth surface. Using D-optimum design theory [6], the minimum wear occurred under the conditions of abrasive material sizes of 0.104-0.214 mm, sliding velocity of 1.68 m/s and rib distance of 15.71 mm. Moreover, the wear rate corresponding to the parallel case is lower than that of the perpendicular case [7].

The reason for the abrasive wear reduction is that the movements of particles are guided when the sliding direction is in parallel with the orientation of corrugated ribs, whilst the rolling motions of particles are enhanced when sliding direction is perpendicular. In the experiments, the particulate solids, worn surface and wear conditions are as shown below:
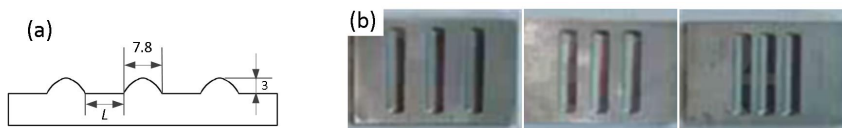
Figure 3.6: Bionic rib surface (a) geometrical design (b) bionic rib samples [100]

(1) Particulate solids: The abrasive material contains 96.5wt% quartz sand and 3.5 wt% bentonite. The average size of bentonite is approximately 0.075 mm. Three sizes of the abrasive material were used: 0.104-0.214 mm, 0.214-0.420

mm and 0.420-0.840 mm, which are shown in Figure 3.7(a-c). The water content is between 3 wt% and 5 wt%.
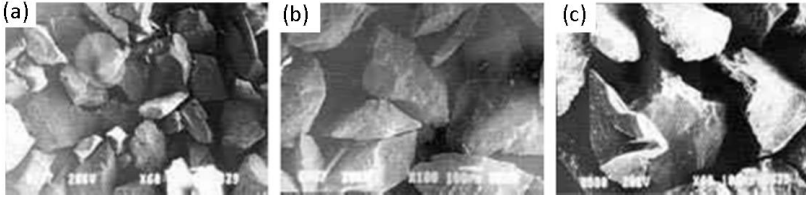
Figure 3.7: Three levels of sizes of particulate solids (a) 0.010-0.21 mm (b) 0.21-0.42 mm (c) 0.42-0.84 mm [100]

(2) Worn surface: Figure 3.6 (b) shows the three bionic rib specimen. The used material for manufacturing worn samples was plain carbon steel. The rib intervals of three samples are 15.71mm, 12.56mm and 9.42mm, respectively.

(3) Wear condition: The tests were carried out on an abrasive wear tester as illustrated in Figure 3.8. In the experiments, bionic models were fixed on the holders and a full sliding distance of 820m was assigned. For each sliding distance, of 420 m, half of abrasive material is replaced with fresh one. The submerging depth of the specimen was 70mm. The impingement angle of the abrasive materials against specimen varied within 33°-37°. Three relative sliding velocities were 1.68m/s, 2.35m/s and 3.02m/s, respectively.
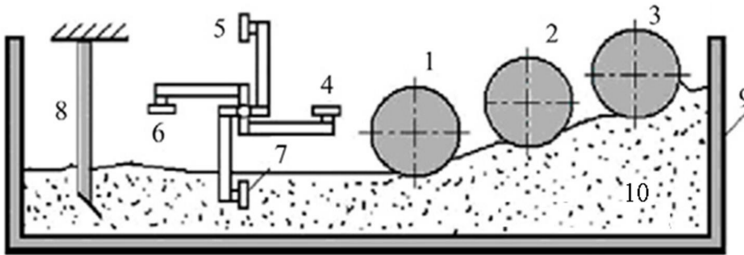
Figure 3.8: Schematic of abrasive wear tester (1-3: compacting wheels; 4-7: bionic specimens; 8: assistant mixer; 9: circular rotary container 10: bulk solids) [7]

3.3.2   Bionic models for erosive wear reduction

The bionic models that utilize biological morphologies for erosive wear reduction are bionic ridge surface and bionic groove surface, which were designed respectively based on ridge morphology and the intermediate groove morphology as summarized in Table 3.1.

A bionic ridge model [93] is displayed in the Figure 3.9. To verify the ability of erosive wear reduction, a bionic ridge surface and a conventional flat surface

were prepared. The experimental results showed that the eroding material of sand grains maintained continuous flow motion on the bionic ridge surface area whereas the sand grains suspended motion at the conventional flat surface. Thus indicates that the bionic ridge surface promotes lower friction than the flat surface with respect to particulate solids.
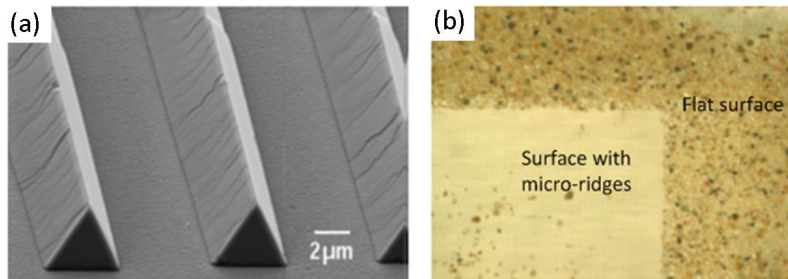
Figure 3.9: Application of ridge morphology (a) bionic model (b) comparison between bionic ridge surface and a flat surface [93]

The reason for the lower friction is that the ridges can dissipate the contact force applied by the bulk flow of eroding particles, thus that the bionic ridge surface can suffer less erosive wear than the flat surface. In the experiments, the particulate solids, worn surface and wear conditions are as follows:

(1) Particulate solids: The used abrasive material to erode the bionic specimen is sand grains as shown in Figure 3.9(b). These sand grains have average particle size of 0.25 mm and were collected from the Sahara desert.

(2) Worn surface: Figure 3.9(a) shows the scanning electron microscopy (SEM) image of the bionic micro-ridge surface. Epoxy polyoxymethylene was used to fabricate an area of 10 mm × 10 mm with uniform morphology of inverted "V" ridges. Besides, an area of conventional flat surface was prepared (seen in Figure 3.9(b)).

(3) Wear condition: A sandblasting cannula was used to continuously supply sand grains. The sand grains fell onto the inclined tested surface, and flew over both fabricated bionic ridge surface and non-treated flat surface. The sliding characteristics of the sand grains on the bionic surface were accurately observed by a digital microscope.

A bionic groove model [89] is depicted in Figure 3.10. To verify the erosive wear reduction ability, simulations studies were carried out, by which it was demonstrated that the contact pressure for low particle impinging angle was significantly reduced due to the disturbances from grooves. At the impact angle of 30° and using the eroding material of silica sand of 150 μm particle size, the experiments based on D-optimum theory were conducted to investigate the significance of geometric parameters (groove height (H), groove distance (D) and groove width (W)) on wear rate and optimize the bionic model. The experimental results showed

that the significance of the geometric parameters was in the order of H, D and W. The lowest erosion rate was the combination of D=2mm, W=5mm and H=4 mm.

The reason for erosive wear reduction is that the contact pressure for low particle impinging angle was significantly reduced for the particle impacts at low impacting angles. The bionic surface, particulate solids and wear conditions are:
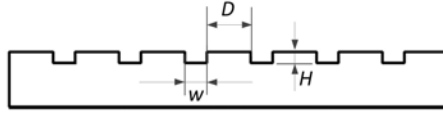
Figure 3.10: Geometrical design of a bionic groove model [93]

(1) Particulate solids: The eroding material of dry silica sands is shown in Figure 3.11, which has average particle diameter equal to 150 μm.
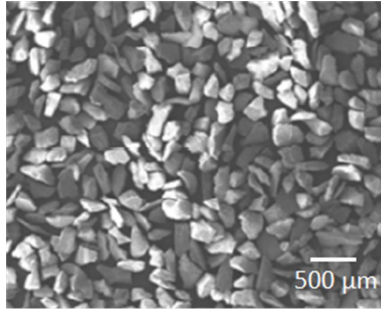
Figure 3.11: Eroding material of Silica sands [91]

(2) Worn surface: The dimensions of the rectangular matrix of the bionic specimen (Figure 3.10 are 50 mm $\times$ 50 mm $\times$ 5 mm. The groove height (H) and groove distance (D) are both in the range of 2-4mm, and the groove width (W) is in the range of 3-4 mm. The bionic specimen are made of mild steel.

(3) Wear conditions: The schematic illustration of the used erosion test rig is shown in Figure 3.12. Preliminary experiments indicated the weight loss of bionic samples reached steady state after $10-15$ minutes erosion duration. Therefore in each test the sample was initially eroded for 15 minutes. Then wear loss for a five minutes test period was measured by using an electronic balance under the accuracy of ±0.01mg. The pressure of the air compressor was 0.5 MPa. Through all tests, the eroding material of silica sand and eroding material injection angle remained constant.

To sum up, this section analyzes the available bionic models for abrasive wear and erosive wear reduction. It demonstrates that bionic models can be applied for surface wear reduction with respect to particulate solids. Based on the similarity that bulk solids handling equipment surfaces also suffer from wear by particulate solids, the application of bionic design in bulk solids handling will be discussed.
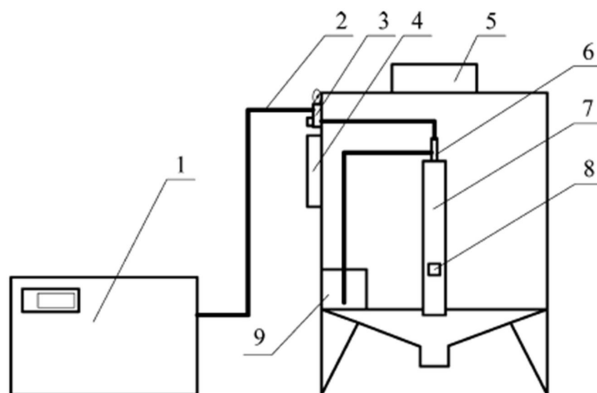
Figure 3.12: Schematic illustration of erosion test rig: 1: air compressor; 2: air pipe; 3: pressure control valve; 4: control box; 5: dust collector; 6: blast gun; 7: nozzle; 8: sample holder; 9: particle container [89]

3.4 Bionic design for bulk solids handling equipment

To introduce bionic design to bulk solids handling for surface wear reduction, this section compares the wear characteristics between biology and industries. Besides, the available bionic design methods are reviewed and a bionic design method for surface wear reduction of bulk solids handling equipment is developed.

3.4.1 Wear characteristics in biology and industries

Table 3.4 compares the three wear aspects from biology to agricultural industry and bulk solids handling industry. From Table 3.4, it is identified that both biology and bulk solids handling deal with dry particulate solids under wear conditions of high speed and high pressure. In combination with the similarities between bulk solids handling industry and agricultural industry which already adopted bionic design, the potential applicability of bionic design for wear reduction of bulk solids handling equipment surfaces is demonstrated.

3.4.2 Review of bionic design methods

Fourteen systematical bionic design methods are found from available literature [14, 20, 95, 101–111]. Two of them start from a biological solution, which are categorized as solution-based. These two methods are summarized in Table 3.5. The remaining twelve bionic design methods begin with a problem analysis, which are characterized as problem-based. These twelve methods are summarized in Table 3.6.

Table 3.4: Wear characteristics in biology and industries

	Particulate solids	Worn surface	Wear conditions
Biology	wet and dry particles, sizes from fines to lumps, e.g. soil and sand	non-smooth composed by discrete elements, e.g. convexes, concaves	biologic organs actively and passively engaging with solids, low and high speeds, low contact pressure
Agricultural industry	moist or semi -viscous soil, fine sizes	mostly smooth or flat metals, sizes of meters	instruments actively engaging with solids, low speed, and low contact pressure
Bulk solids handling industry	dense dry and moist solids, sizes from fines to lumps	mostly smooth or flat metals, sizes of meters	instruments actively engaging with particles, low speed; low and high contact pressure

Table 3.5: Two bionic design methods that are solution-based

Colomb [101]	Helms et al. [102]
Analysis	Biological identification solution
Transformation	Define the biological solution
Implementation	Principle extraction
Product development	Reframe the solution
	Problem search
	Problem definition
	Principle application

Table 3.6: Comparisons of twelve bionic design methods that are problem-based

Junior et al. [103, 104]	Gramman [105, 106]	Hill [107]	Vincent et al. [14]
Identification of need	Formulate	Analyze contradiction	Define the problem
Selection and sampling	Search and assign solution	Identify biological structure	Analyze and understand
Observation of the sample	Analyze biological system	Analyze biological structure	Compare and find solutions
Analogy analysis	Evaluate the system	Transfer solution	Connect nature and technology
Implementation of design	Implement	Vary and combine	Create new system or product
		Select the best solution	
		Elaborate the solution	

Sartori, et al. [106]	Hastrich [108]	Gebeshuber et al. [20]	Helms et al. [102]
Identify required function	Identify /Distill	Problem definition	Identify requirements
Identify conditions	Translate	Reframe the problem	Biologize the function
Find a biological solution	Discover	Biological solution search	Find nature's best practice
Identify function principle	Abstract	Define the biological solution	Generate design ideas
Identify biological structure	Emulate	Principle extraction	
Utilize the structure	Evaluate	Principle application	
Adapt the solution			

Lenau [109]	Nagel et al. [95]	Kilmer [110]	Kore et al. [111]
Search	Identify	State	Combine requirements and nature inspirations
Analysis	Understand	Collect	Structures selection
Principles	Define question	Analyze	Document data
Design	Select morphology	Ideate	Principle
Evaluate	Define scale	Choose	Bionic modeling and refine
	Define functional model	Implement and construct	Simulation analysis
	Validate	Evaluate	

3.4.3   Bionic design method for surface wear reduction

According to Table 3.5 and Table 3.6, all the bionic design methods have either explicitly or implicitly incorporated the bionic design principle of biological function analysis. To develop a bionic design method for wear reduction of bulk solids handling equipment, the problem-based methods (Table 3.6) can be referred. More specifically, the bionic design method derived by Nagel et al. [95] and by Kore et al. [111] can be applied to transfer biologically wear-resistant morphologies to bulk solids handling equipment surfaces. In addition, the 40 inventive principles of TRIZ [112] [14, 113] and D-optimum theory [6, 89] are based on the analysis of available bionic models.

Figure 3.13 shows the bionic design method for surface wear reduction of bulk solids handling equipment. It consists of five steps, which are illustrated below.

Step (1): Search for bio-inspirations in biology where biological systems confront similar situations. One can also refer to the available text book to seek for biological functions [114];

Step (2): Analyze biological function mechanisms and extract the functional elements [115];

Step (3): Propose wear-resistant model (bionic model) based on the function mechanisms in biological system, or using the inventive principles of TRIZ [112];

Step (4): Define the geometrical size of the bionic model in correspondence to industrial levels;

Step (5): Evaluate and optimize the proposed bionic models with respect to practical conditions.
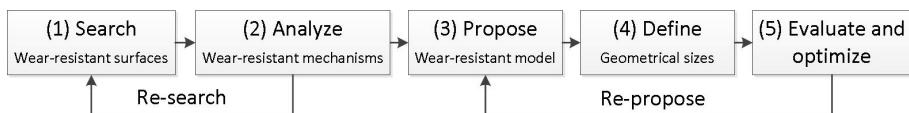
Figure 3.13: Bionic design method for wear reduction in bulk solids handling

Figure 3.13 points out two feedback processes, of which Re-search is used when a selected wear resistant mechanism proves difficult in application, and Re-propose can be required once a bionic model is unsatisfying.

3.5   Bionic models for surface wear reduction

In Chapter 2, an abrasive wear scenario and an erosive wear scenario in a belt conveying system are illustrated in Figures 2.17 and 2.19. Using the proposed bionic design method, this section presents the bionic models for reducing the surface wear of bulk solids handling equipment.

3.5.1   Bionic model for abrasive wear reduction

Based on the five procedures of the bionic design method in Figure 3.13, a bionic model for reducing the abrasive wear of bulk solids handling equipment is proposed, which is illustrated below.

Step (1): Search for the abrasive wear resistant phenomena in biology. Table 3.1 shows several biological morphologies which can be used as bio-inspirations.

Step (2): The wear reduction mechanisms from several biological morphologies are also presented in Table 3.1. For handling iron ore dry material, the function principle of creating friction directionality by using convex scales is utilized (Figure 3.14.)

Step (3): To propose a bionic model that can effectively reduce abrasive wear, the directionality can be enhanced by creating a new dimension using TRIZ [112] innovative principle of *"Transition into a new dimension"*. Hence the geometrical design of parallelogram arrangement of semi-ellipsoids (similar to the convex scales on sandfish body surface [11]) is proposed. Thus the bionic model for abrasive wear reduction is designed as shown in Figure 3.15.
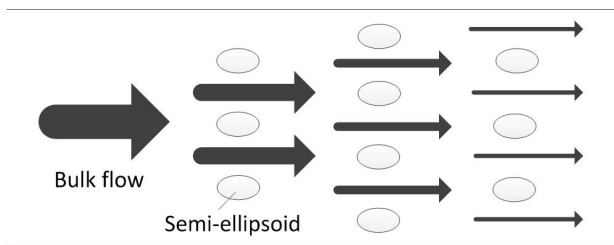
Figure 3.14: Increasing friction directionality by applying semi-ellipsoids
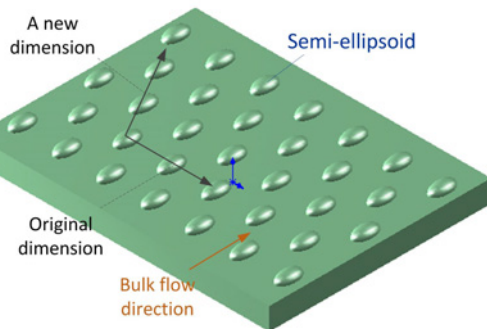
Figure 3.15: Bionic model for abrasive wear reduction

Step (4): Due to significant variation between the sizes of biological morphologies and those of bulk solids handling, the geometrical parameters ($a_0 - d_0$ in Figure 3.16) for the bionic model must be investigated.
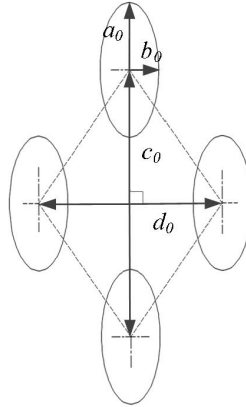
Figure 3.16: Geometrical parameters of bionic model for abrasive wear reduction

Step (5): To evaluate the wear abilities of the bionic model, experimental tests can be used with the application of D-optimum theory [6]. Alternatively, the numerical simulations based on discrete element method (DEM) can be used to predict abrasive wear by bulk solids [116].

3.5.2   Bionic model for erosive wear reduction

Following the five procedures as shown in Figure 3.13, a bionic model for reducing erosive wear of bulk solids handling equipment is elucidated as follows.

Step (1): Search for the erosive wear resistant phenomena in biology. Table 3.1 also summarizes the biological morphologies which can be used for erosive wear reduction.
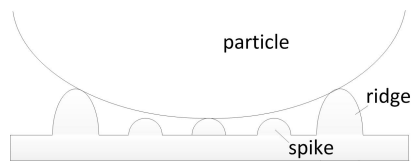
Figure 3.17: Wear reduction by reducing contact friction based on [94]

Step (2): The erosive wear reduction mechanisms from three biological morphologies are presented in Table 3.1. For the handling of dry material iron ore, the wear reduction mechanisms by the spikes and ridges are utilized, which are: the spikes reduce contact friction whereas the semi-ellipsoidal ridges prevent the occurrences of exceeding critical stress [94]. This friction reduction mechanism is illustrated in Figure 3.17. In addition, it is predicted that the ridges can enhance particle-particle impacts by changing particle behaviors, which is illustrated in Figure 3.18. Due to the energy absorption by particles, the impact energy and thus erosive wear of equipment surface can be reduced [99].
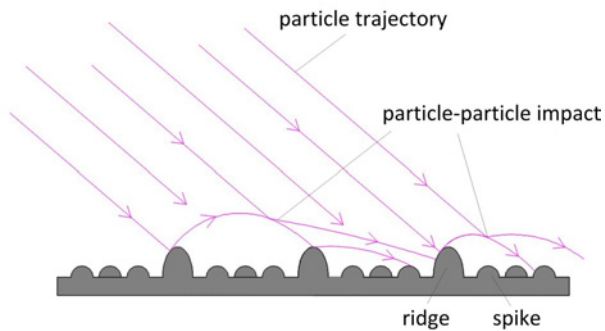
Figure 3.18: Wear reduction by enhancing particle-particle impacts, based on [99]
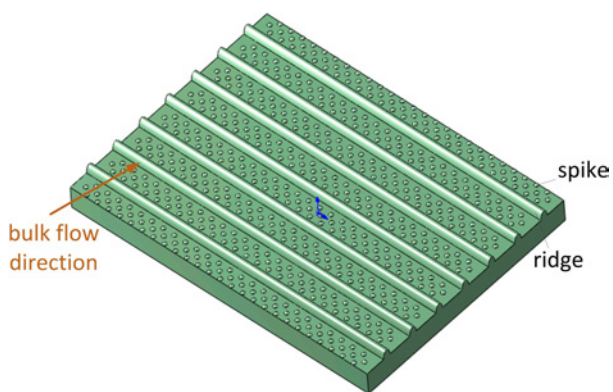
Figure 3.19: Bionic model for erosive wear reduction
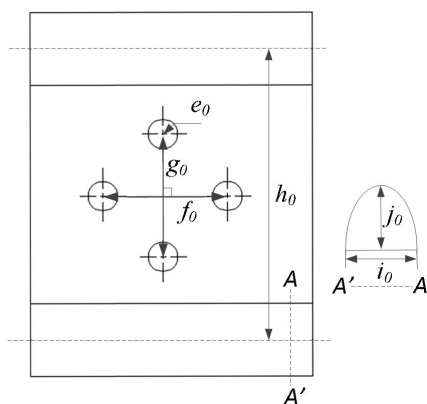
Figure 3.20: Geometrical parameters of bionic model for erosive wear reduction

Step (3): Based on the wear reduction mechanisms (Figures 3.17 and 3.18), the bionic model composed of convex spikes between ellipsoidal ridges is proposed, which is shown in Figure 3.19.

Step (4): To evaluate the ability of erosive wear reduction, the geometrical parameters for the proposed bionic model must be studied. These geometrical parameters $(e_0 - j_0)$ are shown in Figure 3.20.

Step (5): Similar to the prediction of abrasive wear, both experimental [6] and simulation [117] techniques can be utilized.

3.6   Conclusions

To answer the subquestion of *How to develop a bionic design method to reduce the surface wear of bulk solids handling equipment?*, this chapter introduces bionic design and analyzes the potential application of surface wear reduction of bulk solids handling equipment. Four conclusions are drawn as follows:

(1) The biological morphologies from biological wear-resistant surfaces are non-smooth, which have important effects on the ability of wear reduction. The wear-resistant mechanisms provide possible solutions for surface wear reduction of bulk solids handling equipment.

(2) The available bionic models used for wear reduction can be analyzed from three aspects: bionic surface, particulate solids and wear conditions. The experimental validations demonstrate that both abrasive and erosive wear reduction can be achieved using biological morphologies.

(3) The analogies of wear aspects from biology to agricultural and bulk materials handling industries are identified. This indicates significant potential for using bionic design for wear reduction of bulk solids handling equipment surfaces.

(4) In combination with the analysis of the available bionic design methods, a bionic design method is formulated for the wear reduction of bulk material handling equipment. In addition, two possible bionic models, for reduction of abrasive and erosive wear respectively, are proposed.

This chapter presents two bionic models for reducing the abrasive and erosive wear of bulk solids handling equipment surfaces. To be able to use DEM to model the wear of bionic surfaces, material and contact parameters are required to determined. In the next chapter, the tests to determine these parameters are illustrated.

4 | CHAPTER

Experimental studies for determinations of DEM parameters[*]

C hapter 3 introduced DEM as a numerical technique that can be used to model wear in bulk solids handling systems. To achieve realistic wear prediction using the DEM simulations, the input values of the DEM model must be determined. Therefore, experimental tests for determining DEM parameters are required.

This chapter presents three tests for evaluating materials and contact parameters of iron ore and mild steel. In detail, section 4.1 provides the hardness tests for iron ore and mild steel. Section 4.2 describes the pin-on-disk wear tests. Section 4.3 elaborates on the inclining surface tests. Finally, conclusions are given in section 4.4.

4.1 Hardness test

Hardness is the surface ability of resisting mechanical deformations subjected by an indenter applied by comprehensive forces [28]. The hardness of a material is a crucial factor for estimating wear [37].

In the iron ore supply market, Sishen is one of the most demanded ore types due to its high percentage of iron oxides that are used for manufacturing steel products [23]. Many pieces of bulk solids handling equipment are made of mild steel. Therefore it is interesting to study the wear of mild steel caused by Sishen particles. For this, the hardness of Sishen particles and mild steel will be measured.

---

[*]This chapter is based on Guangming Chen, Yueting Liu, Gabriel Lodewijks, and Dingena L Schott. Determination of the coefficient of sliding wear under iron ore handling conditions. *Under review*

4.1.1   Vickers hardness test

The Vickers hardness test is widely used for measuring the hardness of metals [28]. Figure 4.1 (a) displays a hardness tester that can be used to perform Vickers test [119]. This tester has a wide load range of 0.098 N to 98 N, and is used to measure micro and macro hardness subjected to small and large loads. [119]. Figure 4.1 (b) presents the schematic of Vickers hardness test. The Vickers indenter is a square-based diamond cone with an angle of 136°. The Vickers hardness number (H_v) is determined by the load over the surface contact area of indentation, and is expressed by Equation 4.1 [28].
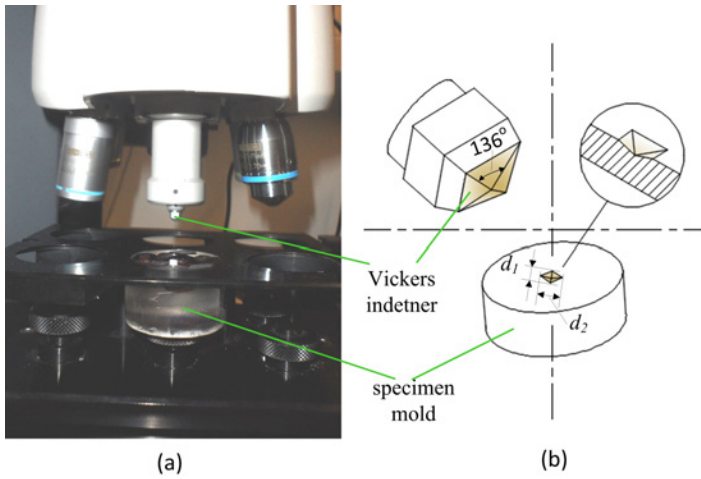
Figure 4.1: Vickers hardness test (a) lab apparatus and (b) schematic illustration [119]

$$H_v = \frac{2F_p \sin(136^o/2)}{d_a^2} \approx 0.0182 \times \frac{F_p}{d_a^2} \tag{4.1}$$

where F_p is the normal load applied on a test surface and d_a is the arithmetic mean of the two diagonals, i.e, $d_a = (d_1 + d_2)/2$.

4.1.2   Sample preparations

To accurately measure hardness, the surfaces of iron ore particles and mild steel must be prepared through grinding and polishing. The tested Sishen particles are selected from the sample which is shown in Figure 2.1 [23]. Based on the particle size distribution and the median size d_{50} = 3 mm [23], two groups of Sishen particles, namely, big and small are chosen as shown in Figure 4.2.

For conveniently grinding and polishing, each group of particles are glued in a mold. Thus two molds are made as shown in Figure 4.3. grinding, the grit sizes

of the utilized sandpapers are subsequently 80, 160, 320, 800, 1200 and 2400 ranging from course to fine. To efficiently clear off the scratches made by the previous sandpaper, the mold is rotated by 90° each time a sandpaper is applied. For polishing, two surface roughness, namely, 3μm and 1μm are subsequently applied. In the same way, a mild steel surface is prepared. Figures 4.3 and 4.4 show the prepared iron ore particle and mild steel surfaces for hardness test.

(a)   (b)
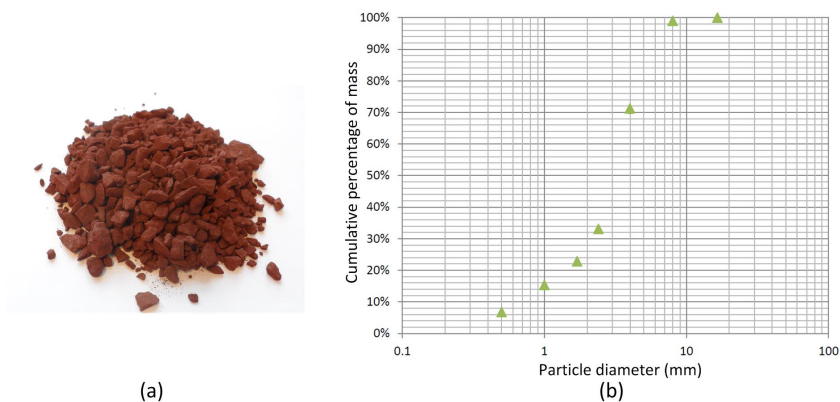
Figure 2.1: A sample of bulk solids (a) Sishen iron ore (b) particle size distribution [23]

Figure 4.2: Two selected groups of Sishen particles

4.1.3   Surface examination

A visual of the surface of the prepared Sishen iron ore particle sample before the Vickers hardness test is shown in Figure 4.5(a), in which the white color represents the inner material of the apparent surface texture, whereas the dark denotes the gaps. It indicates that Sishen particle has porous nonuniform inner structure. Additional imply that the texture varies with locations of an apparent surface and thus also with particles. The inner structure of mild steel is quite compacted and uniform.
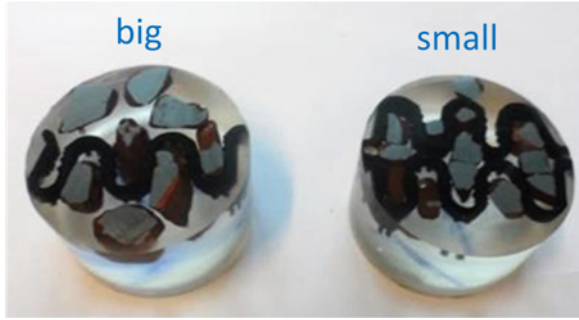
Figure 4.3: Iron ore particles after milling and polishing

Figure 4.4: A mild steel surface after milling and polishing
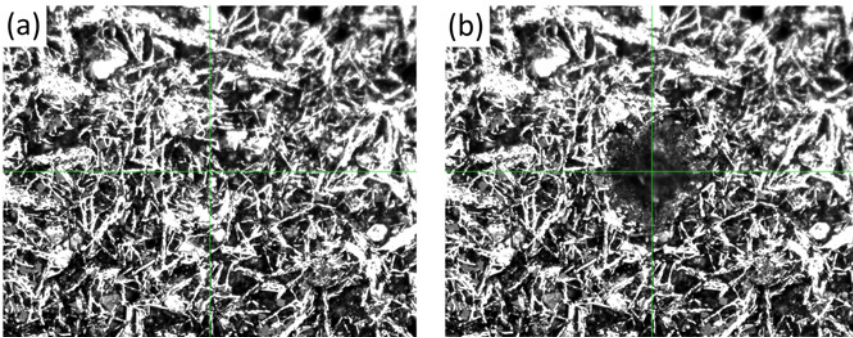
Figure 4.5: Surface texture of a Sishen particle (a) before test (b) after test (400×)

The applied load for hardness tests can be determined based on the surface pressure of bulk solids handling equipment [21]. Accordingly, a load of 9.8N is appropriate for the hardness tests in this research. The result of a Vickers hardness test of an iron ore particle surface is shown in Figure 4.5(b), which is observed

under 400 magnitude. Using the two diagonals (d_1 and d_2) of the indentation area and the applied load (F_p), a Vickers hardness number is calculated by Equation 4.1. To fully examine the hardness of varied surfaces, each surface of a particle is measured both at core area and outer area, and each area is measured eight times. Totally 320 hardness tests were carried out on the two groups of Sishen particles.

4.1.4   Results of Vickers hardness number

Figure 4.6 displays the 320 hardness numbers that were obtained from 320 tests. The same color of 16 data represents the tests on one particle surface at both core and outer areas. It was shown that the hardness number varies from 60 to 960 based on all obtained data. The large variance can be ascribed to the difference and inhomogeneity of inner structures for a single surface and for different particles.
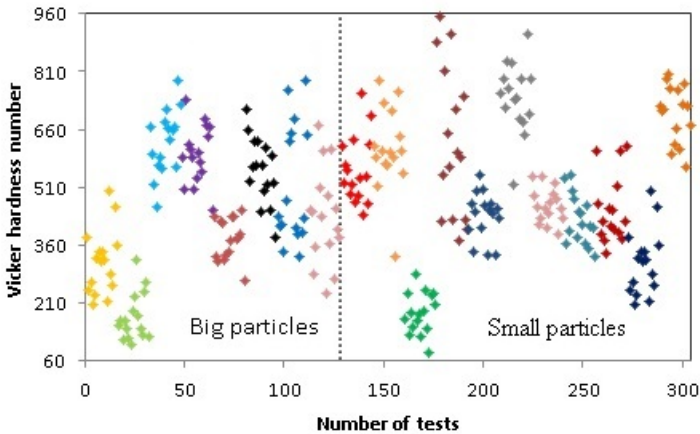
Figure 4.6: Results of 320 hardness tests from 20 Sishen particles
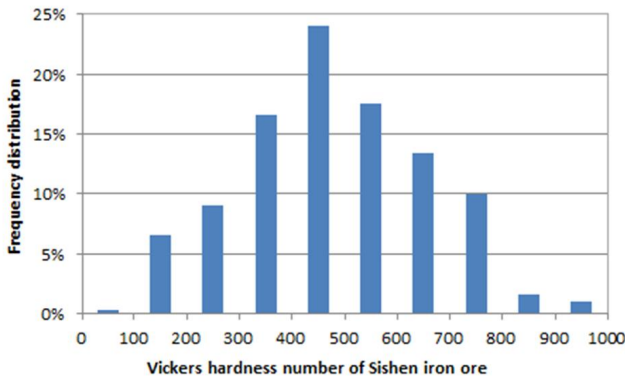
Figure 4.7: Frequency distribution of Vickers hardness number of Sishen iron ore

Using data presented in Figure 4.6, the frequency distribution of hardness numbers for Sishen particles is determined, which is shown in Figure 4.7. Using 95% confidence interval, the Vickers hardness number for Sishen is at $H_{v,p} = 476 \pm 19$. In the same way, the Vickers hardness number of mild steel is measured $H_{v,e} = 143 \pm 4$. It can be calculated that a high possibility of $H_{v,p}/H_{v,e} > 1.2$. This infers that Sishe particles can cause severe wear [37].

4.2   Pin-on-disk wear test

Besides that wear can be assessed using Vickers hardness test, it is also important to quantify sliding wear caused by particles. To apply Equation 2.3 to predict sliding wear volume (such as using DEM simulations), the coefficient of sliding wear α_s must be appropriately estimated. By using a pin-on-disk wear tribometer, the sliding wear volume can be measured and α_s can be calculated.

4.2.1   Experimental set up

Figure 4.8 shows a pin-on-disk tribometer for performing sliding wear tests. The infrared camera is used to capture the temperatures on the surfaces of tested samples. The standard method [69] is applied for conducting pin-on-disk wear tests. More explanations to this tribometer are given in chapter 2 (section 2.5.1).
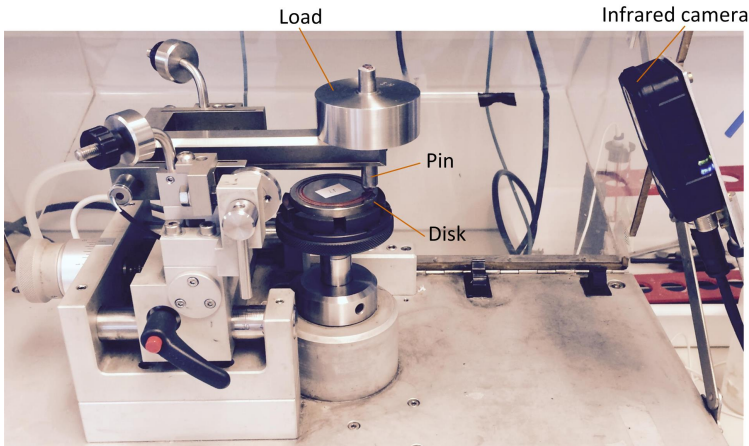
Figure 4.8: Pin-on-disk test apparatus

4.2.2   Experimental plan

Four parameters that affect sliding wear are to be tested:

(1) Particle shape, which affects contact properties [24, 120];

(2) Sliding distance, which has different wear rates for different wear states [45];

(3) Particle sliding speed, which can affect wear by affecting temperatures [121];

(4) Indentation force, which affects wear significantly.

Table 4.1 presents four series of tests to examine the effect of the four parameters on sliding wear. In test series I, in tests No. 1-8 and 25-26 eight natural particle tips and two spherical particle tips are used respectively. In test series II, each particle in tests No. 9-16 is used once and corresponds to one distance. In comparison, each particle in tests No. 27-28 is used for the whole range of distances. Test series III is used to investigate the influence of the sliding speed, in which similar shapes of particles are selected to minimize the contact differences. Test series IV is used to investigate wear subjected to different indentation forces, in which relatively similar particle tips are also used.

Table 4.1: Experimental plan for pin-on-disk wear tests

Test series	Test No.	Wear parameters	Variation	Base values
I	1-8 ; 25-26	particle shapes [–]	non-spherical, spherical	–
II	9-16 ; 27-28	sliding distance l_s [m]	9 –225	180
III	17-20	sliding speed v [m/s]	0.05 – 0.35	0.15
IV	21-24	normal force $F_n [N]$	1 – 10	5

For all the 28 tests, the distance between the pin and the central axis of disk $r_0 = 22$ mm. To understand sliding wear, the coefficient of sliding friction and the contact temperature are also measured. The accuracy of measured temperature is $\pm 0.1^oC$. To measure wear loss in mass, an electronic balance which has the accuracy of ± 0.5 mg is used. For obtaining wear volume by mass and density, a gas-expansion pycnometer is used to measure the density of Sishen particles.

4.2.3 Sample preparations

To perform a pin-on-disk wear test between a Sishen particle and a mild steel surface, each particle must be tightly attached to the end of a pin. Corresponding to the experimental plan, 28 pin samples were made, and are labeled No. 1-28 as shown in Figure 4.9. Among the 28 pins, No. 25-26 are ended with spherical particle tips that were fabricated by laser carving. Because a certain amount of water was used during the fabricating process, the oxidation of these two Sishen particles could be triggered.

Figure 4.10 shows the samples of mild steel disks, which are prepared using the same procedures as that for hardness test. The radii and thickness of all the disks are 26.5 mm and 6 mm, respectively. During the wear tests, each pin corresponds to a specific mild steel disk surface.

Figure 4.9: Experimental pins with SiShen particles
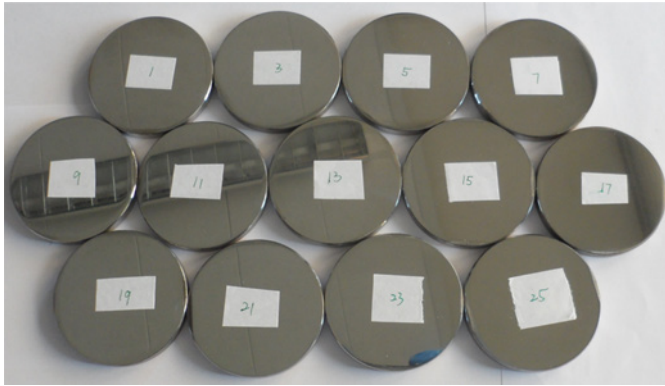
Figure 4.10: Samples of Prepared mild disks

4.2.4   Calculation of the coefficient of sliding wear

Due to the inhomogeneity of wear morphology of mild steel surface, large variations are triggered the calculation of wear volumes based on the measurements of wear profiles. Therefore, the wear loss in mass is measured using a laboratory electron balance (with the accuracy of $\pm\,0.5$ mg). Using a gas-expansion pycnometer, the average density of Sishen particles ρ_p is measured to be 4865 ± 72 kg/m^3 (using 95% confidence interval), which accounts for relatively big and relatively small particles. The density of the used mild steel ρ_p is measured at 7932 kg/m^3. Thus the wear volumes can be calculated for all tests using Equation 4.2,

$$W_V = \frac{\Delta m}{\rho} \tag{4.2}$$

where Δm is the mass loss by sliding wear and ρ is the density of worn material.

With the obtained wear volumes and Table 4.1, the coefficient of sliding wear for both particle and mild steel can be determined. Based on sliding wear Equation 2.3, the coefficient of sliding wear is derived in Equation 4.3:

$$\alpha_s = \frac{W_V}{F_n l_s} \tag{4.3}$$

4.2.5 Results and discussion

In this section, the results of the pin-on-disk tests are discussed. It is referred to Table 4.1 for the experimental plan. Moreover, this section also includes the characterizations of the sliding friction and temperature rise.

Wear subjected to particle shapes: Test series I

Figure 4.11 shows the morphologies of particles before tests (No. 1-8) and after the tests (No. 1'-8'). It is noted that the tips of particles are marked blue which is for efficiently visualizing 3D morphologies using a microscope. This figure demonstrates that certain particle tips have remarkable changes (i.e. No. 2-2', 6-6' and 7-7') while the others have minor changes. A suggested reason is that the unequal wear loss is mainly due to different particle hardness (Figure 4.7) and partially ascribed to the tip shapes [46].
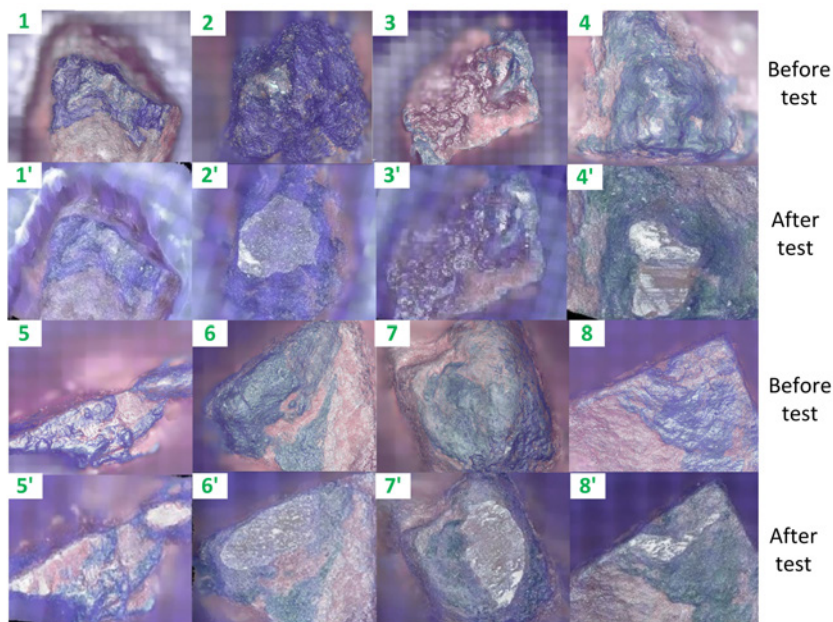
Figure 4.11: Pin particle tips before test (No. 1-8) and after test (No. 1'-8')

Figure 4.12 presents the morphologies for the two spherical particles (No. 25-26) before and after tests. The worn surface of No. 25 particle shows red oxides, which is different from the others. Based on the observation of a substantial mass loss of red color debris dropped from the spherical particle during the test, it is believed that this particle has more porous inner structure. This structure can be caused by oxidation because the water was added during fabricating process. Therefore, test

No. 25 is discarded in the future analysis. However, the surface of No. 26 particle after test (No. 26′) is similar to the others. From the comparison of the test result fo test 25 and 26, and tests 1-8 and 26, it can be concluded that No. 26 particle is not corroded due to the fabricating process.
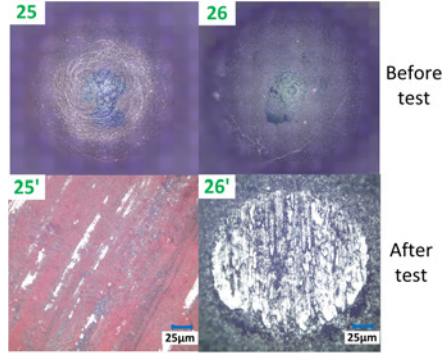
Figure 4.12: of spherical particle tips before (No. 25-26) and after test (No. 25′-26′)

Figure 4.13(a) shows an an example of the morphology of the wear path on a mild steel disk surface. During wear processes by a particle tip, grooves were formed as a result of the removal and transfer of the surface material of mild steel. The wear morphology is inhomogeneous due to the wear of the particle asperities. Figure 4.13(b) displays the three dimensional topography of the wear path and Figure 4.13(c) plots the wear profile for the measured cross-sectional area.
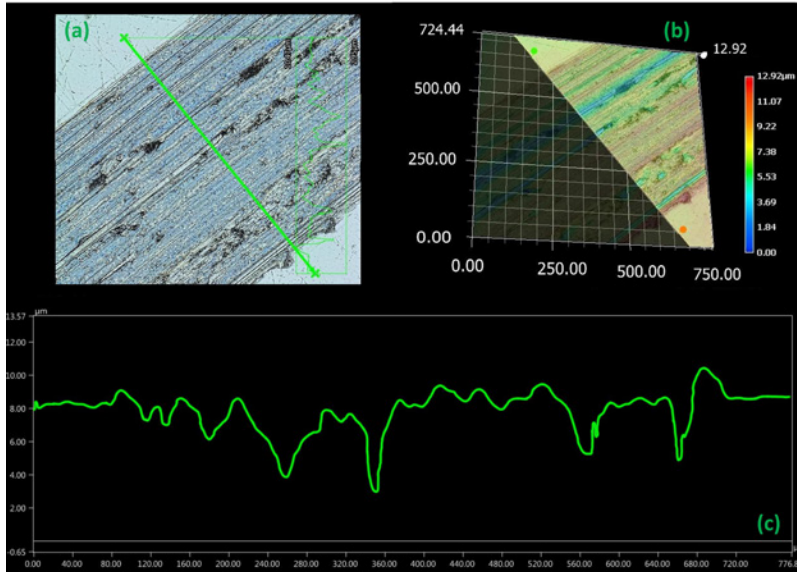
Figure 4.13: Wear morphology of a mild steel disk surface (a) an area of wear path; (b) 3D visualization; (c) profile of the measured cross-section area

Figures 4.14 and 4.15 present the calculated wear volumes of tests No. 1-8 and 26 for particle and mild steel disk, respectively. It shows that the volume loss of both particle and mild steel varies significantly. The suggested reason is also that is mainly ascribed to the difference in particle hardness [37] and partially to the variance in particle shapes. By comparison, the deviation for particles is larger, a suggested explanation is that different Sishen particles have different hardness and thus different wear loss [46].
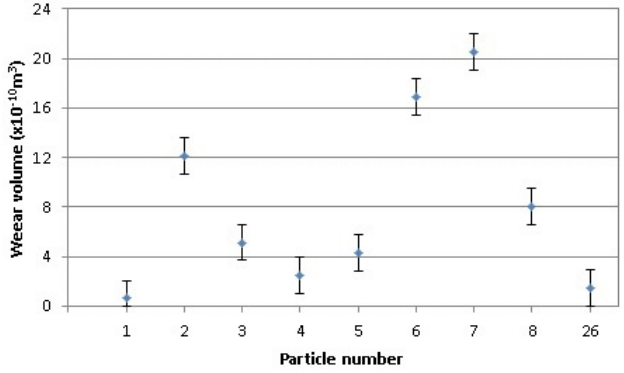
Figure 4.14: Wear of particles No. 1-8 and 26
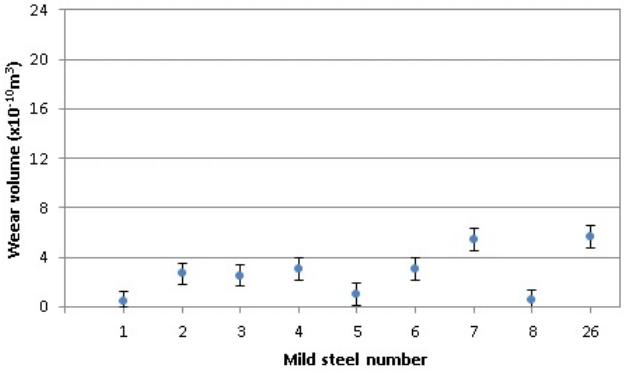
Figure 4.15: Wear of mild steel disks No. 1-8 and 26

To estimate the average coefficient of sliding wear subjected to both non-spherical and spherical particle tip, the wear volumes for particles No. 1-8 and No. 26 were used (Particle No. 25 was discarded as stated earlier). The average of wear volumes is calculated at $(7.95\pm0.49)\times10^{-10}\mathrm{m}^3$. Assuming that ductile failures occurred to Sishen iron ore particle with respect to the sliding test, and using the base values of sliding distance and indentation force in Table 4.1, the average coefficient of sliding wear for Sishen particles is calculated at $\alpha_{s,p}=(8.83\pm0.67)\times10^{-13}\mathrm{m}^2/\mathrm{N}$. In the same way, the average wear volume of mild steel disks in tests No. 1-8 and No. 26 is calculated at $(2.69\pm0.30)\times10^{-10}\mathrm{m}^3$. The average coefficient of sliding

wear for mild steel is calculated at $\alpha_{s,e}=(2.99\pm0.36)\times10^{-13}\mathrm{m}^2/\mathrm{N}$.

Wear subjected to sliding distances: Test series II

Figures 4.16 and 4.17 respectively present the wear volumes for the particles and mild steel disks used in tests No. 9-16. It can be seen that wear volumes do not always increase with respect to increasing sliding distance [45, 46]. Typically, the volume in test No. 14 is extraordinary high for the particle while quite low for the mild steel disk. By carrying out hardness test on the surface of used particle No. 14, it was shown that this particle has porous structure and a low hardness of this particle. Thus this particle can be easily worn whist the corresponding mild steel surface suffer less wear.
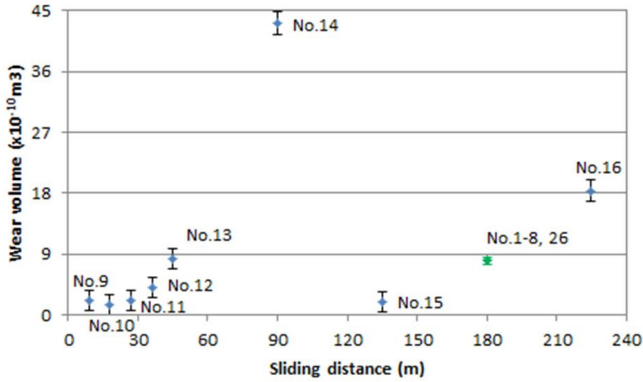
Figure 4.16: Wear of particles No. 9-16
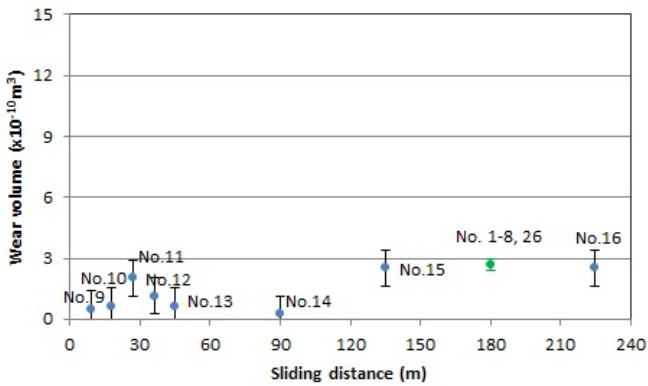
Figure 4.17: Wear of mild steel disks No. 9-16

To avoid the influences of the differences of hardness and shapes of particle tips on wear, two particles are individually tested with respect to the same set of distances in Table 4.1. Figures 4.18 and 4.19 shows the wear volumes for particles and mild steels respectively. It can be seen that for both particle and mild steel, the wear

loss increases continuously with increasing sliding distance. Figures 4.18 and 4.19 also demonstrate that the mean wear volumes for both particle and mild steel are higher than the average obtained fromc tests No. 1-8 and 26 at the distance 180 m. This is due to the fact that when measuring mass loss for the tests No. 27-28, the wear debris was cleansed, therefore particle tip can be fully in contact with mild steel for the subsequent tests and causes more wear.
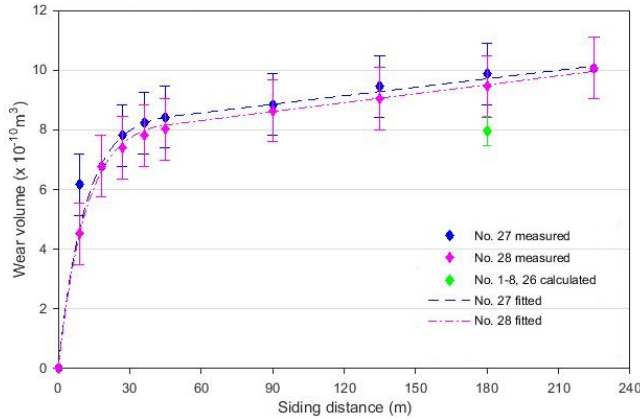
Figure 4.18: Wear as a function of sliding distance for particles No. 27-28
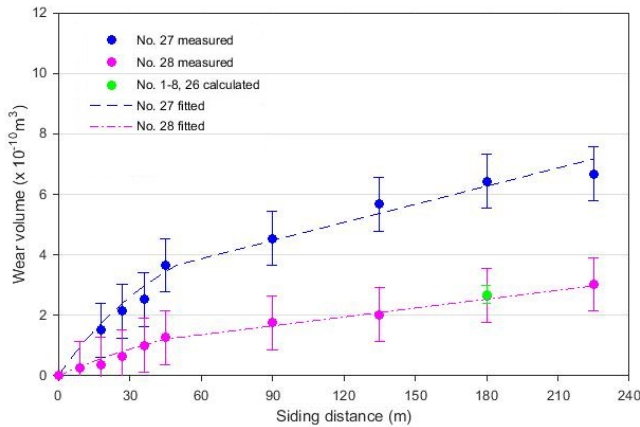
Figure 4.19: Wear as a function of sliding distance for mild steels No. 27-28

Figures 4.18 and 4.19 also indicate that for both particle and mild steel, the wear at transient state increases faster than the steady state. For the wear at transient state, the correlation between the wear volume and sliding distance can be formulated by Equation 2.1 [45],

$$W_{V,d,p,s,t} = A_0(1 - e^{-B_0 l_t}) \tag{2.1}$$

By using presented data for the transient-state in Figures 4.18 and 4.19 the constants A_0 and B_0 can be determined by curve fitting using MATLAB® [122]. In combination with the linear fit for the steady-state using Archard's Equation 2.3, the formulas to express the wear volumes of the particles used in tests No. 27-28 with respect a set of wear distances are given in Equations 4.4 and 4.5, and for No. 27-28 mild steel disks in Equations 4.6 and 4.7.

For the sliding wear of particles and mild steel disks, the following notations are used to represent wear volumes.

$W_{V,p,s}$: Wear Volume of iron ore Particle by Sliding test

$W_{V,m,s}$: Wear Volume of Mild steel by Sliding test

Particle No. 27,

$$W_{V,p,s} = \begin{cases} 8.58 \times (1 - e^{-0.088l_s}) \times 10^{-10}, & 0 \le l_s \le 50 \quad (4.4a) \\ (0.0095 \times l_s + 8.0) \times 10^{-10}, & 50 \le l_s \le 225 \quad (4.4b) \end{cases}$$

Particle No. 28,

$$W_{V,p,s} = \begin{cases} 8.35 \times (1 - e^{-0.086l_s}) \times 10^{-10}, & 0 \le l_s \le 45 \quad (4.5a) \\ (0.01 \times l_s + 7.71) \times 10^{-10}, & 45 \le l_s \le 225 \quad (4.5b) \end{cases}$$

Mild steel No. 27,

$$W_{V,m,s} = \begin{cases} 5.98 \times (1 - e^{-0.019l_s}) \times 10^{-10}, & 0 \le l_s \le 50 \quad (4.6a) \\ (0.02 \times l_s + 2.67) \times 10^{-10}, & 50 \le l_s \le 225 \quad (4.6b) \end{cases}$$

Mild steel No. 28,

$$W_{V,m,s} = \begin{cases} 2.73 \times (1 - e^{-0.013l_s}) \times 10^{-10}, & 0 \le l_s \le 45 \quad (4.7a) \\ (0.0098 \times l_s + 0.77) \times 10^{-10}, & 45 \le l_s \le 225 \quad (4.7b) \end{cases}$$

Wear subjected to sliding speeds: Test series III

Tests No. 17-20 are carried out to investigate the impact of sliding speed on wear volume. The Figures 4.20 and 4.21 respectively show the wear volumes of particle and mild steel with respect changing sliding speeds. It can be seen that No. 17 particle has a high volume while No. 20 has a low volume. However, according to Straffelini et al. [123], low sliding speeds may have minor effect on wear subjected to constant contact. The reason is believed to be the porous and uneven inner structure as well as the low hardness [37] based on hardness test . The wear volumes for mild steel disks do not differ significantly as expected [121].

Wear subjected to indentation forces: Test series IV

Tests No. 21-24 are carried out to investigate the effect of the indentation force on wear volume. Figure 4.22 and Figure 4.23 show the results of wear volumes as functions of sliding distance for particle and mild steel, respectively. The yellow areas are the wear volumes calculated by applying the average coefficients of

sliding wear $\alpha_{s,p}$=(8.83±0.67) $\times 10^{-13}$ m^2/N and $\alpha_{s,e}$=(2.99±0.36)$\times 10^{-13}$ m^2/N to Archard's Equation 2.3. By accounting for the variations, the experimental data are consistent with the predicted range of wear volumes.
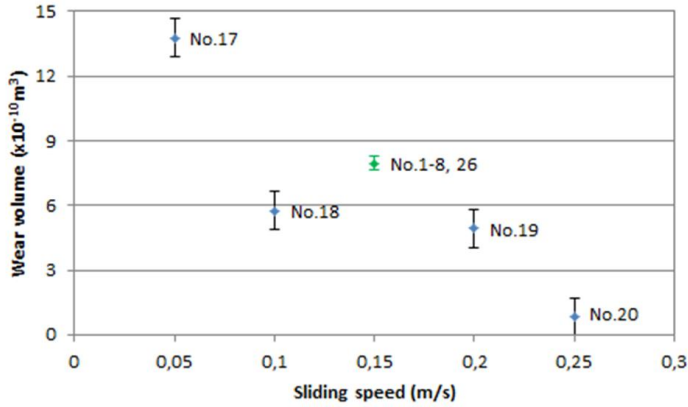
Figure 4.20: Wear volume of particle as a function of siding speed
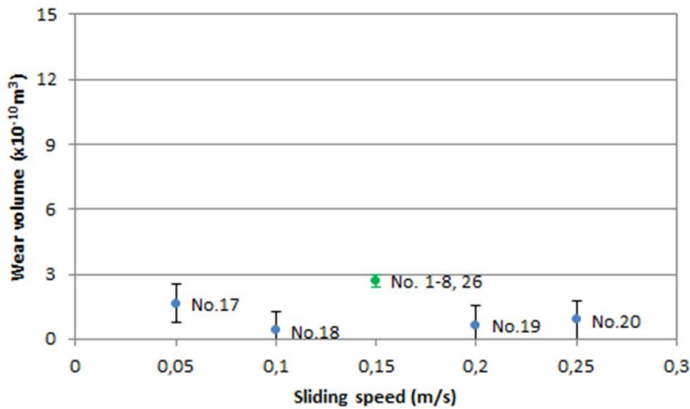
Figure 4.21: Wear volume of mild steel as a function of siding speed

Characterization of sliding friction

The coefficient of sliding friction is defined as the ratio of tangential force F_t to normal F_n, and is shown in Equation 4.8,

$$\mu_s = \frac{F_t}{F_n} \qquad (4.8)$$

Due to the variance of contact between particle and disk during a wearing process, the tangential force F_t changes and thus the coefficient of friction varies. When the coefficient of sliding friction is plotted as a function of distance, two types of friction curves can be distinguished.
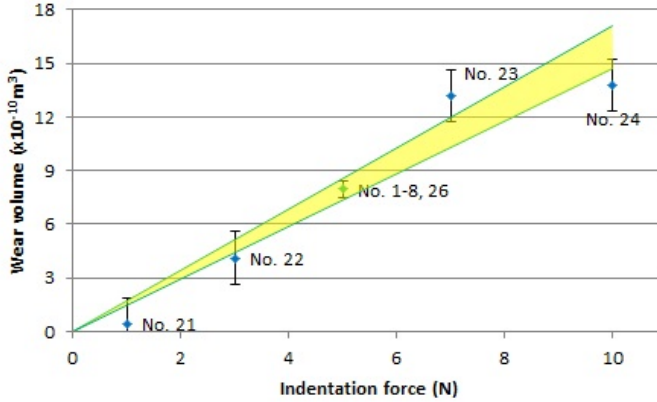
Figure 4.22: Wear volume of particle tip as a function of indentation force
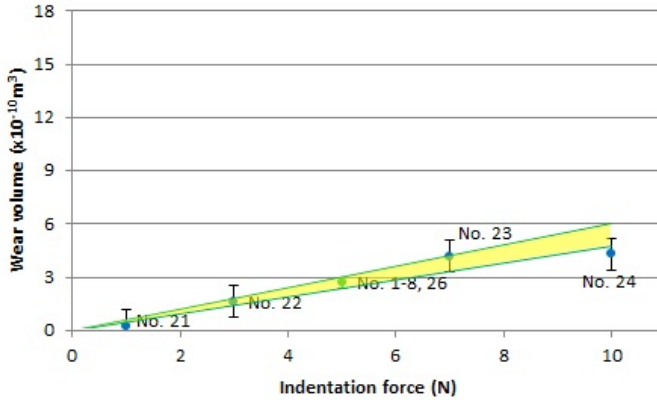
Figure 4.23: Wear volume of mild steel as a function of indentation force

Figure 4.24 shows the Type 1 characteristic, which is plotted using test No. 3. It shows that the coefficient of sliding friction initially maintains an increasing trend and arrives at the maximum value. Then it goes down by certain level and maintains a relatively stable value. The friction Type 2 is plotted in Figure 4.25 by using the result of test No. 7. It shows that for whole wear process the coefficient of friction maintains an increasing trend prior to reaching a relatively constant state. Moreover, it is noticed that for Type 2 the fluctuations at steady-state are severer. By comparing with the wear volumes for Type 2, it is concluded that more wear loss is triggered from for the severer fluctuations at steady-state.

Type 1 friction characteristic happens to majority tests, whereas Type 2 occurs to a few tests. Possible reason is that Type 1 is in correspondence to the hardness ratio $H_p/H_e > 1.2$ [37] which are the majority cases referring to Figure 4.6. On the contrary, Type 2 is for $H_p/H_e \leq 1.2$ [37] which are the minor cases (Figure 4.6).
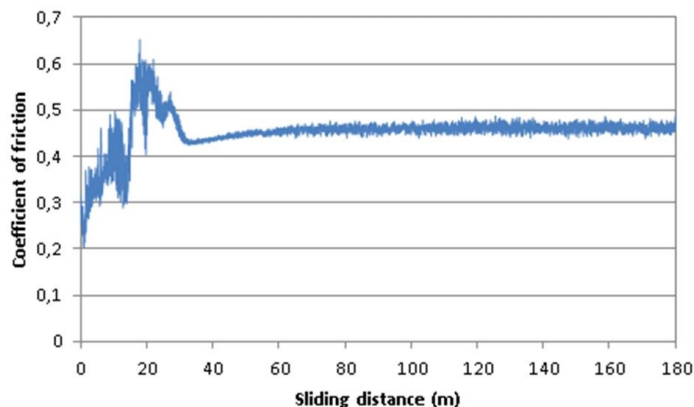
Figure 4.24: Type 1 frictional characteristic (test No. 7)
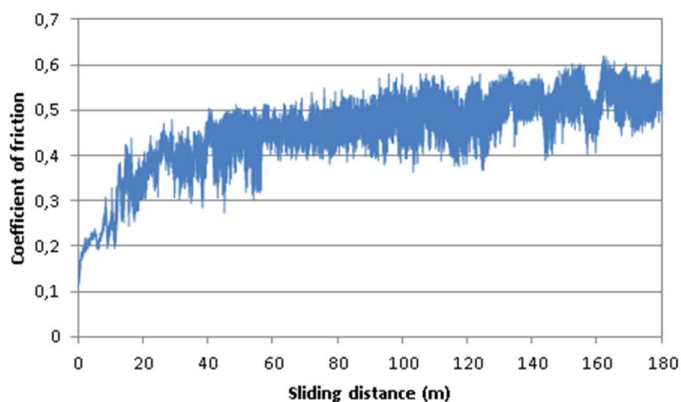
Figure 4.25: Type 2 frictional characteristic (test No. 3)

By comparing Figures 4.24 and 4.25 with wear volume loss in Figures 4.18 and 4.19, the friction characteristics are also consistent with wear states. By this, it is obtained that for all four series of 28 tests the maximum coefficient of sliding friction lies in 0.6-0.8 for transient state while in 0.2-0.6 for steady-state. In addition, it is obtained that the wear distance lies in 20 to 80 m with respect to transient state for all tests.

Characterization of temperature increase

Figure 4.26 shows an image of the thermal field during a pin-on-disk test. In this figure, points 1 and 2 are chosen in the proximity area of the contact between particle and mild steel disk. Others two points (3 and 4) and a square area are simply used as references. The thermal field shows that the surface of the particle suffers a higher temperature than that of mild steel disk.

An illustration of temperature increase is shown in Figure 4.27, which is plotted according to test No. 26. It can be seen that the contact temperature increases

during transient wear state and approximately maintains constant at steady state, which is also observed in the measurement in [124]. The reason for the variance of temperature rise is due to the change of sliding friction based on heat generation theory (Equation 4.9).

$$U_r = \frac{\mu_s F_n v_s}{A_n} \tag{4.9}$$

where U_r is the rate of heat generation, A_n is the contact area.

Furthermore, according to the experimental results, it is obtained that the temperature increase faster with respect to higher indentation forces or sliding speeds, which are as expected using the heat generation theory (Equation 4.9). In order to verify the measured contact temperature, the text No. 26 which utilizes a spherical particle tip, is selected to theoretically estimate the corresponding temperature increase, which is presented as follows.
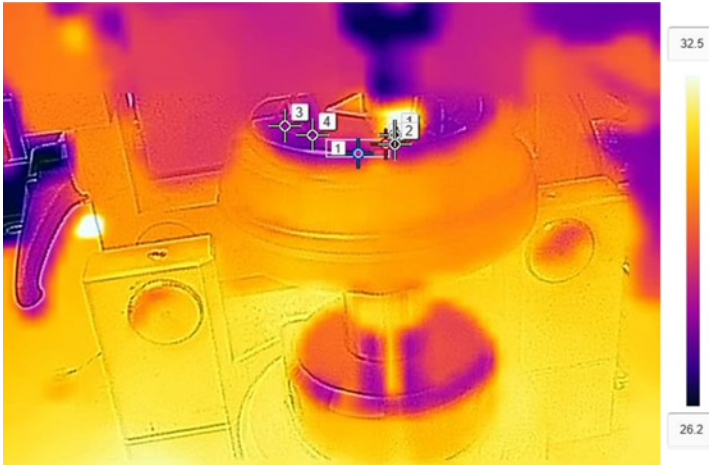
Figure 4.26: Thermal field and measurements of contact temperature

The increase of contact temperature T_c can be obtained using [125],

$$\frac{1}{T_c} = \frac{1}{T_p} + \frac{1}{T_d} \tag{4.10}$$

where T_p and T_d are respectively calculated temperatures by assuming that all heat flows in the particle or the disk.

Based on test No. 26, A_n is estimated by assuming that the contact is a circular area, which has a radius of a_1 [125], i.e,

$$A_n = \pi a_1{}^2 \tag{4.11}$$
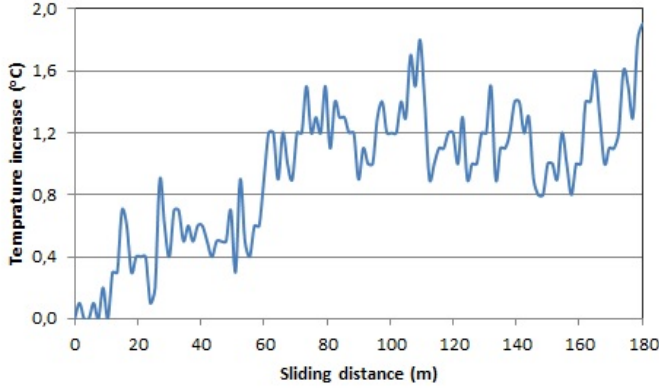
Figure 4.27: Temperature increase for particle in test No. 26

For the stationary particle tip, the average rise of contact temperature T_p is estimated by [125],

$$T_p = 0.5\Pi T_0 \tag{4.12}$$

where Π and T_0 are respectively given by Equations 4.13 and 4.14 [125],

$$\Pi = \frac{v_s a \rho h_s}{2k} \tag{4.13}$$

$$T_0 = \frac{\pi U_r}{\rho h_s v_s} \tag{4.14}$$

in which h_s is specific heat, k is thermal conductivity.

For the moving mild steel disk which has a relatively low speed, the average temperature rise is estimated by Equation 4.15 (a) or (b) depending on the dimensionless parameter Π [125],

$$T_d = \begin{cases} 0.5\Pi T_0 & for \ \Pi < 0.1 \tag{4.15a} \\ 0.5\xi(\Pi)\Pi T_0 & for \ 0.1 \leq \Pi \leq 5 \tag{4.15b} \end{cases}$$

where $\xi(\Pi)$ is presented in Table 4.2 [126].

Table 4.2: Value of $\xi(\Pi)$ corresponding to Π [126]

Π	0.1	0.2	0.5	1	2	5
$\xi(\Pi)$	0.85	0.83	0.75	0.66	0.57	0.44

Table 4.3 listed the parameter values for estimating temperature increase of iron ore and mild steel for the test No. 26.

Table 4.3: Parameter values for calculating temperature blue for test No. 26

	Material parameters			Contact parameters			
	density ρ	specific heat h_s	conductivity k	friction μ_s	force F_n	velocity v_s	radius a_1
Particle	4865	472 [127]	18 [127]	0.5	5	0.15	0.0004
Disk	7932	490 [127]	54 [127]				

Using Equations 4.13 and 4.14, it is obtained that Π=3.83 and T_0=7.49 °C respectively. With this, the temperature for particle No. 26 is $T_p = 13.02$ °C using Equation 4.12. In analogy, using Equation 4.13, it is obtained Π=2.16 for mild steel disk. Referring to Table 4.3 [126], $\xi(2.16) \approxeq 0.57$ using Table 4.2 [126]. Thus T_0 is calculated at 4.02 °C. Using Equation 4.15, the temperature rise for the mild steel disk is $T_d = 2.47$ °C Eventually, using Equation 4.10, it is obtained that T_c =2.11 °C.

In comparison with the highest point of contact temperature increase (1.9 °C) in Figure 4.27, the theoretical calculation is slightly higher. A suggested reason is that the heat is lost to the ambient air and to the wear debris [124]. Therefore it is confirmed that the contact temperatures are successfully measured. For all tests measured from beginning till steady state wear, the estimated values of contact temperature increase lies in 1.3 and 2.2°C. Under such range of temperature rise, the influence on wear is negligible [121, 128]

4.3   Inclining surface test

An inclining surface can be used to measure the coefficient of static friction. A literature survey reports that the coefficients of static friction of iron ore pellets were studied using a pin-on-disk device [129]. However, the friction between Sishen particles and steel have not yet been determined. Based on the two assumptions in bulk solids handling: namely, particles can be in a very loose status, and particles are in a highly compacted state [21], the coefficients of static friction are measured for the contact between discrete particles and a steel surface, and for the contact between bonded particles and a steel surface.

4.3.1   Static friction for discrete particles

Figure 4.28 shows the device used to measure static friction of discrete particles. This tester employs a motor to enable the inclination of the bottom surface with respect to an axis as pointed in Figure 4.28. The angle between the inclining surface and horizontal surface is denoted as inclination angle, and can be automatically measured with the accuracy of $\pm 0.05^o$.

To carry out a test, individual particles are randomly placed on the bottom of steel surface at a horizontal level. With a certain rate the inclination angle of the

steel plate is increased. Except few particles roll downwards as increasing incli-
nation angle, the majority particles simply slide at certain inclining level. The
corresponding maximum angle is used to determine the coefficient of static fric-
tion for the sliding motion of particles, and Equation 4.16 can be used to calculate
coefficient of static friction.

Figure 4.28: Measuring the coefficient of static friction of discrete particles

$$\mu_{st} = tan\theta_w \tag{4.16}$$

To obtain a reliable coefficient of static friction, ten groups of iron ore samples were
used, and each group was tested three times. Therefore total 30 tests proceeded.
Based on the 95% confidence interval, the measured wall friction angle for discrete
particles is: $\theta_{w,d} = 23.1\pm0.3^oC$. The variance is caused by the difference in shapes
and sizes of particles [130, 131]. Correspondingly, the coefficient of static friction
for discrete particles is $\mu_{st,d} = 0.43 \pm 0.01$ (Equation 4.16).

4.3.2 Static friction for bonded particles

Figure 4.29 shows the twelve groups of bonded particles. In each group, particles
are randomly glued together. Similar to the test for discrete particles, each group
of bonded particles is tested three times with regard to varied contact between
surfaces of particles and steel. A total number of 36 tests were executed. Based
on the 95% confidence interval, the average measured angle for boned particles is:
$\theta_{w,b} = 26.3\pm1.3^oC$, which gives the coefficient of static friction for boned particles
$\mu_{st,b} = 0.49 \pm 0.03$ (Equation 4.16).

By comparison, the static friction for highly compacted bulk solids is approxi-
mately 14% larger than that of loose state. The reason is that when particles are
bonded, multiple particle tips are in contact with surface, which produce more
resistance that that of a single particle tip.

Figure 4.29: Twelve groups of glued multiple particles

4.4   Conclusions

To answer the subquestion of *"What experiments can be used to determine the DEM parameters for modeling wear in bulk solids handling?"*, this chapter discusses three tests used to determine material and contact parameters for iron ore and mild steel. Conclusions are given as below:

(1) The hardness number of Sishen particle varied by measured locations and also by particles. Using a 95% confidence interval, the Vickers hardness number for Sishen particles is determined as: 476 ± 19.

(2) The average coefficients of sliding wear are determined for particle and mild steel are determined at $\alpha_{s,p} = (8.83 \pm 0.67) \times 10^{-13} \text{ m}^2/\text{N}$ and $\alpha_{s,e} = (2.99 \pm 0.36) \times 10^{-13} \text{ m}^2/\text{N}$ respectively. Furthermore, the sliding wear volumes for particle and mild steel are determined with respect to transient state and steady state.

(3) The coefficient of sliding friction is varied by particles and distances. In addition, two types of friction characteristics are distinguished: namely, friction increases to a peak value at transient state and friction maintains increasing trend at transient state.

(4) At an open test environment, the contact temperature rise for single particle sliding is between 1.3 and 2.2^{o}C. This range of temperature rise has no impact on the wear rate.

(5) The coefficients of static friction for discrete particles and bonded particles are $0.43 \pm 0.01s$ and 0.49 ± 0.03 respectively. It shows that the coefficient of static friction for discrete particles is approximately 14% lower than that of bonded particles.

The experimental tests provide crucial referential values determining DEM parameters for modeling mild steel wear by Sishen particles. Based on the obtained data from experimental tests, the next chapter presents the verifications of wear predictions by single particle.

5 | CHAPTER

Verification of wear prediction by the discrete element method

C hapter 4 presented experimental tests for measuring material and contact parameters for iron ore particles and a mild steel. Using theses parameters, the interaction between particle and equipment can be modeled. Therefore, the wear of equipment surface can be predicted by using DEM simulations. To assess the reliability of the simulation models, it is essential to firstly wear predictions based on the behavior of a single particle.

This chapter theoretically verifies the wear predictions using single particle wear models and is organized into four sections. Section 5.1 introduces the DEM simulations for wear prediction in bulk solids handling. Section 5.2* presents the verification of particle sliding wear. Section 5.3 provides the verification of particle impact wear. Finally, conclusions are given in section 5.4.

5.1 Discrete element method

The discrete (or distinct) element method (DEM) was initially developed by Cundall and Strack [133] to predict mechanics of rocks that were composed by spherical particles. Hence, DEM has been extensively used to model dynamic interactions of various granular matters. This section starts with elaborations on equilibrium equations of two contact particles. After that the applications of DEM for wear prediction are reviewed. Furthermore, the used Hertz-Mindlin no-slip contact model in this research is illustrated.

5.1.1   Equilibrium equations

Figure 5.1 shows two spherical particles that are in contact. The movements of particles abides Newton's second law of motion [133]. For each particle, a contact force and also a gravitational force are applied. The equilibrium equations for calculating translational and rotational motions (e.g. particle i) are given in Equations 5.1(a-b).
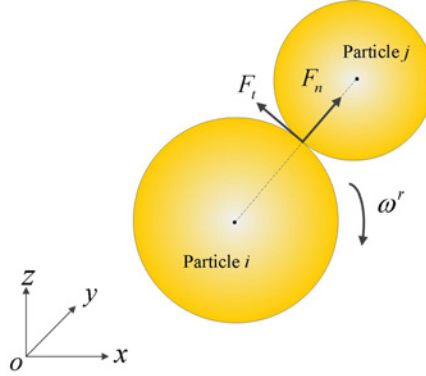
Figure 5.1: Contact between two spherical particles i and j [133]

$$\begin{cases} m_i \dfrac{d\boldsymbol{v}_i^r}{dt} = \boldsymbol{F}_c + m_i \boldsymbol{g} & (5.1a) \\[2mm] I_i \dfrac{d\boldsymbol{\omega}_i^r}{dt} = \boldsymbol{M}_{t,ij} + \boldsymbol{M}_{r,ij} & (5.1b) \end{cases}$$

In Equation 5.1a, m_i is the mass of particle i; $\boldsymbol{v}_i^r$ is the velocity of particle i relative to particle j; $\boldsymbol{g}$ is global gravity ($\boldsymbol{g} = [0, 0, -9.81]^{-1}$). $\boldsymbol{F}_c$ is the contact force between particles. $\boldsymbol{F}_c$ is composed of a normal force $\boldsymbol{F}_n$ and a tangential contact force $\boldsymbol{F}_t$ (Equation 5.2),

$$\boldsymbol{F}_c = \boldsymbol{F}_n + \boldsymbol{F}_t \qquad (5.2)$$

In Equation 5.1b, I_i is the moment of inertia of particle i. $\boldsymbol{M}_{r,ij}$ is the torque induced by particle rolling friction. $\boldsymbol{M}_{t,ij}$ is the torque induced by tangential force,

$$\boldsymbol{M}_{t,ij} = -\frac{\boldsymbol{\omega}_i^r}{|\boldsymbol{\omega}_i^r|} F_t r_i \qquad (5.3)$$

where $\boldsymbol{\omega}_i^r$ is the angular velocity of particle i relative to particle j; r_i is the radius of particle i.

Equations 5.1(a-b) are used to determine equilibriums of forces and torques subjected to particle-particle contact. These equations are also applicable for particle-geometry contact.

5.1.2   Review of wear prediction by DEM

A series of contact models are developed to simulate behaviors of bulk solids [134]. For non-cohesive materials, the Hertz-Mindlin no-slip contact model [116, 135, 136] and Linear-Spring-Dashpot (LSD) model [136, 137] are used. For cohesive materials, the Hertz-Mindlin Johnson-Kendall-Roberts (JKR) [138, 139] contact model can be applied.

In bulk solids handling, the Hertz-Mindlin no-slip contact model has been used to predict the abrasion and impact on the liner [135, 140], lifter [141–143] and screen mesh [144, 145]. Furthermore, this model is used to predict impact force on a transfer plate [136], transfer chute [146] and pipe wall [147]. The LSD model has been applied on predicting the impact forces on a transfer plate [136].

In the available research that uses DEM to predict wear, it was done by assuming that the wear prediction by single particle is correctly determined. However, several parameters that can affect wear must be investigated. For instance, Sato et al. [143] indicated that particle size (radius) might affect sliding wear. Furthermore, Powell et al. [116] suggested evaluation of the effects of mesh sizes on the wear predictions. Thus far, at single particle level, the sensitivity of DEM parameters on the wear prediction has not yet been published in detail by the research community.

In this project, the Sishen iron ore sample has a moisture content that is less than 3.0% [23, 148]. The internal friction angle of the Sishen iron ore is measured at around 45°, which indicates this bulk sample is not very cohesive. Therefore, the Hertz-Mindlin no-slip contact model is chosen to model interactions of Sishen particles.

5.1.3   Hertz-Mindlin no-slip contact model

Figure 5.2 illustrates the Hertz-Mindlin (no-slip) contact model [149]. This model consists of two springs, two dampers and a slider. The springs are used to represent the particle stiffness in normal and tangential directions. Two dampers are used to model the damping forces and the slider is applied to generate a friction force. The normal force F_n is calculated according to Equation 5.4,

$$F_n = -\frac{2}{3}S_n\delta_n^{1/2} + D_n v_n \tag{5.4}$$

where S_n, δ_n , D_n and v_n are the overlap, coefficient of damping force and velocity in the normal direction of the contact.

The tangential force is also calculated based on the overlap and damping force in the tangential direction. However, the tangential force is restrained by Coulomb law [150]. The tangential force is expressed by Equation 5.5.

$$F_t = \min\{-S_t\delta_t + D_t v_t, \mu_{st}F_n\} \tag{5.5}$$

in which μ_{st} is the coefficient of static friction; S_t, δ_t, D_t and v_t are the stiffness, overlap, coefficient of damping force and velocity in the tangential direction of the contact. Expressions for the coefficients of spring stiffness and damping in normal and tangential direction are given in Table 5.1. Besides, the used equivalents are presented in Table 5.2.
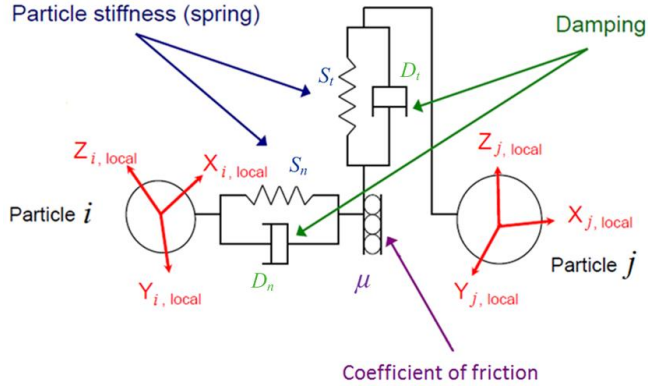
Figure 5.2: Parameters for Hertz-Mindlin no-slip contact model [149]

Table 5.1: Coefficients of spring stiffness and damping in normal and tangential directions [135, 151]

Coefficients	Normal direction	Tangential direction
Spring stiffness	$S_n = 2E^*\sqrt{r^*\delta_n}$	$S_t = 8G^*\sqrt{r^*\delta_n}$
Damping	$D_n = -2\sqrt{\frac{5}{6}}\frac{\ln e}{\sqrt{\ln^2 e + \pi^2}}\sqrt{S_n m^*}$	$D_t = -2\sqrt{\frac{5}{6}}\frac{\ln e}{\sqrt{\ln^2 e + \pi^2}}\sqrt{S_t m^*}$

Table 5.2: Equivalents for the contact model [135, 151]

Equivalents	$\frac{1}{E^*} = \frac{1-\nu_p}{2G_p} + \frac{1-\nu_g}{2G_g}$	$\frac{1}{G^*} = \frac{2-\nu_p}{G_p} + \frac{2-\nu_g}{G_g}$
	$\frac{1}{r^*} = \frac{1}{r_p} + \frac{1}{r_g}$	$\frac{1}{m^*} = \frac{1}{m_p} + \frac{1}{m_g}$

In bulk solids handling processes, abrasive wear is mainly caused by particle sliding. The erosive wear is caused by the succeeding impacts of individual particles. Therefore, wear models of particle sliding and particle impact will be respectively investigated in the following two sections.

5.2   Particle sliding wear

To model sliding wear by a single particle, the laboratory pin-on-disk test (chapter 4) is simulated by using DEM. To quantify sliding wear, Archard's model (Equation 2.2) is implemented. The accuracy of the predicted wear volume is assessed

by comparing DEM outputs with theoretical calculations based on the average measured parameters. The stability of simulation model is evaluated by repetitive tests of a reference case. In addition, the sensitivities of DEM parameters on the wear prediction are investigated.

5.2.1 Simulation model

Figure 5.3 shows the simulation model of a pin-on-disk wear test, which is modeled using the software EDEM$^\circledR$ 2.7.1 [149]. Here ω is the angular velocity of the disc geometry with respect to its central axis (OO') and F_p is the indentation force acting on the pin particle. A single mono-size spherical particle [152] is used to represent Sishen iron ore. As that in experiments, this particle is positioned at a distance r_0 =0.022 m with regard to the central axis (OO') and thus a full revolution of the disk covers a sliding distance 0.1382 m.
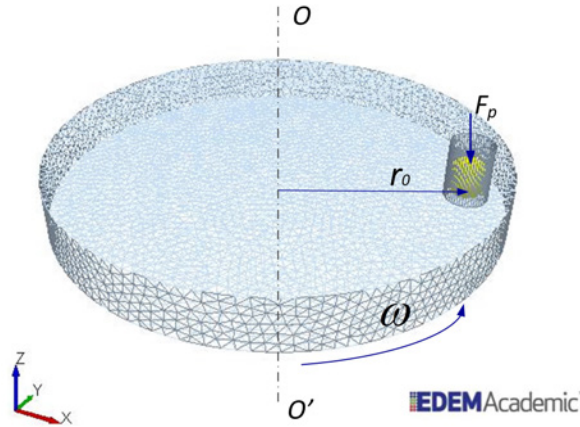
Figure 5.3: Simulation model for pin-on-disk wear test

To restrain the particle movements incurred by the rotating disk as in practice, a standard cylindrical geometry (holder) is applied and the rolling motion of the particle is disabled. The holder is vertically positioned and is parallel to the center axis of the disc. To place a particle into the holder, the radius of holder has to be slightly larger than the radius of the modeled particle. In this research, all the radii of holders are 0.1 mm larger than the inside particles.

Figure 5.4 illustrates the DEM simulation cycle of modeling a pin-on-disk wear test. It implies that, as geometry rotates, the simulation model subsequently undergoes four procedures in each time step until the simulation time has been reached. These four procedures are: apply indentation force, detect contact, calculate wear and update contact. The indentation force on the particle is applied by the particle body force by using EDEM$^\circledR$ API [149] and the global gravitational force. The Hertz-Mindlin no-slip contact model [116, 129] is used to calculate the

contact forces between particle and geometry. In the DEM simulations, a geometry surface is constructed with meshes which interact with particles. To quantify the wear volume, Equation 5.7 is derived, which is presented below.
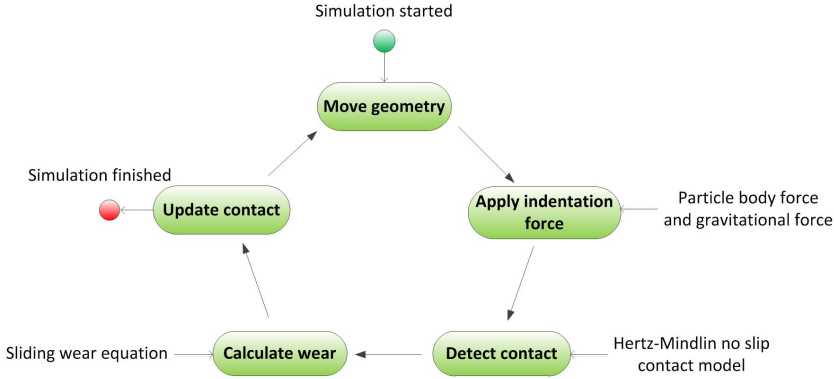
Figure 5.4: Simulation cycle of a pin-on-disk wear test based on [153]

Using the sliding wear Equation 2.3 and the normal force Equation 5.4, the sliding wear from a meshed geometry surface for a distance Δl is given by Equation 5.6.

$$\Delta W_V = \alpha_{s,e} F_n \Delta l = \alpha_{s,e} F_n v_t \Delta t = \alpha_{s,e}(-\frac{2}{3}S_n \delta_n^{1/2} + D_n v_n)\omega r_0 \Delta t \qquad (5.6)$$

The total wear W_V in the DEM simulations for a sliding distance l is a sum of wear from all contact meshes, as shown in Equation 5.7.

$$W_V = \sum \Delta W_V = \alpha_{s,e} \sum (-\frac{2}{3}S_n \delta_n^{1/2} + D_n v_n)\omega r_0 \Delta t \qquad (5.7)$$

Thus far, the sliding wear equation and the simulation cycle have been illustrated for modeling a pin-on-disk wear test. By inputing appropriate values of the parameters to the simulation model, the sliding wear of mild steel caused by Sishen particles can be predicted. Accordingly, the determination of the DEM parameters will be presented.

5.2.2   Determination of DEM parameters

This section illustrates the determinations of DEM parameters to predict sliding wear by using the simulation model of pin-on-disk wear test. All the DEM parameters are classified into four categories, namely, particle, geometry, contact and simulation. In this research, the values of the DEM parameters are determined on the basis of available resources and laboratory wear tests.

Based on the sliding wear Equation 5.7, four particle parameters are used as inputs in DEM simulations, which are:

(1) radius r_p;

(2) density ρ_p;

(3) Poisson's ratio ν_p;

(4) shear modulus G_p;

The determination of these four particle parameters is shown as follows:

Referring to the particle size distribution of the Sishen iron ore (Figure 2.1) and its median size d_{50} = 3mm [23], the modeled spherical particles radii are 1-4 mm to account for the sizes for majority particles. Using a gas-expansion pycnometer, the particle densities are measured, which varies from 4768 to 4970 kg/m^3 from small to large sizes. The average density is 4865 kg/m^3.

Because Sishen iron ore contains a large percentage of hematite which has Poisson's ratio 0.24 [154] [155], thus Poisson's ratio for Sishen particles is determined at 0.24. In combination with the variances of particle densities and inner microstructures, eventually, the Poisson's ratio of Sishen iron ore is estimated in the range of 0.23-0.26.

The shear modulus of Sishen particles is determined according to Equation 5.8 [156]:

$$G = \frac{E}{2(1 + \nu)} \tag{5.8}$$

in which the Young's modulus of Sishen particles E is given by an empirical Equation [154],

$$E_p = 55.27 + 128.87(\rho_p/1000 - 4.0) \tag{5.9}$$

Using equations 5.9 and the measured Sishen particle densities ρ_p = (4768-4970) kg/m^3, the Young's modulus of iron ore particle is calculated at (154.24-180.27) GPa. By applying the calculated values of the Young's modulus and the average Poisson's ratio of particle (i.e. 0.24) to Equation 5.8, the shear modulus is determined at (62.19-72.69) GPa.

Table 5.3 summaries the determined values for the particle parameters.

Table 5.3: Values for particle parameters

	DEM parameters	Values
	radius r_p [$\times 10^{-3}$]m	$1 - 4$
Particle	density ρ_p[kg/m^3]	$4768 - 4970$
	Poisson's ratio ν_p [–]	$0.23 - 0.26$
	shear modulus G_p [GPa]	$62.19 - 72.69$

Based on the geometry parameters in Equation 5.7, while also accounting for geometry mesh size, the following five geometrical parameters of the mild steel disk must be determined:

(1) density ρ_p;

(2) Poisson's ratio ν_p;

(3) shear modulus G_p;

(4) rotating speed ω_g;

(5) mesh size d_g;

The determinations of these five geometry parameters are presented as belows:

The density of the used mild steel plates was measured as 7932kg/m^3. The Poisson ratio and the shear modulus of mild steel are given in available research [157], which are 0.30 and 78 GPa, respectively. For maintaining consistency with our laboratory pin-on-disk wear test, the rotating speeds of the geometry set as (130.1-911.6) ^{o}/s, resulting in sliding velocity 0.05-0.35m/s. A higher velocity causes unstable contact due to vibrations of the system. The geometry is meshed into tetrahedrons using the software ANSYS® [158]. To achieve a smooth transition between the triangular meshes, the maximum size of mesh sides is set by 4.4×10^{-3} m. By accounting for the reduction of computational time which proportionally relates to number of meshes, the minimal mesh size is set by 0.55×10^{-3} m.

Table 5.4 presents the determined values for the disk geometry parameters.

Table 5.4: Values for disk parameters

	DEM parameters	Values
	density ρ_g[kg/m^3]	7932
	Poisson's ratio ν_g [–]	0.30
Disk	shear modulus G_p [GPa]	78
	rotating speed ω_g [$^o/s$]	$130.1 - 911.6$
	mesh size d_g [$\times 10^{-3}$] m	$0.55 - 4.4$

The geometry parameters of a cylindrical holder has no influence on steady-state wear. Therefore, a standard cylindrical geometry in the software EDEM® 2.7.1 [134] is used to generate a holder. Meanwhile, the default values for the geometrical parameters are applied.

Table 5.5 presents the determined values for the holder geometry parameters.

Table 5.5: Values for holder geometry parameters

	DEM parameters	Values
	density ρ_g[kg/m^3]	2500
Holder	Poisson's ratio ν_g [–]	0.25
	shear modulus G_p [GPa]	0.1

For the contact parameters between particle and geometry, three parameters must be determined, which are:

(1) coefficient of restitution e;

(2) coefficient of static friction μ_{st};

(3) coefficient of rolling friction μ_r;

The values of these three parameters are determined in the following manner:

First, the applied coefficient of restitution is to 0.42 by referring to experimental tests of iron ore pellets [129]. By accounting for the variety of the shape and densities of Sishen iron ore particles, a range of 0.35-0.50 is applied to the coefficient of restitution. According to Equation 5.7, the wear volume is not related to the coefficient of friction, therefore the value of 1.0 is applied. By applying this value, it is beneficial to minimize particle sliding movement before reaching a steady-state wear. Even though the particle is not allowed to roll, the coefficient of rolling friction is given by zero according to [157].

Table 5.6 provides the determined values for the contact between particle and disc geometry.

Table 5.6: Values for particle/disk contact parameters

	DEM parameters	Values
	coefficient of restitution e [–]	$0.35 - 0.50$
Particle/Disk	coefficient of static friction μ_{st} [–]	1.0
	coefficient of rolling friction μ_r [–]	0

For the interaction between particle and holder, the value of coefficient of restitution is significantly low so that the response of the particle during contact with the holder is largely damped. The other inputs of coefficients of static friction and rolling friction are identical to those of particle/disc contact. Table 5.7 gives the values for the contact between particle and holder.

Table 5.7: Values for particle/holder contact parameters

	DEM parameters	Values
	coefficient of restitution e [–]	0.0001
Particle/Holder	coefficient of static friction μ_{st} [–]	1.0
	coefficient of rolling friction μ_r [–]	0

Equation 5.7 gives three simulation parameters, which are indentation force, coefficient of sliding wear and sliding distance. Besides the three parameters, the applied time step must be determined. All four simulation parameters are presented as below.

(1) indentation force F_p;

(2) coefficient of sliding wear $\alpha_{s,e}$;

(3) sliding distance l_s;

(4) time step Δt;

The determination of the values for these four parameters is given below.

Referring to the force setting of laboratory test, a range of $3-9$N indentation are applied on particle. Under this range, the corresponding contact pressure is comparable to that of bulk solids handling [21].

To determine the coefficient of sliding wear $\alpha_{s,e}$, the indentation characteristic for a sphere indenting a ductile flat surface is illustrated in Figure 5.5. In this figure, δ_n is the normal overlap; A_1 is cross-sectional chord area under a sphere indentation. a_1 is the radius of the contact area [159]. The coefficient of $\alpha_{s,e}$ is expressed by Equation 5.10 and its derivation is given in Appendix A.
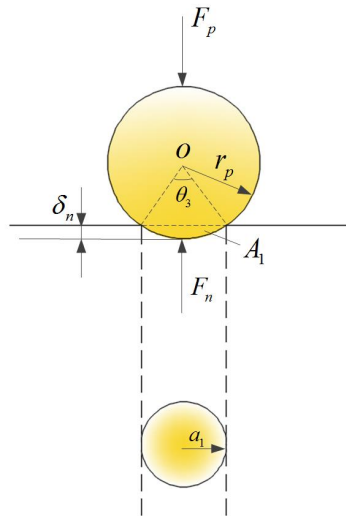
Figure 5.5: A rigid particle indents against an elastic surface [160]

$$\alpha_{s,e} = \frac{3\phi_4[arc\sin\left(\frac{\delta_n}{r_p}\right)^{1/2} - \left(\frac{\delta_n}{r_p}\right)^{1/2} + \left(\frac{\delta_n}{r_p}\right)^{3/2}]}{4E^*\left(\frac{\delta_n}{r_p}\right)^{3/2}} \tag{5.10}$$

In Equation 5.10, the coefficient ϕ_4 is the ratio of area loss relative to the full cross-sectional area under spherical indentation. The term $\frac{\delta_n}{r_p}$ is suggested as a constant for a given applied load regardless of particle sizes [47]. This is based on the fact that the applied load might be expected to be inversely proportional to the square of particle radius $r_p{}^2$, and to be proportional to the square of indentation depth $\delta_n{}^2$ [47].

To estimate $\frac{\delta_n}{r_p}$, Equation 5.11 is introduced [160],

$$H_e \approx 3Y_e \tag{5.11}$$

in which H_e is hardness of a metal surface and Y_e is the elastic load limit. For a spherical particle indent against ductile surface , Y_e can be equated to the maximum indentation pressure P_m, i.e. [35],

$$Y_e = P_m \tag{5.12}$$

where P_m is given by [160],

$$P_m = \frac{2}{\pi} E^* (\frac{\delta_n}{r_p})^{1/2} \tag{5.13}$$

Based on Equations 5.11 – 5.13, it is obtained,

$$\frac{\delta_n}{r_p} = (\frac{\pi H_e}{6E^*})^2 \tag{5.14}$$

The hardness of mild steel is experimentally measured at H_e=1.38 GPa. The equivalent Young′s modulus is calculated at E^* =96.74 GPa based on equations in Table 5.2. Using these values Equation 5.14 leads to $\frac{\delta_n}{r_p} = 5.58 \times 10^{-5}$.

To estimate the coefficient of fraction ϕ_4, it is assumed that A_2 is the real wear loss from the area of the displaced groove A_1, then the fraction ϕ_4 is expressed by,

$$\phi_4 = \frac{A_2}{A_1} \tag{5.15}$$

A_2 can be measured from a wear profile using a pin-on-disk test. However, it is difficult to accurately measure A_2 with respect to a single revolution. Therefore, a number of revolutions N_r are made to obtain a total loss A_3 from the displaced groove. Thus the real area loss A_2 for one revolution can be estimated by,

$$A_3 = \frac{A_2}{N_r} \tag{5.16}$$

To determine A_3, the pin-on-disk wear test for a spherical tip of iron ore particle is illustrated in Figure 5.6. Figure 5.6(a) presents the fabricated spherical tip of a Sishen particle. Figure 5.6(b) illustrates the approach to measure the area of cross-section. Figure 5.6(c) displays the three wear contours from three measurements. A_3 is obtained as the net area of the worn surface.

In the pin-on-disk test of using the spherical head of Sishen iron ore particle r_p= 3 mm, revolutions N_r=1302.5 which corresponding to l=180 m, the mean value of the net area A_3 from the three wear contours is 4.13×10^{-9}m^2. Using Equation 5.16, the average loss per revolution A_2=3.16×10^{-12} m^2. In combination with A_0 = 3.74×10^{-12}m^2 calculated by using Equation A.8, the coefficient of fraction is calculated as ϕ_4=0.84. E^* is estimated at 96.74 GPa. Eventually, Equation 5.10 gives $\alpha_{s,e} = 6.51\times10^{-12}$m^2/N.
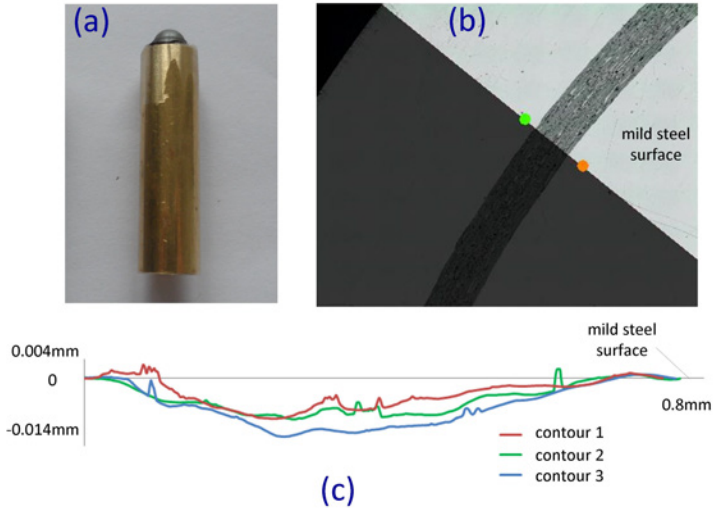
Figure 5.6: Determination of the coefficient of fraction (a) a pin with a spherical head of iron ore particle; (b) measuring an area of cross-section; (c) three wear contours based on three measurements

The sliding distance is set to 180 m (corresponding to 20 mins of testing), which refers to our laboratory pin-on-disk tests. The simulation parameter of time step is estimated using the Rayleigh time step, that is [161]:

$$t_R = \pi r_p \sqrt{\rho_p/G_p}/(0.1631\nu_p + 0.8766) \tag{5.17}$$

In DEM simulations, a lower value than Rayleigh time step is commonly used for increasing the accuracy of the simulation results. However, in attempting to reduce computational time and maintain simulation accuracy, the test range of values for time step $\Delta t = (50–130)\% \, t_R$, which corresponds to $1.0–2.5 \times 10^{-6}$s.

Table 5.8 lists the determined values for the simulation parameters.

Table 5.8: Values for simulation parameters

	DEM parameters	Values
Simulation	indentation force F_p [N]	$3-9$
	coefficient of sliding wear $\alpha_{s,e}$ [$\times 10^{-12}$m^2/N]	6.51
	sliding distance l_s [m]	138.2
	time step Δt [$\times 10^{-6}$s]	$1.0-2.5$

To sum up, values of the DEM parameters have been determined on the basis of analytical and experimental results. Using these values, the realistic prediction of wear by DEM can be obtained, which is presented as below.

5.2.3 Reference case of sliding wear prediction

Using Tables 5.3 – 5.8, a group of values used as a reference case is selected, which is given in Table 5.9. In correspondence to Table 5.9, Figure 5.7 presents the wear prediction, in which the legend bar represents the magnitude of the wear volume from each mesh. Due to the nonuniform meshes, the wear volumes from each worn mesh are not the same.

Table 5.9: Reference case of parameter values for pin-on-disk wear test

Categories	Wear aspects	DEM parameters	Values
Particle	iron ore	radius r_p [$\times 10^{-3}$m] density ρ_p[kg/m^3] Poisson's ratio ν_p [–] shear modulus G_p [GPa]	2 4850 0.24 65
Geometry	disk	density ρ_g[kg/m^3] Poisson's ratio ν_g [–] shear modulus G_p [GPa] rotating speed $_g$ [^{o}/s] mesh size d_g [$\times 10^{-3}$m]	7932 0.3 78 390.8 1.1
	holder	density ρ_g[kg/m^3] Poisson's ratio ν_g [–] shear modulus G_p [GPa]	2500 0.25 0.1
Contact	iron ore/disk	coefficient of restitution e [–] coefficient of static friction μ_{st} [–] coefficient of rolling friction μ_r [–]	0.4 1.0 0
	iron ore/holder	coefficient of restitution e [–] coefficient of static friction μ_{st} [–] coefficient of rolling friction μ_r [–]	0.00001 1.0 0
Simulation	conditions	indentation force F_p [N] coefficient of sliding wear $\alpha_{s,e}$ [$\times 10^{-12}$ m^2/N] sliding distance l [m] time step Δt [$\times 10^{-6}$ s]	5 6.51 180 1.5

To verify the accuracy of the predicted wear volume, Figure 5.8 presents the result of the reaction force in accordance with each time step for the early wear stage. This figure shows that the reaction force (F_n) initially increases to maximum, then it decreases with fluctuations and after 0.00001 s arrives at an expected constant. These overshoots are caused by the variance of overlap when applying the external force, i.e. particle body force [153]. The predicted forces are consistent with the calculation using Equation 5.4. Moreover, it is seen that the reaction force reaches a steady value in a very short period.

Figure 5.9 presents the particle tangential velocity corresponding to the early wear stage between 0 - 0.0012 s. Initially, the tangential velocity exhibits the same characteristics as that of the reaction force until it reaches constant speed. However, it begins to decrease when the particle comes in contact with the geometry of the holder. From the moment 0.0012 s on, the particle tangential velocity gradually reduces to zero, which means that the movement of the particle has been restrained by the holder.

It is expected that the particle tangential velocity maintains a constant of zero after 0.0012 s. However, the particle tangential velocity overshoots intermittently and triggers occurrences of numerical errors, as presented in Figure 5.10.
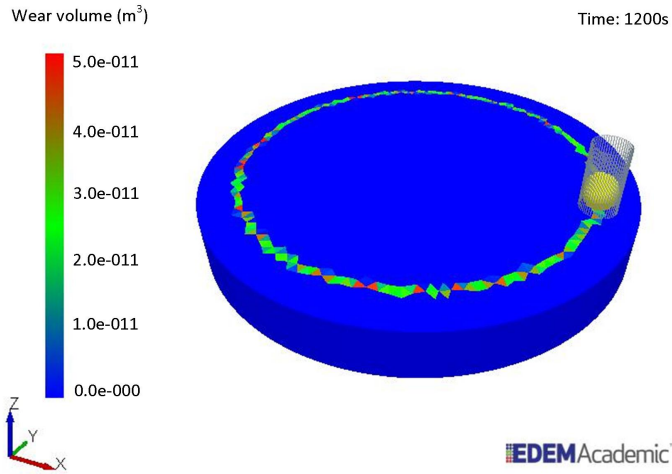
Figure 5.7: Wear for a sliding distance of 1200s (180m) of the reference case
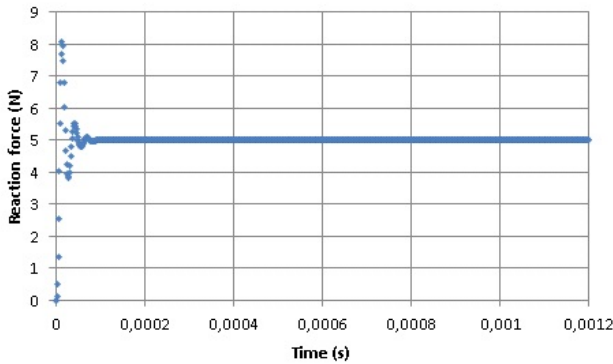
Figure 5.8: Reaction force as at an early wear stage

To further analyze the numerical scattered data, the first occurrence in Figure 5.9 is illustrated in Figure 5.11. It shows that particle tangential velocity drops to a negative value but immediately changes to positive. Then it continues to increase until reaching a peak. After that, the velocity begins to decreases and adjust to originally value (zero). By comparing the sudden increase with the wear track in Figure 5.7, it is concluded that a numerical error occurs whilst the particle crosses a joint side of the geometry meshes.

In order to examine the influence of the scattered data on total wear, the wear volume corresponding to the early stage 0.0312 s is illustrated in Figure 5.12. Referring to Figure 5.10, it demonstrates that the total wear can maintain a linear

increase even when numerical scattered data occur. This indicates that the influence of the numerical scattered data is negligible in comparison to the total wear, especially when considering that sliding distance is in the range of meters. Furthermore, the linear increase of wear volume indicates that steady-state wear starts after the particle is in full contact with the holder.
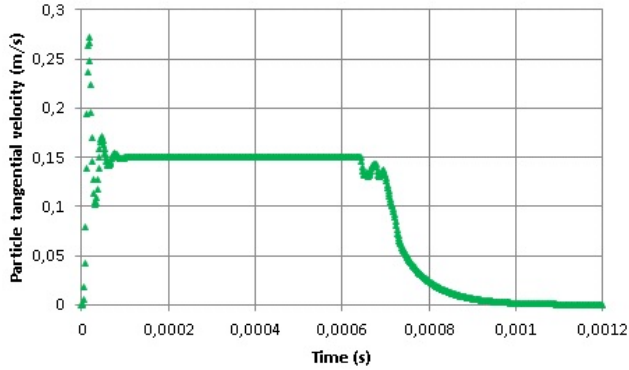
Figure 5.9: Particle tangential velocity at an early wear stage
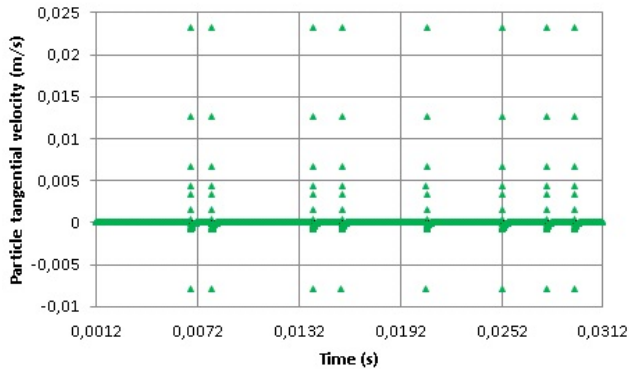
Figure 5.10: Particle tangential velocity after coming into contact with holder

Figure 5.13 shows the predicted wear volume over the sliding distance 180 m at the steady-state using Equation 5.7. The predicted wear volume is 5861×10^{-12} m^3, which differs less than 0.04% in regard to the theoretical calculation of 5859×10^{-12} m^3 using Equation 5.7. Therefore, the accuracy of the DEM prediction of wear is verified.

In addition, stability tests are carried out by repeating the simulation of the reference case three times. All the predictions from the repetitive tests give identical wear volume 5681×10^{-12} m^3. This demonstrates that highly accurate and stable predictions of wear volumes can be achieved by using the simulation model.
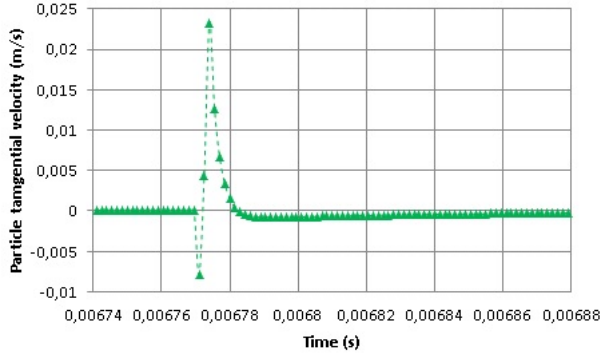
Figure 5.11: Numerical error when particle passes a mesh side
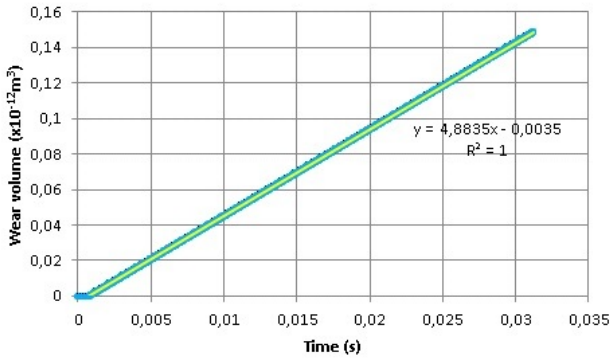
Figure 5.12: Wear volume as a function of time at the early stage
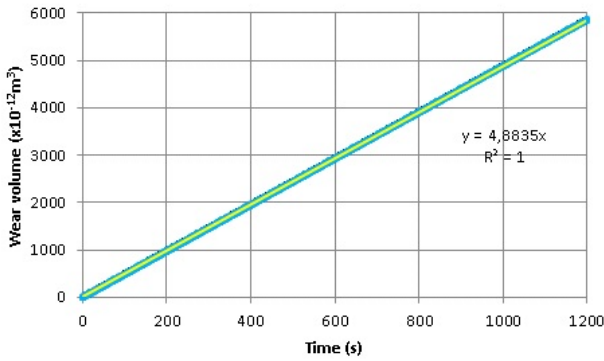
Figure 5.13: Wear volume for 20 mins (180 m) at the steady state

5.2.4   Sensitivity study of particle sliding wear

The previous discussions concluded that accurate and stable wear predictions can be achieved. Therefore, the wear loss for one revolution can be used to investigate the sensitivity of DEM parameters. This section presents the sensitivity analysis based on the real properties of the material. Besides, extended values of DEM parameters are investigated for reducing computational time.

Based on the determinations of DEM parameters in section 5.2.2, nine variables respectively from the categories of particle, disk, contact and simulation are identified. Table 5.10 lists the values of the nine variables used for the sensitivity study.

Table 5.10: Values of DEM parameter for sensitivity study

Categories	DEM parameters	Values
Particle	radius r_p [$\times 10^{-3}$m]	$1, 2, 3, 4$
	density ρ_p [kg/m^3]	$4750, 4850, 4950, 5050$
	Poisson ratio ν_p [–]	$0.23, 0.24, 0.25, 0.26$
	shear modulus G_p [GPa]	$60, 65, 70, 75$
Geometry	rotating speed ω_g [^{o}/s]	$2.27, 6.82, 11.36, 15.91$
	mesh size d_g [$\times 10^{-3}$m]	$0.55, 1.1, 2.2, 4.4$
Contact	coefficient of restitution e	$0.35, 0.40, 0.45, 0.50$
Simulation	indentation force F_p [N]	$3, 5, 7, 9$
	time step Δt [$\times 10^{-6}$s]	$1.0, 1.5, 2.0, 2.5$

For particle parameters, increasing the particle radius can cause significant increase of wear volume, which is shown in Figures 5.14. The significant increase is due to the extra gravitational force as a result of the increased particle mass which depends on the radius to the power three. By comparison, increasing particle density results in a minor increase (Figure 5.15). This is ascribed to the extra gravitational force as a result of the increase of particle mass which depends on the density to the power one. However, a change in the Poisson's ratio or the shear modulus shows no influence. The estimate wear remains the same volume of $4.50 \times 10^{-12} m^3$ as that of the theoretical calculation by using Equation 5.7.

For disk geometry parameters, it is examined that varying rotating speed has no influence on wear volume. This is because total sliding distance is maintained constant when varying rotating speeds. Referring to the experimental results (Figure 4.21) that limited variances occur with respect to varying sliding speeds, it confirms that wear is independent of the sliding speed at 0.05-0.35 m/s.

Although varying mesh sizes has no influence on wear, the area of wear distribution is affected, as shown in Figure 5.7. To achieve a uniform distribution of wear prediction, the maximum mesh size d_1 must be smaller than the particle radius r_p referring to the mesh setting used for the reference case (Figure 5.7). On the other hand, the minimal size is restrained by the diameter of the indented area, which is $2\sqrt{r_p \delta_n}$ (Appendix A). Therefore, the recommended mesh size setting is $2\sqrt{r_p \delta_n} < d_1 < r_p$.
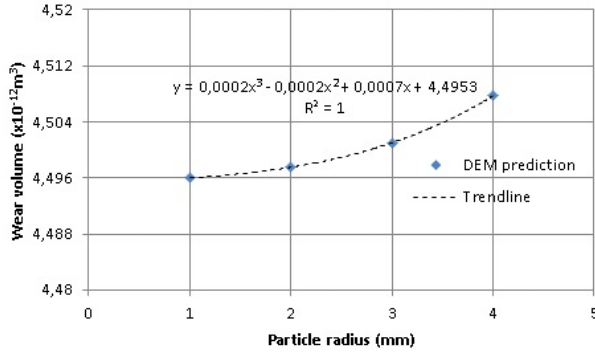
Figure 5.14: Wear as a function of particle radius
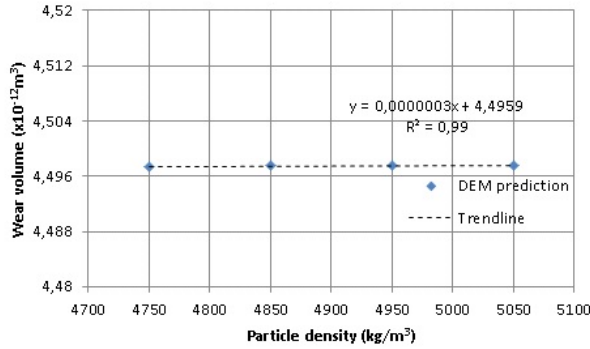
Figure 5.15: Wear as a function of particle density

For the contact parameter coefficient of restitution e, all the DEM predictions give the wear volume of 4.50×10^{-12} m^3 that is equivalent to the theoretical calculation. This is ascribed to that the coefficient of restitution has no influence on normal force F_n and thus not affecting wear at steady state.

For the simulation parameters, the wear volumes as a function of indentation force is illustrated in Figure 5.16. As predicted by Equation 5.7, wear volume increases proportionally to indentation force. The positive value of y-intercept means the wear loss simply by gravitational force. The time step has no influence on wear volume with respect to the determined values.

Thus far, the sensitivities of DEM parameters using the determined values based on material properties are obtained, which are given in Table 5.11. Table 5.11 shows that the sliding wear is not influenced by particle shear moduli nor by time step using the values from material real properties. In the DEM simulations, lowering shear moduli is preferable because it can enable reduction of computational time by using larger time steps [148]. Therefore, lower shear moduli will be explored with regard to the applicability in modeling sliding wear. Furthermore, simulations for a range of larger time steps are carried out.
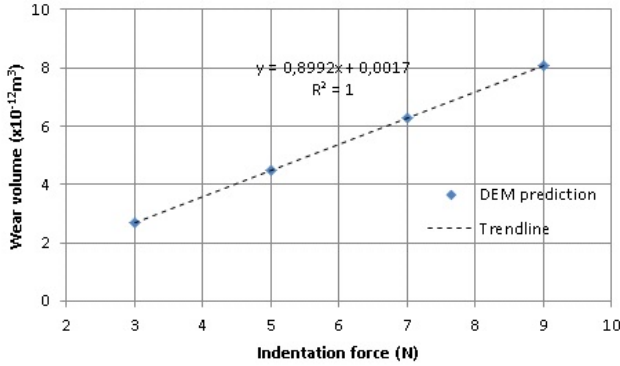
Figure 5.16: Wear volume as a function of indentation force

Table 5.11: Results of sensitivity studies based on material real properties

Categories	DEM parameters	Influences on wear volume
Particle	radius r_p $[\times 10^{-3} m]$	polynomial increase $y = 0.0002x^3 - 0.0002x^2 + 0.0007x + 4.4953$
	density ρ_p [kg/m^3]	linear increase $y = 0.0000003x + 4.4959$
	Poisson ratio ν_p [–]	no influence
	shear modulus G_p [GPa]	no influence
Geometry	rotating speed ω_g [^{o}/s]	no influence
	mesh size d_g $[\times 10^{-3}$m]	no influence
Contact	coefficient of restitution e [–]	no influence
Simulation	indentation force F_p [N]	linear increase $y = 0.8992x + 0.0017$
	time step Δt $[\times 10^{-6}$s]	no influence

The selection of lower shear moduli is based on the reference case values in Table 5.9, thus a series of particle shear moduli ΩG_p (Ω=1/10, 1/40, 1/70 and 1/100) are used. Simulation results demonstrated that wear volumes are not changed by lower moduli for steady-state stage. The reason is that the shear modulus has no influence on the normal force at the steady-state. Nevertheless, to reach the applied indentation force, the normal overlaps become higher and undergo longer unsteady time (Figure 5.17).

Considering the wear modeling bulk solids handing, the influences on normal overlap and time might affect the flow behaviors of bulk solids in direct contact with equipment. In addition, a change of particle shear modulus directly affects particle-particle interaction and thus bulk behavior as well. Therefore, for modeling the wear in bulk solids handling it is not appropriate to use lower particle shear moduli to reduce computation time.

The wear predictions of higher time steps use (160-240)%t_R, i.e. (3.0-4.5)$\times 10^{-6}$ s, and the results are plotted in Figure 5.18. It infers that accurate prediction of 4.50

$\times 10^{-12}$ m^3 can still be achieved as time step is increased to 3.50×10^{-6} s ($187\%t_R$). Thus, the maximum time step for modeling sliding wear can be set by $187\%t_R$.
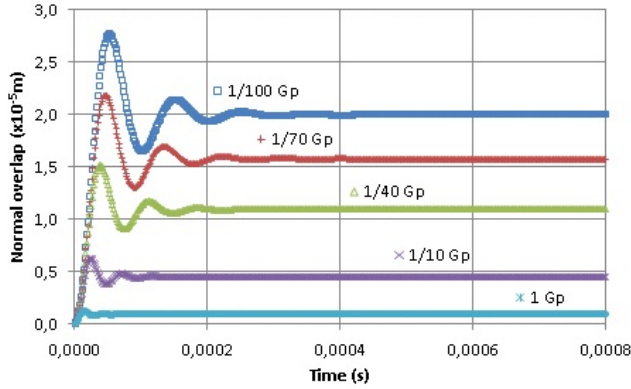
Figure 5.17: Normal overlaps as functions of particle shear moduli
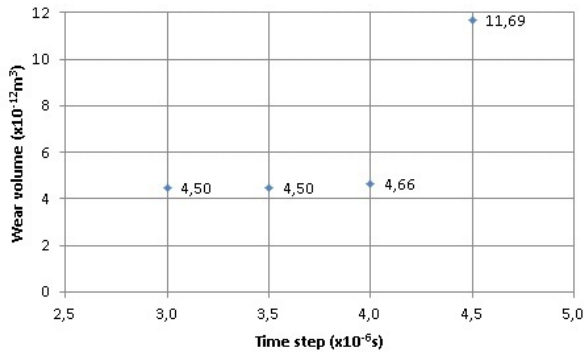
Figure 5.18: Wear volume with respect to higher time steps ($(160\text{-}240)\%t_R$)

In summary, the reliance of DEM prediction of particle sliding wear has been verified. This model can be used for predicting wear subjected to multiple particles.In the next section, the verification of DEM prediction of particle impact wear is presented.

5.3   Particle impact wear

In this section, the simulation model for modeling particle impact wear is presented. Using the determined parameter values, a reference case is carried out to evaluate the reliability of the DEM prediction. In addition, a sensitivity analysis is performed to study the impact of the selected DEM parameters.

5.3.1   Simulation model

Figure 5.19 presents the DEM simulation model used for predicting particle impact wear, which is built by using EDEM® 2.7.1 [149]. This model consists of a moving particle and a meshed rectangular geometry, which respectively represents a Sishen particle and mild steel plate. The particle is initially positioned at 0.02 m height relative to the geometry surface and is 0.02m distance from the plate center. The particle velocity has only a translational velocity v_p. The sizes of the rectangular plate (length, width and height) are 53 mm $\times$ 48 mm $\times$ 6 mm.
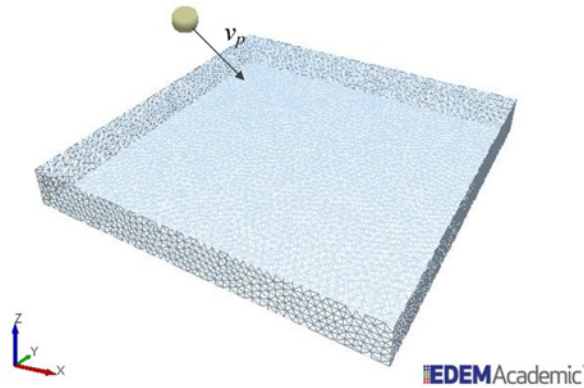
Figure 5.19: Simulation model of particle impact wear

Figure 5.20 illustrates the simulation cycle for the wear prediction by single particle impact. It consists of five procedures: namely, generate a particle, assign particle motion, detect contact, calculate contact energy and update contact [153]. In this simulation model, it is noted that particle impact wear is estimated from cumulative cutting energy $E_{k,c}$ and cumulative deformation energy $E_{k,d}$. This is based on the impact wear Equation 5.18 [56, 57, 64],
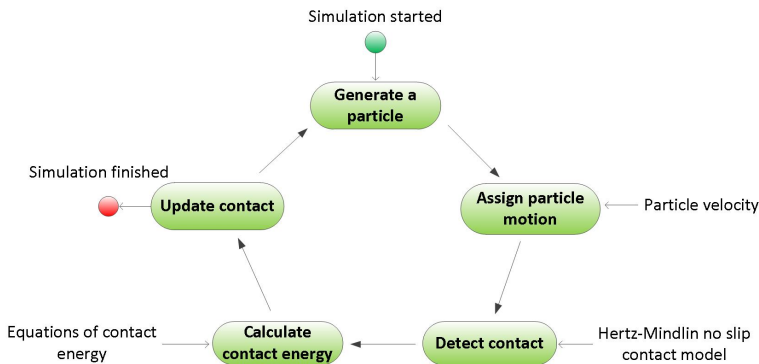
Figure 5.20: Simulation cycle for particle impact wear based on [153]

$$W_{V,e} = \frac{E_{k,c}}{\varepsilon_c} + \frac{E_{k,d}}{\varepsilon_d} \tag{5.18}$$

in which ε_c and ε_d are cutting and deformation factors. $E_{k,c}$ and $E_{k,d}$ are given by Equations 5.19(a-b) [117, 134, 136],

$$\begin{cases} E_{k,c} = \sum |F_t v_t \Delta t| & \text{(5.19a)} \\ E_{k,d} = \sum |F_n v_n \Delta t| & \text{(5.19b)} \end{cases}$$

5.3.2   Determination of DEM parameters

Similar to the determinations of DEM parameter values used to predict particle sliding wear, all the DEM parameters for predicting particle impact wear by using the simulation model (Figure 5.20) are classified into four categories. These four categories are: particle, geometry, contact and simulation.

For the particle parameters, according to the contact energy Equation 5.19, and using Tables 5.1 and 5.2, five particle parameters must be determined for predicting impact wear, which are:

(1) radius r_p;

(2) density ρ_p;

(3) Poisson's ratio ν_p;

(4) shear modulus G_p;

(5) velocity v_p;

The determinations of radius, density, Poisson's ratio and shear modulus are identical to those for particle sliding wear. However, the particle velocities is set at 1-7 m/s according to bulk solids handling conditions [4].

For the geometrical parameters, the material of the modeled rectangular geometry is identical to the disk used in the simulation model for predicting particle sliding wear. Therefore, the same values for the same below geometry parameters are applied.

(1) density ρ_p;

(2) Poisson's ratio ν_p;

(3) shear modulus G_p;

(4) mesh size d_g;

Three contact parameters are applied at that for modeling particle sliding wear,

(1) coefficient of restitution e;

(2) coefficient of static friction μ_{st};

(3) coefficient of rolling friction μ_r;

For the coefficients of restitution and rolling friction, the same values for particle sliding wear are applied. For the coefficient of static friction, it is estimated at 0.5-0.8 by referring to the experimental tests of iron ore pellets [129].

The wear energy Equation 5.19(a-b) show that the impact angle and time step need to be determined. Besides, the gravitation acceleration have to be specified.

(1) impact angle β;

(2) time step Δt;

(3) gravitational acceleration g_i;

The investigated values of impact angles lie in 15-60°. The time step is approximated by 1/10 of the collision time (t_c) based on Equation 5.20 [136, 162]. Meanwhile, the time step can also be determined by using Rayleigh time step [136]. The gravitational acceleration is set to zero for the simplicity of calculating particle velocities before and after impact.

$$t_c = 2.87 \times \left[\frac{(m^*)^2}{r^*(E^*)^2 v_p} \right]^{1/5} \tag{5.20}$$

5.3.3 Reference case of impact wear prediction

On the basis of the discussions in section 5.3.2, a reference case is determined to model the impact wear of mild steel surface by a Sishen particle. Table 5.12 lists the values for the DEM parameters of the reference case. Figure 5.21 shows the predicted cumulative cutting energy of the reference case.

Furthermore, the predicted cumulative cutting energy and cumulative deformation energy is illustrated in Figure 5.22. It is seen that both cumulative cutting and cumulative deformation energy increases sharply during impact process. The predicted cumulative cutting energy and cumulative deformation energy after impact are $0.21 \times 10^{-3} J$ and $0.23 \times 10^{-3} J$, respectively.

In addition, the cutting and deformation forces are also plotted (Figure 5.22). It is seen that the cutting force is governed by the deformation force, which is as expected based on Equation 5.5. By using impulse-momentum theory (Equation 5.21), the normal force and tangential force can be verified.

Table 5.12: Values of DEM parameters for reference case

Categories	DEM parameters	Values
Particle	radius $r_p [\times 10^{-3} \text{m}]$	2
	density $\rho_p [\text{kg/m}^3]$	4850
	Poisson's ratio ν_p [–]	0.24
	shear modulus G_p [GPa]	65
	velocity v_p [m/s]	3
Geometry	density $\rho_g [\text{kg/m}^3]$	7932
	Poisson's ratio ν_g [–]	0.3
	shear modulus G_p [GPa]	78
	mesh size $d_g [\times 10^{-3}]$ m	1.1
Contact	coefficient of restitution e [–]	0.4
	coefficient of static friction μ_s [–]	0.6
	coefficient of rolling friction μ_r [–]	0
Simulation	impact angle β [°]	30
	time step $\Delta t [\times 10^{-6} \text{s}]$	1.0
	gravitational acceleration g_i [m/s^2]	0
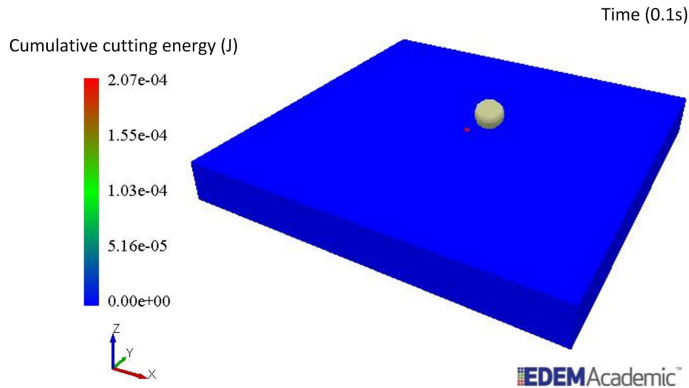
Figure 5.21: Simulation result for single particle impact wear

$$\boldsymbol{F}_n t_c = m_p(\boldsymbol{v}_{p,0,n} - \boldsymbol{v}_{p,1,n}) \qquad (5.21)$$

The normal force is calculated by,

$$F_n = m_p(v_{p,0,n} + v_{p,1,n})/t_c \qquad (5.22)$$

Correspondingly, the tangential force is given by,

$$F_t = \mu_{st} F_n \qquad (5.23)$$

Using Equations 5.22 and 5.23, the average normal force and average tangential force are calculated at 28.4 N and 17.2N. Based on the DEM prediction (Figure

5.23) of the average normal force (25.2 N) and average tangential force (15.1 N), it indicates that the DEM predictions are 11% smaller than the theoretical values. In addition, repeated simulations of the reference case are carried out, which all give the same predictions. Based on the analysis, it is concluded that this simulation model can provide acceptable predictions of particle impact wear.
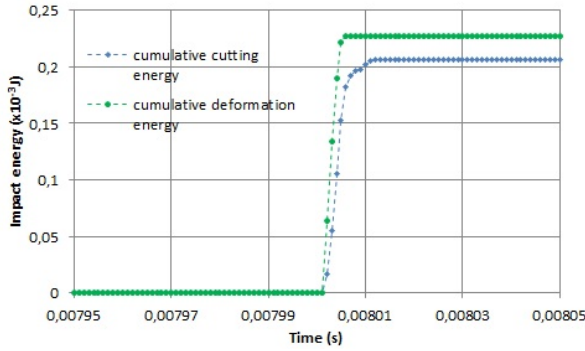
Figure 5.22: Cumulative cutting and deformation energy as a function of time
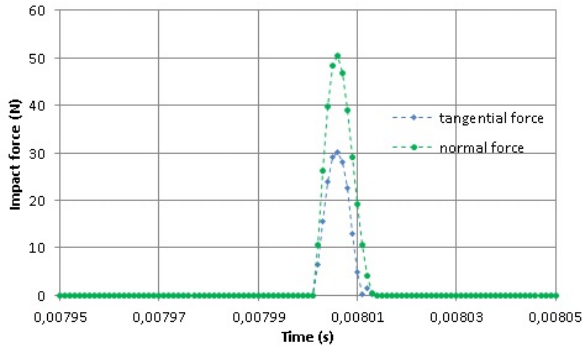
Figure 5.23: Cutting and deformation (normal and tangential) forces as a function of time

5.3.4 Sensitivity study of particle impact wear

Based on the parameter determinations in section 5.3.2, total nine variables are identified from the three categories of particle, contact and simulation. To examine the sensitivities of these nine parameters on particle impact wear, the test values are presented in Table 5.13. In combination with other values from reference case (Table 5.12), the impact wear energy is predicted with respect to the nine parameters, which are shown in Figures 5.24–5.33.

For the particles parameters, simulations demonstrates that particle radius, density and velocity have influences on wear. By comparisons, particle Poisson's ratio

and shear modulus have negligible influences. Figure 5.24 presents the cumulative cutting and deformation energy as functions of particle radius. It shows that both cumulative cutting and cumulative deformation energy undergo polynomial increase with increasing particle radius. This is due to the fact that particle mass increases with increasing particle radius by the power three.

Table 5.13: Values of DEM parameters for sensitivity study

Categories	DEM parameters	Values
Particle	radius r_p [$\times 10^{-3}$]m density ρ_p[kg/m^3] Poisson's ratio ν_p [–] shear modulus G_p [GPa] velocity v_p [m/s]	$1, 2, 3, 4$ $4750, 4850, 4950, 5050$ $0.23, 0.24, 0.25, 0.26$ $60, 65, 70, 75$ $1, 3, 5, 7$
Contact	coefficient of restitution e [–] coefficient of static friction μ_s [–]	$0.35, 0.40, 0.45, 0.50$ $0.5, 0.6, 0.7, 0.8$
Simulation	impact angle β [^{o}] time step Δt [$\times 10^{-6}$s]	$15, 30, 45, 60,$ $0.5, 1.0, 1.5, 2.0$

Figure 5.24: Impact wear energy as a function of particle radius

Figure 5.25 illustrates the cumulative cutting and deformation energy as functions of particle density. It shows that both cumulative cutting energy and cumulative deformation energy increases approximately in parallel with respect to the increase of particle density. This is ascribed to the fact that the linear increase of particle mass as a result of increasing density.

Figure 5.26 presents the cumulative cutting and deformation energy as functions of particle Poisson's ratio. It is seen that both cumulative cutting energy and cumulative deformation energy experiences a slight linear increase. This can be interpreted as, when Poisson's ratio is increased, the equivalent Young's modulus is increased (Table 5.2) and thus the range of normal force F_n is wider (Equation 5.4), which also results in wider range of tangential force (Equation 5.5). Accordingly, the cumulative cutting and deformation energy is higher.

Figure 5.27 presents the cumulative cutting and deformation energy as functions of particle shear modulus. It is observed that increasing shear modulus causes a

very minor increase on deformation energy, whilst no difference is observed on cumulative cutting energy. This reason is that when increasing shear modulus, the Young's modulus is increased (Table 5.2) and thus the range of normal force becomes larger (Equation 5.4). Nevertheless, the impact of the tested range is less insignificant to tangential force according to Equation 5.5.
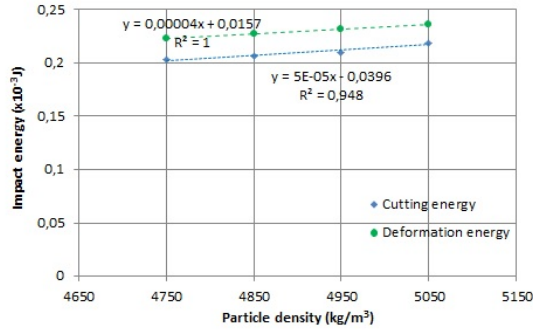
Figure 5.25: Impact wear energy a function of particle density
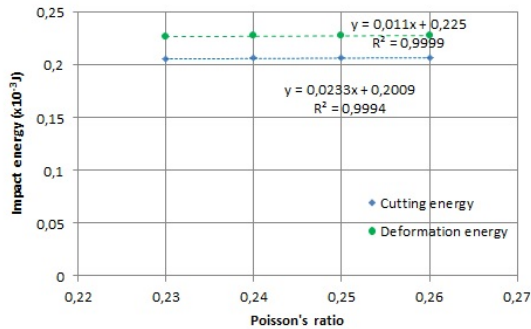
Figure 5.26: Impact wear energy as a function of particle Poisson's ratio
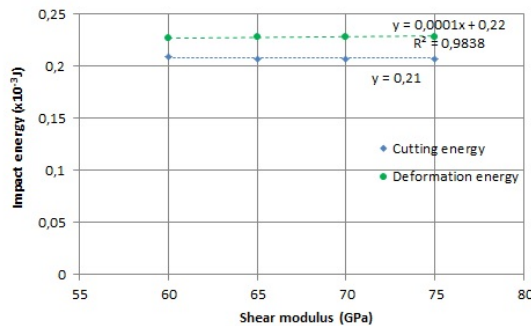
Figure 5.27: Impact wear energy as a function of particle shear modulus

Figure 5.28 shows the cumulative cutting and deformation energy as a function of particle velocity. It is seen that both cutting and deformation energy experiences exponential rise. The reason is that the kinetic energy increases with increasing particle velocity. In addition, it is noticed that the deformation energy increases more than the cutting energy, which is ascribed to the fact that increasing particle velocity causes larger change to the normal force than the tangential.

For the contact parameters (coefficients of restitution and static friction), it is examined that for both parameters, the cumulative cutting energy experiences an increase whilst the cumulative deformation energy maintains constant, which are shown in Figures 5.29 and 5.30. The reason for the increase of cumulative cutting energy by increasing coefficient of restitution is that the damping coefficient D_t is decreased, which results in the increase of the variance of tangential force and thus that the tangential energy is increased. However, the deformation energy is not sensitive to coefficient of static friction within the test range. The increase of cumulative cutting energy by increasing the coefficient of static friction is also due to the increase of tangential force (Equation 5.5).
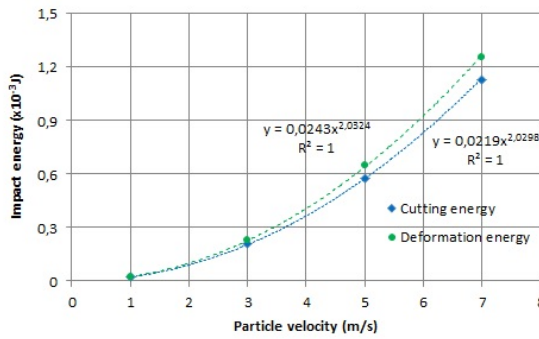
Figure 5.28: Impact wear energy as a function of particle velocity
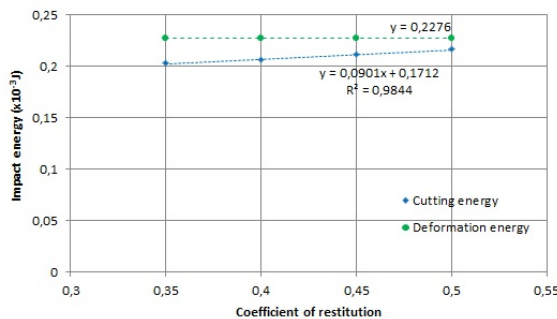
Figure 5.29: Impact wear energy as a function of coefficient of restitution

For the simulation parameters (impact angle and time step), the predicted impact energy is shown in Figures 5.31 and 5.32. It is observed from Figure 5.31 that the cumulative cutting energy has a peak value at 30° impact angle as is also

predicted in [117]. The cumulative deformation energy maintains a polynomial increase. For the determined time steps in Table 5.13, both cumulative cutting and cumulative deformation energy maintains increasing trends. However, due to the fact that the kinetic energy is the unchanged, the total energy must be at a relative steady value. Therefore the increased time steps are investigated (Figure 5.33.)
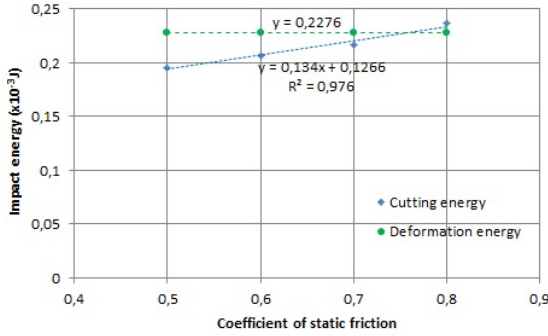
Figure 5.30: Impact wear energy as a function of coefficient of static friction
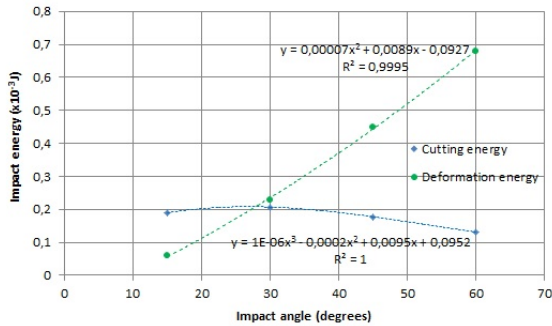
Figure 5.31: Impact wear energy as a function of impact angle
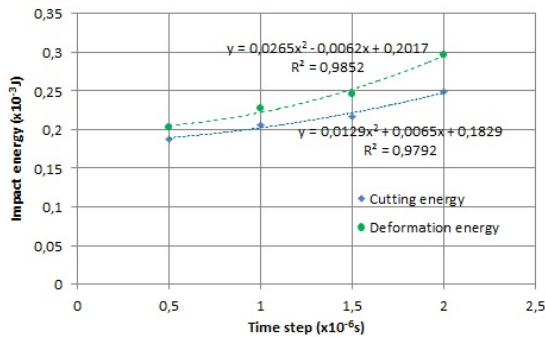
Figure 5.32: Impact wear energy as a function of time step

Figure 5.33 demonstrates that both cumulative cutting and deformation energy arrives at a relatively constant value at 3.5×10^{-6}s. For higher values than that, the impact energy becomes unsteady with large variations. Thus, for modeling particle impact wear, the maximum time step is also limited at $187\% t_R$.
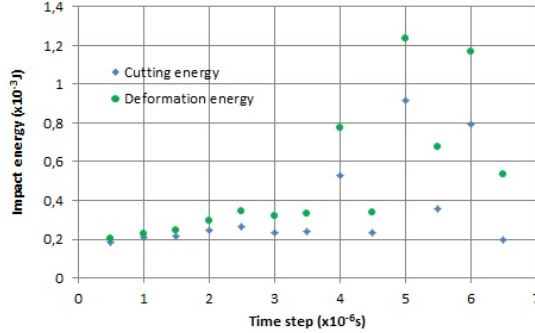
Figure 5.33: Impact wear energy as a function of time step of an increased range

5.4   Conclusions

To answer the subquestion of *"How to predict the surface wear of bulk solids handling equipment by using the DEM simulations?"*, this chapter verifies wear predictions of particle sliding test and particle impact test, respectively from two simulation models. Four conclusions are drawn below.

(1) Using the Hertz-Mindlin no-slip contact model, the sliding wear at steady state for a single particle can be accurately predicted.

(2) The effects of the selected DEM parameters on the prediction of wear volume are obtained by conducting a sensitivity study. This provides significant references for modeling the sliding wear in bulk solids handling.

(3) Using the Hertz-Mindlin no-slip contact model, the DEM predictions are 11% smaller than the theoretical estimation. Under this deviation, the prediction of the corresponding particle impact energy is acceptable.

(4) The effects of the DEM parameters on the predictions of particle impact energy are revealed. This is useful to the selections of appropriate values for modeling the erosive wear in bulk solids handling.

This chapter presents the verifications of DEM predictions of particle sliding wear and particle impact wear. In the next chapter, an abrasive wear scenario in bulk solids handling is modeled to evaluate wear from bionic surfaces and a smooth surface.

6 | CHAPTER

Abrasive wear reduction of bulk solids handling equipment surfaces[*]

Chapter 4 and chapter 5 respectively presented experimental and simulation investigations for predicting wear of a steel surface by a single iron ore particle. In combination with modeling flow behavior of iron ore bulk solids, the wear loss for the conventional and bionic surfaces of bulk solids handling equipment can be predicted.

This chapter numerically demonstrates the abrasive wear reduction of a bionic surface in comparison to a conventional smooth one. In this chapter, section 6.1 describes the reference case of an abrasive wear scenario; section 6.2 illustrates the determinations of DEM parameters; section 6.3 determines the wear prediction of a conventional smooth surface; section 6.4 provides the wear predictions of bionic surfaces. Finally, conclusions are given in section 6.5.

6.1   Referential setup for modeling abrasive wear

As was explained in chapter 2, a loading chute can suffer from severe abrasive wear on the bottom surface (Figure 2.17) [4]. Therefore, bionic design was introduced to investigate the possibility of wear reduction. This reduction can be studied by using the DEM simulations. To model the wear of conventional and bionic surfaces of a chute bottom, the referential setting for this scenario (Figure 2.17b) is determined in this section.

To efficiently model wear of the chute surface, from a computational point of view using the DEM, the number of particles must be reduced. Therefore, the modeled

widths of the belt and the loading chute are one fifth of real sizes [4]. The determined values of dimensions and positions for modeling the abrasive wear of the loading chute bottom surface are given in Table 6.1 [4].
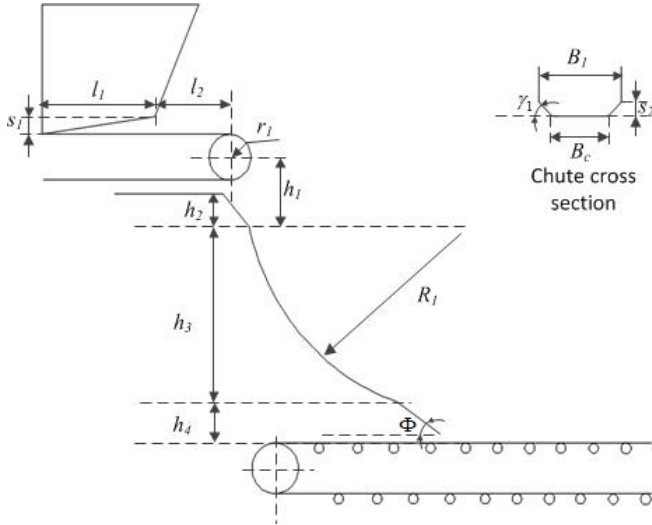
Figure 2.17b: Positions and dimensions of the transfer equipment based on [4]

Table 6.1: Referential dimensions and positions of a loading chute based on [4]

Denotations	B_1	B_c	h_1	h_2	h_3	h_4	l_1	l_2	R_0	R_1	S_1	S_2
Values (m)	0.3	0.2	0.5	0.3	1.8	0.4	0.5	0.25	0.2	2.0	0.2	0.2

Corresponding to the used dimensions and positions (Table 6.1), the applied initial feed rate is 100 t/h and the speed of the belt is 0.20 m/s [4]. By neglecting air drag, the calculated horizontal and vertical velocities of bulk solids at the initial contact with respect to the surface of chute bottom are $v_{x,0} = 0.20$ m/s and $v_{y,0} = -5.33$ m/s (Equation 2.45), respectively. The angle between bottom and inclining side is determined by $\gamma_1 = 45^o$ [4]. To achieve self-cleaning by the transported iron ore, the chute cut-off angle is set to $\Phi \approx \theta_w + 5^o = 30^o$ by using the measured wall friction angle θ_w in chapter 4.

For this transfer process, the interacting particles with respect to chute bottom surface have sliding and also rolling motions. The sliding and rolling behaviors of particles will be modeled by using DEM. However, to quantify the abrasive wear, the wear caused by particle rolling is not accounted for since it has a minor contribution [4, 35]. Therefore, the abrasive wear loss is quantified solely from sliding wear (Equation 5.7).

6.2 Determination of DEM parameters

As shown in chapter 5, all parameters for carrying out a DEM simulation are categorized into particle, geometry, contact and simulation parameters. To determine the values of the DEM parameters for modeling wear by multiple particles, the determinations in chapter 5 for a single particle are used. In addition, experimental and simulation tests to model bulk flow behavior [130] are carried out thus all DEM parameters are determined.

6.2.1 Particle parameters

For the particle parameters, the particle sizes of experimental sample of Sishen iron ore are given in Figure 6.1. However, the used particle size range is 3-8 mm to reduce computational time by decreasing particle number. Figure 6.1 also shows the modeled particle size distribution. To ensure that the chosen particle sizes can correctly represent the flow behavior as in practice, the experimental and simulation of bulk flow behavior [164] are performed (Figure 6.6), which is presented in section 6.2.5. The average particle density was measured at 4865 kg/m^3 (chapter 4). Other particle parameters are stated in Table 5.3. Table 6.2 summaries the determined values for particle parameters.
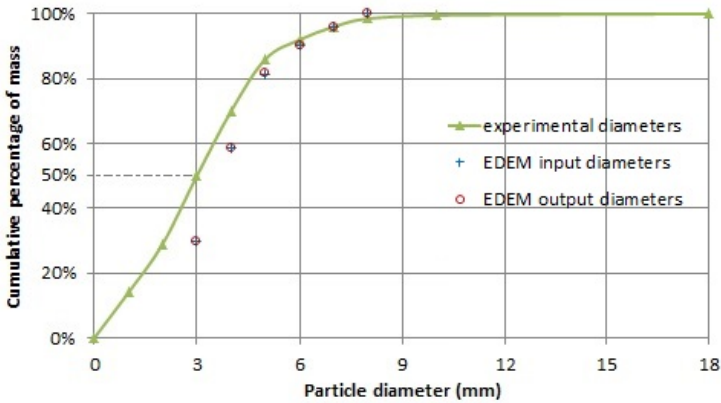
Figure 6.1: Particle size distribution for the wear modeling

Table 6.2: Values for particle parameters

Category	Wear aspect	DEM parameters	Values
Particle	iron ore	radius r_p [$\times 10^{-3}$m]	1.5 – 4
		density ρ_p[kg/m^3]	4865
		Poisson's ratio ν_p [–]	0.24
		shear modulus G_p [GPa]	65

6.2.2   Geometry parameters

In this research, the material of the chute surface is mild steel. The density, Poisson's ratio and shear modulus of the mild steel surface were determined in chapter 5 (Table 5.4). The geometrical dimensions are given in Table 6.1. To predict wear of chute bottom surface using DEM, the chute geometry must be carefully meshed. The Ansys Workbench 16.2 [158] is used for meshing. The applied mesh setting preferences are: CFD-Fluent, high smooth sizing and using max face size of 0.006 m. Table 6.3 gives the values of the chute geometry parameters.

Table 6.3: Values for geometry parameters

Category	Wear aspect	DEM parameters	Values
Geometry	chute	density ρ_g[kg/m^3]	7932
		Poisson ratio ν_g [–]	0.3
		shear modulus G_p [GPa]	78
		maximal mesh size d_g [$\times 10^{-3}$m]	6.0

6.2.3   Contact parameters

The contact parameters involve the two types, namely, iron ore/iron ore and iron ore/steel. For the parameters subjected to iron ore/iron ore contact, the adopted coefficient of restitution is 0.45 based on [129]. The coefficients of static and rolling friction for the interactions of iron ore particles are determined by simulating bulk solids behavior (section 6.2.5) [165]. For iron ore/chute contact, the coefficient of restitution were discussed in chapter 5. The applied coefficients of static friction and rolling friction are given by 0.46 and 0.3 according to experimental tests (chapter 4). Table 6.4 presents the values for the iron ore/chute contact parameters.

Table 6.4: Values for the iron ore/chute contact parameters

Category	Wear aspect	DEM parameters	Values
Contact	iron ore/chute	coefficient of restitution e [–]	0.4
		coefficient of static friction μ_{st} [–]	0.46
		coefficient of rolling friction μ_r [–]	0.3

6.2.4   Simulation parameters

There are six simulation parameters must be determined, namely, particle generation rate, initial horizontal velocity, initial vertical velocity, coefficient of sliding wear, total time and time step. In DEM simulations, a particle factory is utilized to generate bulk solids with specific flow rate and velocities [149]. In combination with the determinations of the modeled scenario in section 6.1, the experimental tests in chapter 4 and the determination of time step in chapter 5, the values for the six simulation parameters are obtained, as given in Table 6.5.

Table 6.5: Values for simulation parameters

Category	Wear aspect	DEM parameters	Values
Simulation	conditions	particle generation rate q_b [kg/s]	27.78
		initial horizontal velocity v_y [m/s]	0.2
		initial vertical velocity v_z [m/s]	5.33
		coefficient of sliding wear $\alpha_{s,e}$ [$\times 10^{-13} m^2/N$]	3.0
		total time Δt [s]	4.0
		time step Δt [$\times 10^{-6}$s]	1.5

6.2.5   Experimental and simulation of bulk flow behavior

To obtain the input values of DEM parameters of iron ore, an experimental setup was designed (Figure 6.6) based on the inclining surface tester (Figure 4.28). This tester can be used to predict bulk flow behavior [166, 167]. To start a test, the front sheet must be instantly released by quickly rotating it upwards. Simultaneously, the bottom surface starts to rotate against an axis (Figure 4.28). A bin with a steel bottom surface is used to receive the bulk solids falling from the inclining surface. During the experimental tests, two rotating speeds, namely, 0.18 ^{o}/s and 1.31 ^{o}/s are used. For each speed the tests are repeated eight times. The same material is reused after one test.

The parameters for modeling the experimental test are based on sections 6.2.1-6.2.4. The same particle characters as in section 6.2.1 is used. For the geometry parameters, a rectangular steel sheet is prepared for the experimental test (Figure 6.6).In addition, a feeder constructed by acrylic sheets is used to store the sample of iron ore bulk solids. The density, Poisson's ratio and shear modulus of acrylic sheet are given by 1136 kg/m^3, 0.4 and 11 GPa [136, 168]. These geometries are generated by using the built-in models in the software EDEM® 2.7.1 [149]. Other dimensions are identical to the experimental setup (Figure 6.6).

For the contact between iron ore and acrylic sheet, the coefficient of restitution, the coefficient of static friction and the coefficient of rolling friction are determined at 0.5, 0.24 and 0.22 [136, 168]. To enable effective modeling, the periodic boundary [169] is used to reduce simulation scale. Accordingly, the modeled domain is decreased while still maintaining the ratio of domain width to particle size $Z_s/d_{max} > 4$ [169].

Based on preliminary simulations of the experimental tests, the rotating speed can be increased up to ten time while still maintaining similar bulk flow behavior. Therefore, to reduce computational time, ten times of the experimental speeds are applied in simulations, which are 1.8 ^{o}/s and 13.1 ^{o}/s respectively. In the simulations, three repetitive simulations are done to obtain the error range subjected to one rotating speed. Using the trial-and-error method, the bulk flow behavior is modeled by comparing three angles (Ψ_1, Ψ_2 and Ψ_3) from experiments and simulations (Figure 6.2). Figure 6.2 shows three snapshots from Experiment 1 and Simulation 1.

Figure 6.2 shows that the simulated bulk flow behavior maintains high similarities with the results of the experiments. However, after all particles have fallen onto

the bin bottom (Figure 6.2c), the bulk pile is unstable due to the fact that the used spherical particles can maintain horizontal speeds as a result of low resistance between particles and bin bottom surface. In practice, the pile shape is steady due to higher sliding resistance generated by non-spherical particles. Therefore, the angle Ψ_3 is determined when the kinetic energy of total particles reach a relatively stable and low value (1.8×10^{-5} J).
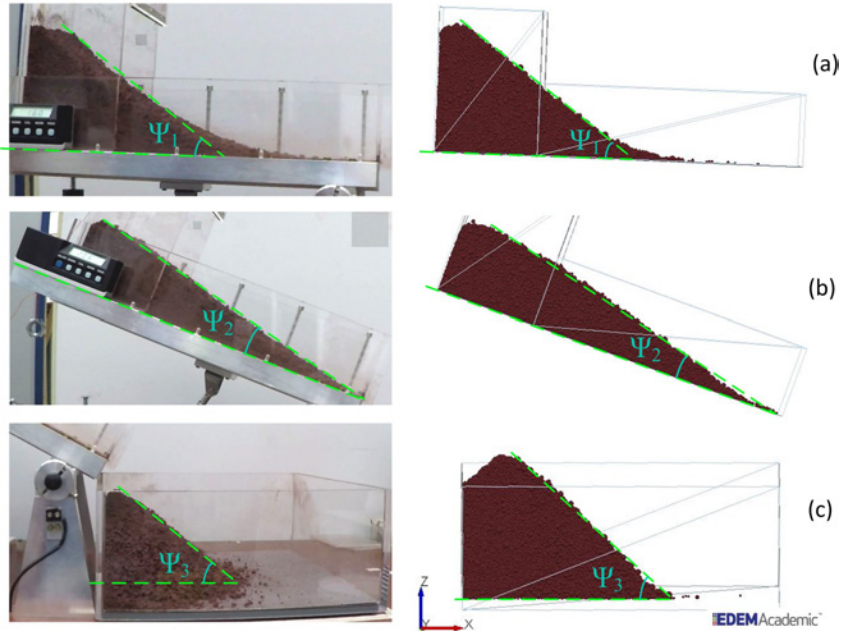
Figure 6.2: Iron ore bulk flow behavior from Experiment 1 and Simulation 1 (a) angle by ledge test (b) angle of bulk flow and (c) angle of repose

Table 6.6: Comparisons of three angles obtained by experiments and simulation

	Particle radius r_p [$\times10^{-3}$ m]	Rotating speed ω_s [$^\circ$/s]	Angle 1 Ψ_1 [$^\circ$]	Angle 2 Ψ_2 [$^\circ$]	Angle 3 Ψ_3 [$^\circ$]
Experiment 1	0-9	0.18	33.8±0.7	35.6±1.2	38.9±1.1
Simulation 1	1.5-4	1.8	35.4±0.2	35.4±0.7	42.4±1.4
Experiment 2	0-9	1.31	33.7±0.9	37.7±0.7	33.3±0.8
Simulation 2	1.5-4	13.1	32.7±0.6	37.8±0.4	33.8±0.9

The measured three angles (Ψ_1, Ψ_2 and Ψ_3) from both simulations and experiments are summarized in Table 6.6. Although the angle Ψ_3 (in Simulation 1) falls outside the range of experimental results, the other angles from the simulations lie in the experimental ranges. Thus the input values for the DEM simulation can be used to model the flow behavior of iron ore bulk solids. Table 6.7 lists the values used in the DEM simulations, in which the error range for the angles are obtained using 95% confidence interval.

Table 6.7: Values of DEM parameters for iron ore bulk flow behavior

Categories	Items	DEM parameters	Values
Particle	iron ore	radius r_p [$\times 10^{-3}$m] density ρ_p [kg/m^3] Poisson's ratio ν_p [–] shear modulus G_p [GPa]	$1.5 - 4$ 4865 0.24 65
Geometry	steel sheet	density ρ_g [kg/m^3] Poisson's ratio ν_g [–] shear modulus G_p [GPa]	7932 0.3 78
	acrylic sheet	density ρ_g [kg/m^3] Poisson's ratio ν_g [–] shear modulus G_p [GPa]	1136 0.4 1.1
Contact	iron ore/iron ore	coefficient of restitution e [–] coefficient of static friction μ_s [–] coefficient of rolling friction μ_r [–]	0.45 0.41 0.22
	iron ore/steel sheet	coefficient of restitution e [–] coefficient of static friction μ_{st} [–] coefficient of rolling friction μ_r [–]	0.4 0.46 0.3
	iron ore/acrylic sheet	coefficient of restitution e [–] coefficient of static friction μ_{st} [–] coefficient of rolling friction μ_r [–]	0.5 0.24 0.22
Simulation	conditions	total mass of bulk solids m_b [kg] mass generating rate q_b [kg/s] initial velocity of bulk solids v_z [m/s] rotating speed v_0 [$^o/s$] time step Δt [$\times 10^{-6}$s]	2.78 1.5 1.0 1.8, 13.1 1.5

6.3   Abrasive wear prediction of a smooth surface

Using the sliding wear prediction model in chapter 5 and the determined DEM values in Tables 6.2-6.5 and 6.7, the abrasive wear for the iron ore handling conditions can be predicted. This section illustrates the DEM prediction of abrasive wear on a smooth surface of the loading chute. In addition, the theoretically calculation of the abrasive wear volume prediction is provided.

6.3.1   Simulation model

Table 6.8 presents the geometry and simulation parameters for modeling abrasive wear on a loading chute. Using the software EDEM 2.7.1$^®$ [149], the DEM model for abrasive wear prediction is built as depicted in Figure 6.3(a). To efficiently model wear process, the particle factory is adjusted and placed close to the area where the bulk solids begin to have contact with the chute bottom (Figure 6.3b). The height of the particle factory is 0.1 m and the width equates to the width of the chute bottom.

Table 6.8: Values for modeling abrasive wear on loading chute

Categories	Wear aspects	DEM parameters	Values
Particle	iron ore	radius r_p [$\times 10^{-3}$m]	1.5 – 4
		density ρ_p[kg/m^3]	4865
		Poisson ratio ν_p [–]	0.24
		shear modulus G_p [GPa]	65
Geometry	chute	density ρ_g[kg/m^3]	7932
		Poisson ratio ν_g [–]	0.3
		shear modulus G_p [GPa]	78
		maximal mesh size d_g [$\times 10^{-3}$m]	6.0
Contact	iron ore/iron ore	coefficient of restitution e [–]	0.45
		coefficient of static friction μ_{st} [–]	0.41
		coefficient of rolling friction μ_r [–]	0.22
	iron ore/chute	coefficient of restitution e [–]	0.4
		coefficient of static friction μ_{st} [–]	0.46
		coefficient of rolling friction μ_r [–]	0.3
Simulation	conditions	particle generation rate q_b [kg/s]	27.78
		initial horizontal velocity v_y [m/s]	0.2
		initial vertical velocity v_z [m/s]	5.33
		coefficient of sliding wear $\alpha_{s,e}$ [$\times 10^{-13} m^2/N$]	3.0
		total time Δt [s]	4.0
		time step Δt [$\times 10^{-6}$s]	1.5

(a)   (b)

Figure 6.3: Simulation model for predicting abrasive wear on a loading chute (a) modeling a transfer process (b) modified particle factory

6.3.2 Results

Figure 6.4 presents the wear prediction for the smooth chute surface corresponding to Figure 6.3b. In this figure, three wear zones 1-3 are identified. Zone 1 is the curved surface to which severe wear occurs due to the high normal force triggered by the impact of bulk solids. Zone 2 represents the curved surface which suffers the sliding wear, and Zone 3 shows the wear of the straight surface when bulk solids recontact and travel off the chute. The legend bar denotes the range of the total wear loss for individual meshes through the feeding time.
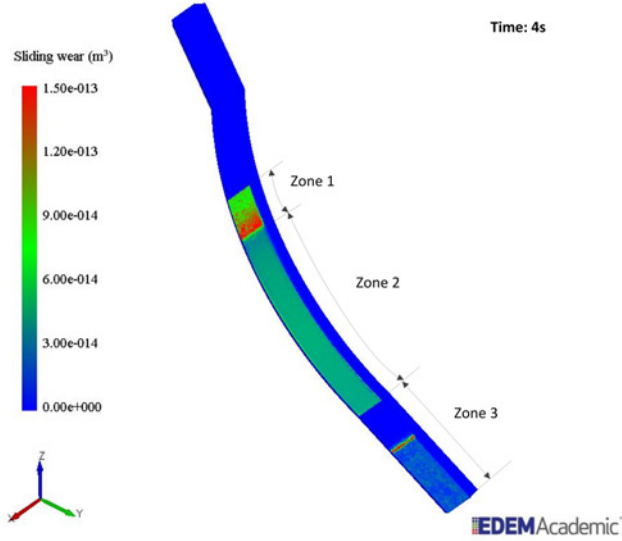
Figure 6.4: Abrasive wear prediction of a smooth surface of a loading chute

Simulations show that after 0.5 s a steady bulk flow is achieved. The predicted wear rates for the three zones 1-3 are $Q_{q_b,s,1} = 0.97 \times 10^{-10} \text{m}^3/\text{s}$, $Q_{q_b,s,2} = 1.72 \times 10^{-10} \text{m}^3/\text{s}$ and $Q_{q_b,s,3} = 0.48 \times 10^{-10} \text{m}^3/\text{s}$. By repeating this simulation three times, it is calculated that the wear loss deviates by 1.0%. This deviation is acceptable in comparison to total wear loss.

6.3.3 Theoretical calculation

Section 6.3.2 presented the predicted wear rates for the three zones 1-3. The results of Zones 1 and 3 are affected by the impact forces generated by bulk solids impacts. Nevertheless, Zone 2 can be theoretically verified by using theoretical calculations. Based on Equations 2.41 and 4.3, the wear rate by the sliding of bulk solids for the curved surface of chute bottom is,

$$Q_{q_b,s} = \alpha_{s,e} q_b \int_{\theta_{L,0}}^{\theta_{L,m}} [v_s(\theta_L)^2 + R_1 g \sin \theta_L] d\theta_L \qquad (6.1)$$

where $\theta_{L,0}$ and $\theta_{L,m}$ are chute slope angles corresponding to two locations that bulk solids start to contact and leave the bottom surface.

The velocity of bulk solids at any location θ_L is given by [4],

$$v_s(\theta_L)^2 = \frac{2gR_1}{4\mu_e^2 + 1}[(1 - 2\mu_e^2)\sin\theta_L + 3\mu_e\cos\theta_L] + \Gamma e^{-2\mu_e\theta_L} \tag{6.2}$$

in which μ_e is estimated at 0.4 based on the assumption of transporting a shallow layer of iron ore particle and thus having low pressure. Accordingly, μ_e is calculated at 0.47 using Equation 2.43. For the modeled case in Figure 6.3, Γ is evaluated by [4]

$$\Gamma = \{v_0^2 - \frac{2gR_1}{4\mu_e^2 + 1}[(1 - 2\mu_e^2)\sin\theta_L + 3\mu_e\cos\theta_L]\}e^{2\mu_e\theta_L} \tag{6.3}$$

Using $v = v_0 = 5.34m/s$ at $\theta = \theta_0 = 28.36^o$, it is obtained that $\Gamma = -4.68$.

To estimate the wear rate for Zone 2, the chute slope angles $\theta_{L,0}$ and $\theta_{L,m}$ are measured at 35.34^o and 64.15^o, respectively. By inserting Γ into Equation 6.2, and integrating Equation 6.1, the theoretical wear rate for Zone 2 is obtained at $1.68 \times 10^{-10} \text{m}^3/\text{s}$. In comparison with the DEM prediction of Zone 2, i.e, $1.72 \times 10^{-10} \text{m}^3/\text{s}$, it is concluded that the DEM simulation model can be used to predict the sliding wear by iron ore bulk solids.

6.4 Abrasive wear prediction of bionic surfaces

To predict wear reduction of the bionic surface chute, this section firstly presents the determination of the geometrical parameters of the bionic model for abrasive wear reduction. Then the wear of a base case of a bionic surface is predicted and is compared to that of a smooth surface. Furthermore, the sensitivities of geometrical parameters on abrasive wear are investigated.

6.4.1 Geometrical parameters of the bionic model

Figure 6.5(a) illustrates the geometrical parameters of the bionic model (chapter 3). The values for the geometrical parameters of the bionic model are determined in the following way:

For the geometrical parameters a_0 and b_0 on the semi-ellipsoidal convex, it is known that $a_0 \geq b_0$ so that particles can be transfered by the curved chute. The parameter b_0 can be determined based on the condition that the height of the convex is not larger than particle diameter to enable particle to roll (i.e, $b_0 < d_{50} = 3.0$ mm) [7]. Considering that a smaller convex causes more meshes and the meshing and simulation time is proportional to the number of meshes, the minimum size of b_0 is selected at 1.5 mm.

The geometrical parameters c_0 and d_0 are based on the fact that less wear is predicted when the distance between adjacent convexes is larger than the width of convexes [11]. Thus c_0 and d_0 are bigger than a_0. However, the used distances of c_0 and d_0 are much larger. In this manner, the meshing time and simulation time is reduced as a result of decreasing mesh number by decreasing the number of convexes. Table 6.9 lists the values for the geometrical parameters $a_0 - d_0$ for the bionic model of the chute.
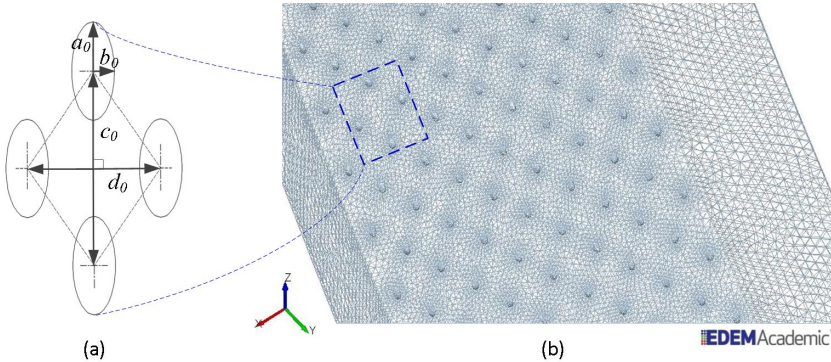
Figure 6.5: Bionic design of non-smooth surface (a) geometrical parameters (b) meshed geometry of the base case of bionic surfaces (**group 2**)

Table 6.9: Geometrical parameters of the bionic model

Geometrical parameters	group 1	**group 2**	group 3	group 4
major radius a_0 [mm]	2	**3**	4	5
minor radius b_0 [mm]	1.5	**2**	2.5	3
vertical distance c_0 [mm]	30	**40**	50	60
horizontal distance d_0 [mm]	25	**30**	35	40

In Table 6.9, group 2 is selected as a base case and the corresponding bionic surface is shown in Figure 6.5b. Other values are used to investigate the sensitivity of corresponding parameters (section 6.4.3).

6.4.2   Wear comparison for a bionic surface and a smooth surface

Figure 6.6 shows the wear prediction of the bionic surface for the base case (group 2 of Table 6.9). It can be seen that the bionic surface also has the same wear zones 1-3 as that of the smooth surface (Figure 6.4). In addition, it is observed that more wear occurs to semi-ellipsoidal convexes than to the matrix of bottom surface.

To compare the wear rates for the smooth and the bionic surfaces, the total wear volumes of the whole chute with respect to time are presented in Figure 6.7. It shows that the both bionic surface and smooth surface initially undergo curve increase and quickly reach linear increase. The bionic surface produces lower wear volumes than the smooth one for transport period (0 - 4s). By comparing the

rates of mass flow at chute outlets, it demonstrates that the transport capability for the bionic surface can be maintained at the steady state (Figure 6.8). The difference of the transport capacity at the initial time (start-up phenomenon) is due to the that effect of bionic convexes, which is illustrated by Figures 6.9 and 6.10.
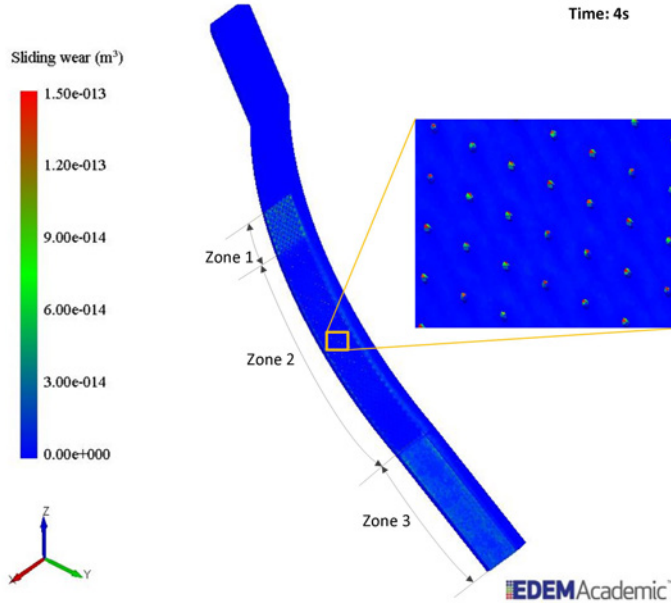
Figure 6.6: Wear prediction for the base case of a bionic surface (**group 2**)
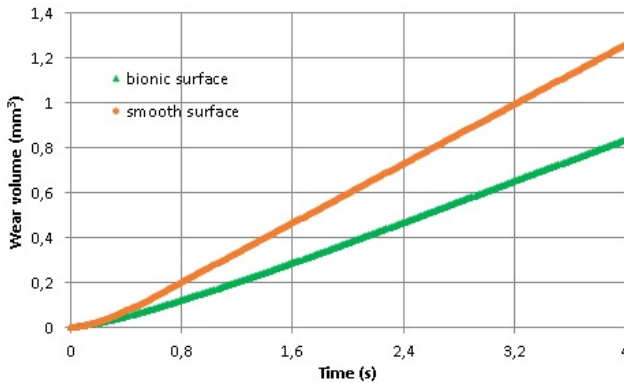
Figure 6.7: Wear volumes for the smooth and bionic surfaces (**group 2**)

The reduction of wear can be quantified by Equation 6.4:

$$W_r = \frac{W_{V,s} - W_{V,b}}{W_{V,s}} \times 100\% \tag{6.4}$$

in which W_r is designated as the ratio of wear reduction; $W_{V,s}$ and $W_{V,b}$ are wear volumes with respect to smooth surface and bionic surface. By using their wear volumes from 1.6 s to 2.4 s, the ratio of wear reduction is calculated at 30.7%.
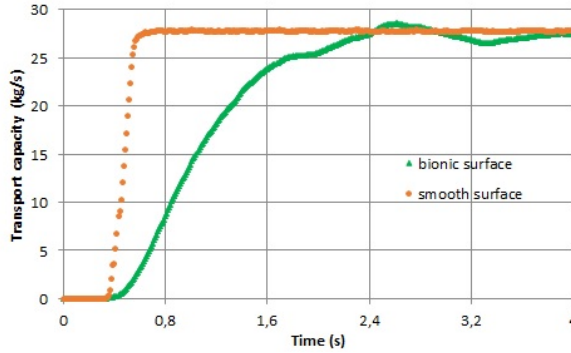
Figure 6.8: Transport capabilities for the smooth and bionic surfaces (**group 2**)

To understand the wear reduction mechanism using bionic surface, the particle velocity distributions from chute bottom view are compared in Figure 6.9. It shows that the overall velocity of bulk solids for the bionic surface is lower than that of the smooth one. However, the thickness of bulk solids on the bionic surface is larger, which is shown by the sectional middle view in Figure 6.10. It indicates that a certain amount of particles suspend above the chute channel, which is ascribed to the fact that semi-ellipsoidal convexes changing particle sliding motions.
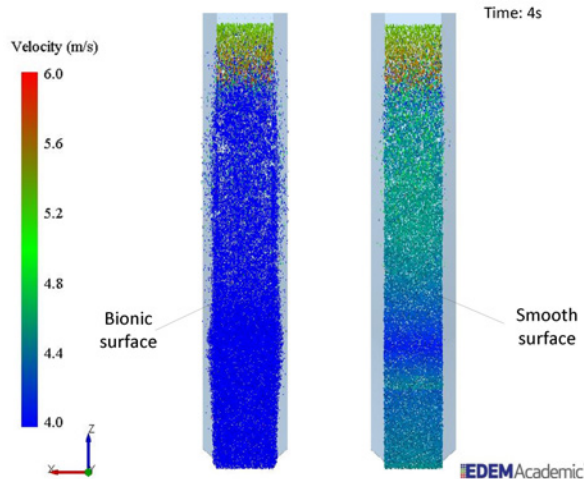
Figure 6.9: Bottom view of velocities for bionic and smooth surfaces (**group 2**)

In addition, the contact pressure on these two chutes is compared in Figure 6.11. It shows that the pressure on the bionic surface is less sever than on the smooth surface. Due to the fact that a bionic surface can influence the direction of motion of bulk solids, the resultant pressure on the straight outlet area is higher than that

on the resultant pressure on the outlet area of the smooth surface. The predictions of pressure are consistent with the wear predictions of bionic surface (Figure 6.6) and smooth surface (Figure 6.4).
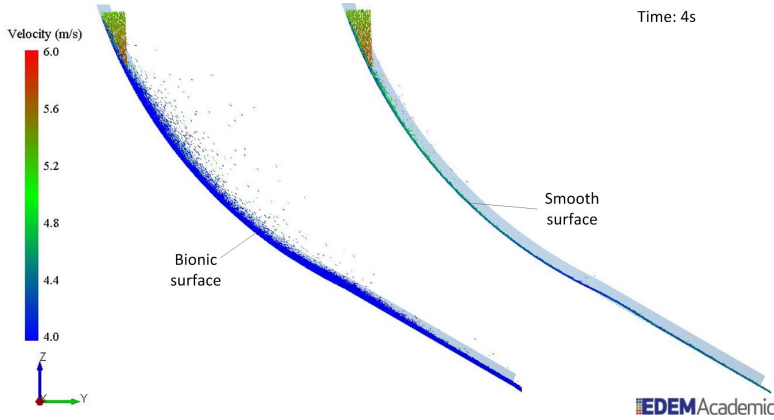
Figure 6.10: Sectional view of particle velocities for bionic and smooth surfaces (**group 2**)
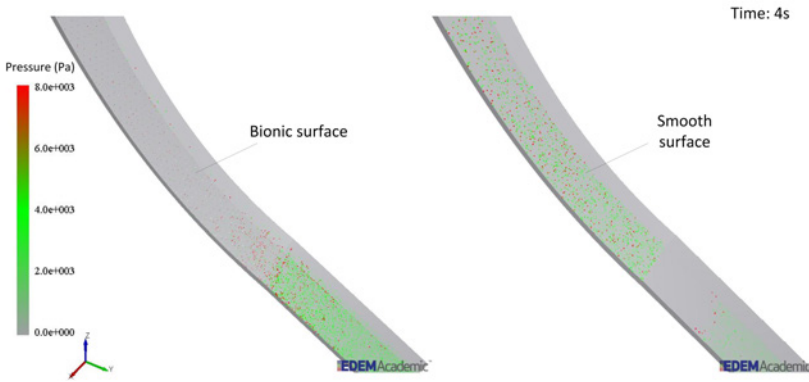
Figure 6.11: Contact pressure for the bionic and smooth surface (**group 2**)

Therefore, the wear reduction mechanism is explained by the following: the semi-ellipsoidal convexes increase the directionality of transported particles with respect to equipment surface. This breaks the continuity of the sliding bulk solids [170], consequently the contact pressure between bulk solids and chute surface is reduced so that wear is reduced. Although a bionic surface causes certain particles to travel off the chute channel, in practice the occurrence is not significant because in practice the transport capacity is much larger such that the simulated scenario and thus particles can hardly move off the chute bottom.

6.4.3   Sensitivity study of geometrical parameters

The previous section has demonstrated the abrasive wear reduction of a bionic surface with wear prediction of a smooth surface. In order to investigate the impact of the bionic surface subject to the variation of geometrical parameters $(a_0 - d_0)$, a sensitivity study has been performed. The figures 6.12-6.15 present the wear volumes of bionic surfaces subjected to the four geometrical parameters a_0-b_0. In each figure, the wear of a smooth surface is also incorporated for reference purpose. The parameters used in the sensitivity analysis are all given in Table 6.9. Different geometrical parameters have different effects on the wear predictions, which are illustrated below.

Figure 6.12 illustrates the wear volumes of the four bionic surfaces subjected to four major radii. It is observed that wear volume increases with increasing major radius a_0. (The parameters b_0, c_0 and d_0 are denoted in group 2.) In particular, a significant increase occurs when increasing a_0 =2 mm to 3 mm. However, the increase in wear volume becomes minor for a_0 >3 mm. The reason for this is that the contact directionality of a_0 =2 mm the convexes are hemispherical, giving maximum contact directionality and thus can maximally enable the reduction of wear [11]. With increasing a_0, the convexes become ellipsoidal and less sensitive. For a_0 =2 mm, the highest ratio of wear reduction is calculated at 43%.
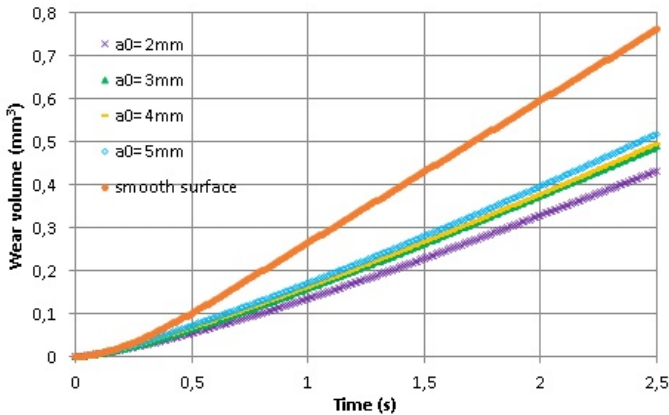
Figure 6.12: Wear volume as a function of major radius a_0

Figure 6.13 presents the wear volumes for the four bionic surfaces with respect to four minor radii. It shows that with increasing the minor radius, a steady and significant wear reduction is obtained. The reason is that with increasing the minor radius, the shape of a semi-ellipsoidal convex tends to change to semi-hemispherical (i.e. $a_0/b_0 = 1$). This change is beneficial to the increase of contact as the cases for the minimum wear of the major radius a_0=2 mm. Thus the highest wear reduction is obtained at 63% for $b_0 = 3$ mm. The results have consistencies with the research of applying spherical convexes for reducing soil resistance [97].

Figure 6.14 shows the wear volumes for the bionic surfaces of four vertical distances. In this figure, a minor increase of wear is observed with increasing vertical

distance c_0 from 30 to 60 mm. The reason is that when the vertical distance c_0 is much larger than the particle size (i.e. $c_0 > 3d_p$), more wear is predicted with increasing vertical distance. However, the influences of semi-ellipsoidal convexes are insignificant [7]. For $c_0 =$30 mm, the highest ratio of wear reduction is calculated at 37%.
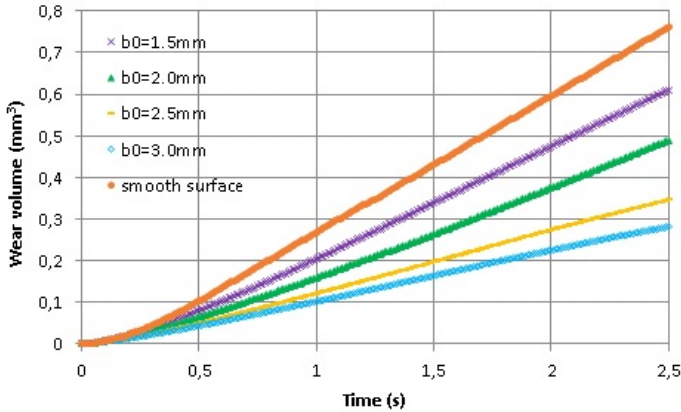
Figure 6.13: Wear volume as a function of minor radius b_0
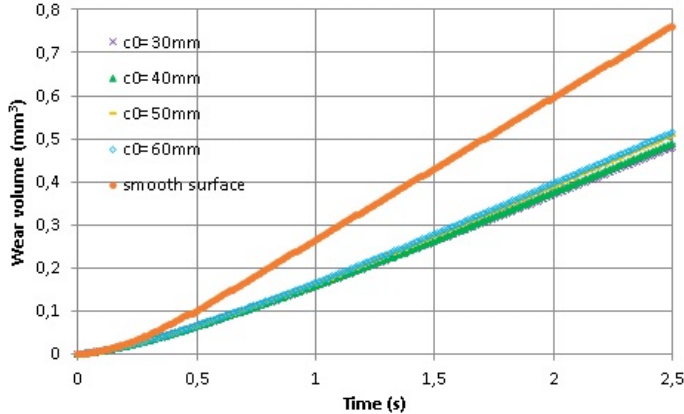
Figure 6.14: Wear volume as a function of vertical distance c_0

Figure 6.15 provides the wear volumes with respect to the horizontal distance d_0 of four bionic surfaces. It is seen that the wear volume increases with increasing horizontal distance d_0. The reason is similar to the wear results while increasing the vertical distance c_0. Thus it can be concluded that when the horizontal distance $d_0 > 3d_p$, the larger the d_0, the smaller the contact directionality. In addition, it is observed that for $d_0 > 3d_p$, the larger the d_0, the faster the increase of wear volume is apparent due to the faster decrease of contact directionality. For $d_0 =$25 mm, the highest ratio of wear reduction is calculated at 38%.
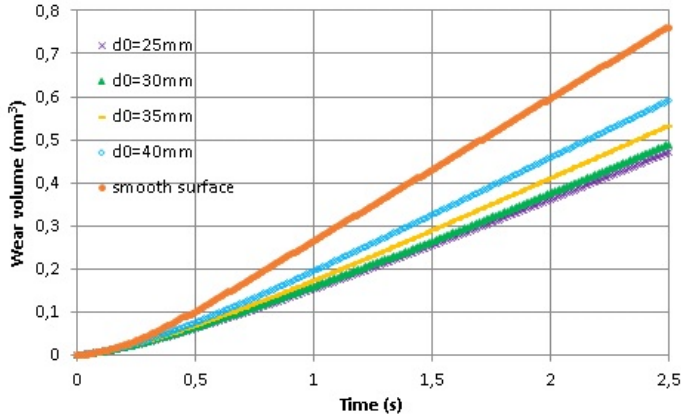
Figure 6.15: Wear volume as a function of transverse distance d_0

In summary, it is shown that the wear volumes of all bionic surfaces are lower than the wear volume obtained with a smooth surface at all values of the determined geometrical parameters. The highest reduction occurs at the longer hemispheric radius of 3mm, with a reduction of 63%.

6.5 Conclusions

To answer the subquestion of " *What are the effects of applying bionic surfaces on abrasive wear reduction?* ", this chapter has demonstrated the abrasive wear reduction of bulk solids handling equipment by using bionic design. Four conclusions are drawn follow.

(1) Using the values determined from experimental tests, the steady state of the sliding wear in iron ore handling is accurately predicted.

(2) In comparison with a conventional smooth surface, the wear reduction of a bionic surface is successfully demonstrated.

(3) The effects of geometrical parameters on the wear prediction of bionic surface are obtained. It is shown that the maximum reduction of wear achieved is 63% from hemispheric convexes of a bionic surface.

(4) This research provides significant value for applying bionic design method to reduce abrasive wear in bulk solids handling.

This chapter investigated the abrasive wear reduction using the bionic design method. In parallel with the investigation on abrasive wear reduction, the erosive wear reduction will be explored in the next chapter.

7 | CHAPTER

Erosive wear reduction of bulk solids handling equipment surfaces

Chapter 6 demonstrated that the abrasive wear of bulk solids handling equipment surface can be successfully reduced using a bionic design method. To apply the bionic design method for erosive wear reduction, the wear for a conventional smooth surface and bionic surfaces will be investigated.

This chapter presents the investigation of the erosive wear reduction of bulk solids handling equipment by applying a bionic model. This chapter is organized into four sections. Section 7.1 illustrates the reference case for erosive wear modeling; section 7.2 provides the erosive wear prediction of a smooth surface; section 7.3 presents the erosive wear predictions of bionic surfaces. Finally, conclusions are given in section 7.4.

7.1   Referential setup for modeling erosive wear

As was introduced in chapter 2, the erosive wear of an impact chute (or a hood) (Figure 2.20) is a significant issue at a bulk transfer station. To reduce the erosive wear on an impact chute surface, an analysis will be made into the applicability of an impact chute with a bionic design. This analysis will be made using a DEM model. First, a referential setup is determined for the DEM simulations. Table 7.1 lists the corresponding dimension and positions.

Table 7.1: Referential dimensions and positions of an impact chute based on [4]

Denotations	b_2	B_3	e_1	e_2	e_3	h_5	r_2	R_2
Values (m)	0.15	0.1	0.13	0.45	1.42	0.06	0.6	2.8
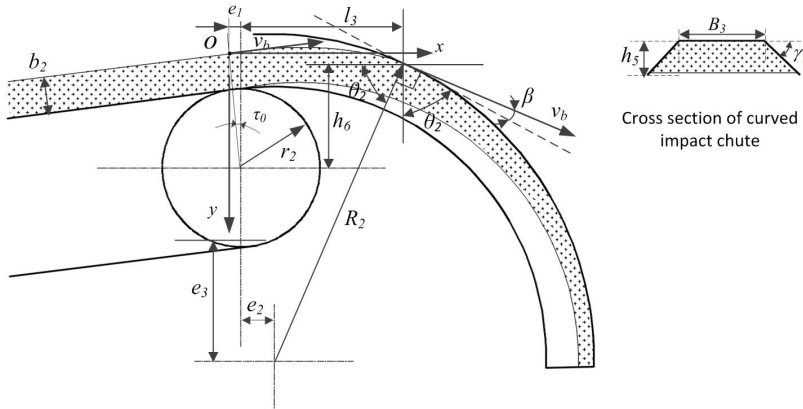
Figure 2.20: Erosive wear on a curved impact chute [4]

In addition to the selected dimensions and positions, the applied conveyor speed is 5.5m/s by referring to bulk solids handling conditions [4]. The inclination angle at discharging point can be determined as $\tau_0 = 10^o$ [4]. The modeled chamfer angle between the bottom and a joining side can be $\gamma_2 = 45^o$.

7.2   Erosive wear prediction of a smooth surface

Using the same approach to quantify impact wear by a single particle (Chapter 5), the erosive wear by bulk solids is also investigated from cumulative cutting and cumulative deformation energy. This section presents the erosive wear prediction of a smooth surface of the curved impact chute. To verify the DEM prediction, theoretical calculation is also presented.

7.2.1   Simulation model

The values of the DEM parameters for simulating erosive wear are mainly from Table 6.8, which were used for modeling abrasive wear. However, to mesh the small sizes of convex spikes, the mesh size must be reduced. In this simulation model, the maximum mesh size is set at 2.0×10^{-3} m, because reducing it further is difficult by considering the meshing time. Using this setting, the shapes of meshed convex spikes are pyramidal. The time step is set 1.0×10^{-6}s similar to what was used for particle impact wear. The width of particle factory is equal to the chute bottom width, which is 0.1 m.

In addition, to efficiently investigate the erosive wear using EDEM® 2.7.1 [149], the particle factory is placed closely to the impact area of chute surface. Accordingly, the velocities of particles are adjusted using Equation 2.49 (Figure 2.20). Table 7.2 presents the determined values for the parameters used for modeling erosive wear.

Table 7.2: Values for modeling erosive wear on a curved impact chute

Categories	Wear aspects	DEM parameters	Values
Particle	iron ore	radius r_p [$\times 10^{-3}$m]	1.5 – 4
		density ρ_p[kg/m^3]	4865
		Poisson ratio ν_p [–]	0.24
		shear modulus G_p [GPa]	65
Geometry	chute	density ρ_g[kg/m^3]	7932
		Poisson ratio ν_g [–]	0.3
		shear modulus G_p [GPa]	78
		maximum mesh size d_g [$\times 10^{-3}$m]	2.0
Contact	iron ore/iron ore	coefficient of restitution e [–]	0.45
		coefficient of static friction μ_{st} [–]	0.41
		coefficient of rolling friction μ_r [–]	0.22
	iron ore/chute	coefficient of restitution e [–]	0.4
		coefficient of static friction μ_{st} [–]	0.46
		coefficient of rolling friction μ_r [–]	0.3
Simulation	conditions	particle generation rate q_b [kg/s]	27.78
		initial horizontal velocity v_y [m/s]	4.92
		initial vertical velocity v_z [m/s]	1.40
		total time t [s]	1.5
		time step Δt [$\times 10^{-6}$s]	1.0

Using the geometrical settings in Table 7.1 and the DEM values in Table 7.2, the simulation model for predicting erosive wear on the curved impact chute is built in the software EDEM$^{\circledR}$ 2.7.1 [149], which is depicted in Figure 7.1. It also outlines the main impact wear area as predicted by the analytical model (Figure 2.20).
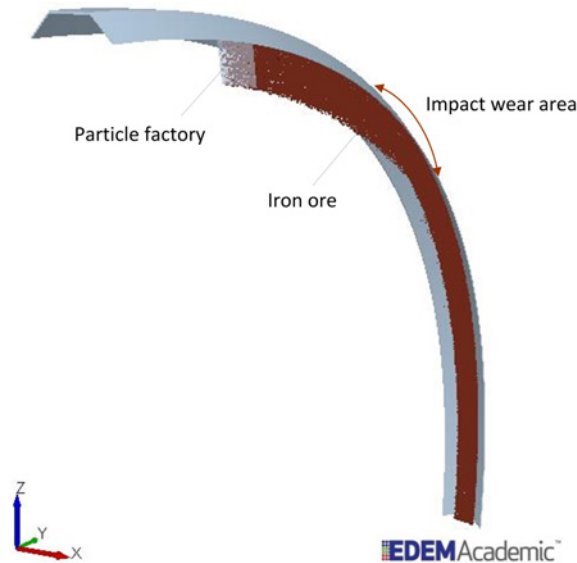
Figure 7.1: Simulation model for predicting erosive wear

7.2.2   Results

From the analytical model given in Figure 2.20, it shows that the impact angle β is very low. Therefore, the cutting wear is dominant over deformation according to [56, 57]. Figure 7.2 presents the cumulative cutting energy on the curved impact for the simulation of Figure 7.1. It also illustrates the wear distribution of the impact area. The legend denotes the scale of wear energy for individual meshes.
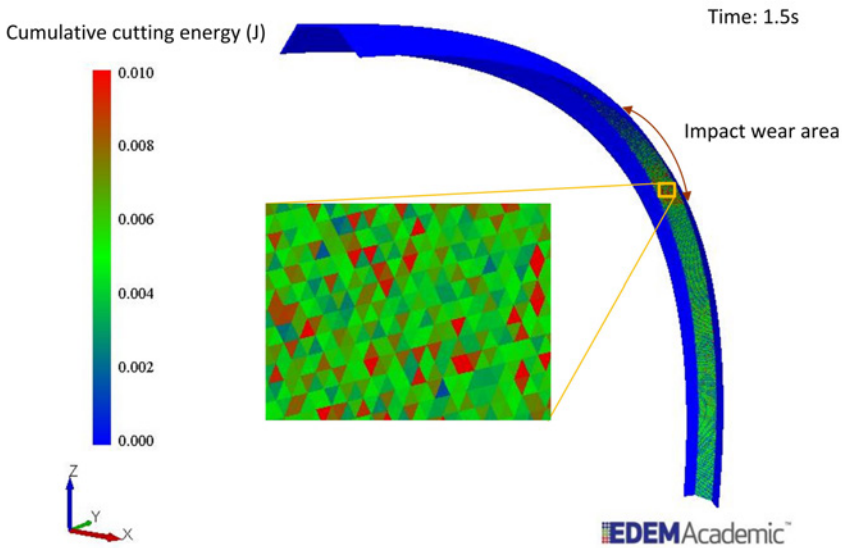
Figure 7.2: Total cutting energy on the smooth surface

The predicted data of the total normal force and the total tangential force on the impact area are given in Figure 7.3. It can be seen that the tangential force is influenced by the deformation force, which is as expected in accordance with Equation 5.5. The reason for the fluctuations for both forces is that unequal mass of particles made impact on the chute surface at given instant. Nevertheless, the fluctuations desegregate and the majority data reach relatively stable levels as the expected transport capacity is arrived (after 0.9 s). The average normal force and tangential force are 30 N and 14 N for the period 0.9-1.5 s. It is also noticed an unexpected occurrence of a quite high normal force between 1.2 s and 1.5 s, which may be triggered by the maximum flow rate of the bulk solids.

7.2.3   Theoretical calculation

To evaluate the reliability of the predicted tangential and normal force (Figure 7.3), theoretical calculations will be carried out. The total impact force exerted by bulk solids can be approximated by using the impulse-momentum theory given in Equation 7.1 [136],

$$\sum \boldsymbol{F} = q_b(\boldsymbol{v}_{b,0} - \boldsymbol{v}_{b,1}) \tag{7.1}$$

where q_b is the mass flow rate of bulk solids; $\boldsymbol{v}_{b,0}$ and $\boldsymbol{v}_{b,1}$ are the velocities of bulk solids before and after impact.
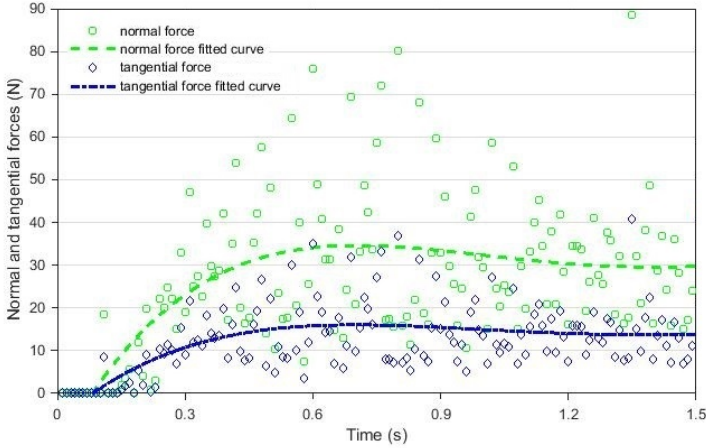
Figure 7.3: DEM prediction of the total tangential and normal forces on the smooth surface

Based on Equation 7.1, the average normal force F_N triggered by bulk solids can be obtained by,

$$F_N = q_b(v_{b,0,n} + v_{b,1,n}) = q_b v_{b,1,0} \sin \beta (1 + e) \tag{7.2}$$

Correspondingly, the average tangential force F_T is given by,

$$F_T = \mu_{st} F_N \tag{7.3}$$

Using Equations 2.51 and 2.52, the impact angle β can be found to be 8.71^o. In combination with the values in Table 7.2, the average normal force and the average tangential forces are calculated and are respectively 37 N and 17 N using Equations 7.2 and 7.3. By comparison, the DEM predicted values (30 N and 14 N) are respectively 18% lower. This may be partially ascribed to the limitation of using the Hertz-Mindlin no-slip contact model to predict particle impact, which was discussed in chapter 5. Another possible explanation is that while particles are in contact with chute surface during impact, the succeeding impact can occur to particles instead of chute surface, and thus decreasing impact forces. By this, it is concluded that quantitative prediction of erosive wear can be achieved.

7.3   Erosive wear prediction of bionic surfaces

Using this simulation model which was verified in section 7.2, the erosive wear of a bionic surface of the curved chute can also be predicted. In this section, the values of geometrical parameters of the a bionic model are determined. Then the wear prediction of a bionic surface is compared with that of the smooth one. Furthermore, a sensitivity study on geometrical parameters of the bionic model is carried out.

7.3.1   Geometrical parameters of the bionic model

To achieve erosive wear reduction on the curved chute surface, the proposed bionic model of chapter 3 will be applied on the impact wear area. Based on the illustration of the biological morphology for erosive wear reduction (Figure 3.17), the values for the geometrical parameters $(e_0 - j_0)$ (Figure 7.4a) are determined as below.
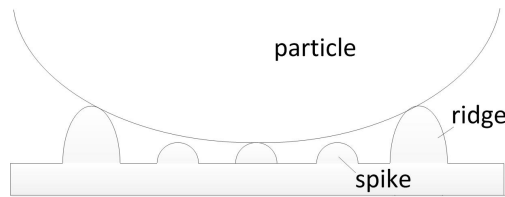
Figure 3.17: Wear reduction by reducing contact friction based on [94]

For the radii of spikes e_0, the minimum size is determined at 1.25 mm. Because using a smaller value requires too much computational time (in meshing and simulation) due to largely increased number of geometry meshes. However, it is noted again using the determined sizes, the meshed convex spikes are pyramidal as a result of the determined maximum mesh size (i.e, 2.0 mm). To enable particle rolling [7] after impact, the maximum size of spike radius can be set by 2.0 mm, which is lower than the median size (i.e, d_{50} = 3.0 mm) of the used bulk solids. To reduce contact friction by increasing the chances of particle impact on convex spikes instead of on smooth area (Table 3.1), the maximum horizontal and vertical distances between adjacent spikes (i.e, f_0 and g_0) are limited by particle sizes.

The determination of the distance between ridges h_0 can be referred to Figure 3.17, in which it shows that the distance is less than a particle diameter. However, for the erosive wear subjected to low impact angles, this distance can be increased while ridges can still effectively resist impact force. In this manner, the number of spikes and ridges can be reduced and thus the computational time is reduced. For the dimensions of the ridges (i_0 and j_0), their height i_0 must be larger than the spike radius in order to prevent large impact forces acting on spikes. On the other hand, the maximum size is evaluated based on the fact that particles should be able to efficiently travel through the chute channel. Table 7.3 lists the values for the geometrical parameters $e_0 - j_0$.
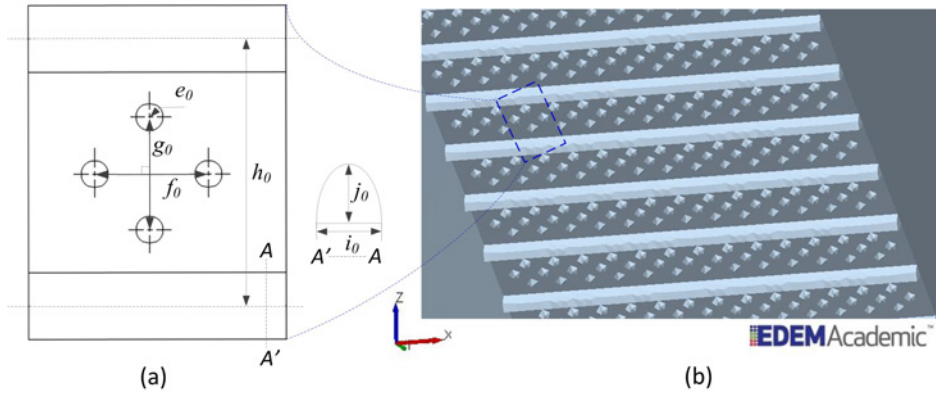
Figure 7.4: A bionic surface of a curved chute bottom (a) geometrical parameters (b) bionic design on the bottom surface (**group 2**)

Table 7.3: Parametric variation for erosive wear prediction of bionic surfaces

Geometrical parameters	group 1	**group 2**	group 3	group 4
spike radius e_0 [mm]	1.25	**1.5**	1.75	2.0
spike/spike horizontal distance f_0 [mm]	6.0	**7.0**	8.0	9.0
spike/spike vertical distance g_0 [mm]	6.0	**7.0**	8.0	9.0
ridge/ridge distance h_0 [mm]	16	**18**	20	22
ridge width i_0 [mm]	3.0	**3.5**	4.0	4.5
ridge height j_0 [mm]	3.0	**3.5**	4.0	4.5

7.3.2 Wear comparison for a bionic surface and a smooth surface

To compare wear from a bionic surface to that of a smooth surface, group 2 of Table 7.3, is selected as a base case. The corresponding bionic surface is shown in Figure 7.4b. The predicted cumulative cutting energy on the bionic surface is shown in Figure 7.5. It is seen that the ridges suffer more from severe wear than the convex spikes between the ridges. This is because for the set of values (group 2) the majority impact occurs to ridges subjected to the low impact angle.

To compare wear of a chute with a bionic surface with a chute with a smooth surface, Figure 7.6 presents the cumulative cutting and cumulative deformation energy for the bionic and the smooth surfaces. It can be seen that the cutting energy and deformation for both smooth and bionic surfaces maintain a linear increase after 0.9 s. This means that the steady state of the transport as well as the wear of bottom chute surface is reached. Furthermore, Figure 7.6 illustrates that the cumulative cutting energy is reduced by the bionic surface. However, the cumulative deformation energy goes up.
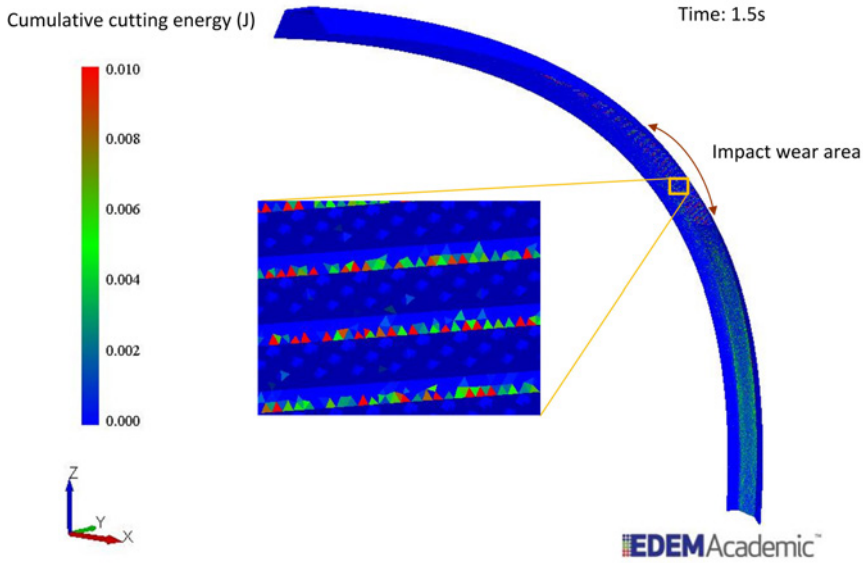
Figure 7.5: Tangential impact energy distribution on the bionic surface **group 2**
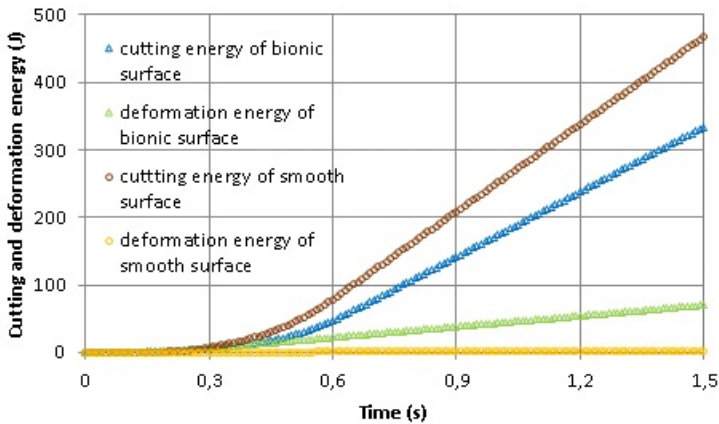
Figure 7.6: Comparison of cumulative cutting and deformation energy (**group 2**)

To evaluate wear volume, Equation 5.18 is used to quantify erosive wear volume.

$$W_{V,e} = \frac{E_{k,c}}{\varepsilon_c} + \frac{E_{k,d}}{\varepsilon_d} \tag{5.18}$$

in which ε_c and ε_d are respectively cutting and deformation factors. The accurate values for these two factors have to be determined by conducting wear tests [64]. However, to estimate the reduction of wear for the bionic surface, a coefficient Λ is introduced to relate ε_c with ε_d, i.e,

$$\varepsilon_c = \Lambda \varepsilon_d \tag{7.4}$$

According to the research of erosive wear of metallic materials, the values of Λ is between 1/4 to 4/4 [64]. Figure 7.7 presents the ratio for the reduction wear by using the bionic surface (group 2) using Equation 6.4. It is seen that wear reduction can be achieved from 25% to 14% corresponding to Λ from 1/4 to 4/4.
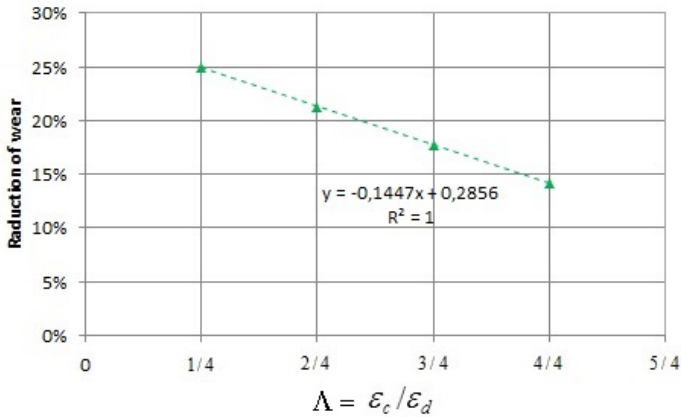
Figure 7.7: Ratio of reduction of wear for the bionic surface as a function of Λ (**group 2**)

In order to estimate the absolute wear volume, the wear factors for mild steel surface with respect to Sishen iron ore particles are referred to the combination of mild steel surface and ilmenite bulk solids [64]. This is based on the fact that ilmenite bulk solids probably have similar particle hardness, particle size range and irregularities of shapes. Thus the measured values for the combination of mild steel surface and ilmenite bulk solids $\varepsilon_c = 1.3 \times 10^7$ J/kg and $\varepsilon_d = 2.8 \times 10^7$ J/kg (and thus Λ = 0.46) are applied for this research. Figure 7.8 presents the wear volumes for the bionic and smooth surfaces obtained by using Equation 5.18. It can be seen from Figure 7.8 that wear reduction can be achieved by using bionic surface. For the steady transport state (after 0.9 s), wear reduction is calculated at 22% (Equation 6.4).

In order to understand the wear reduction mechanism, Figure 7.9 presents the sectional middle view of bulk solids velocities for the bionic surface and smooth surface. It can be seen that certain particles travel off the main flow stream from the bionic surface chute. To be able to more clearly observe the deviated particles, the velocities of the particles at the interacting layer relative to equipment surface are shown in Figure 7.10. It can be seen that a number of particles in the interacting layer of the bionic surface have lower velocities and random directions. By comparison, the particles on the smooth surface have higher velocities and the directions are uniform.
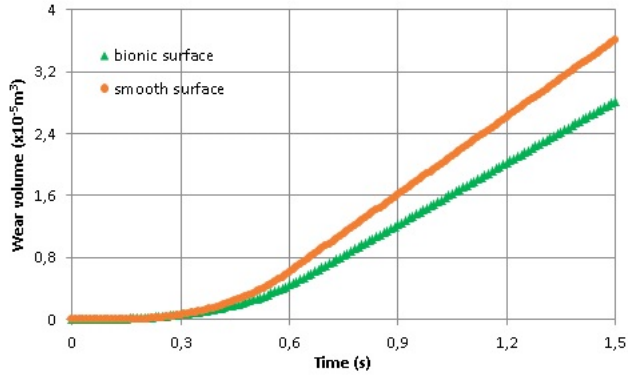
Figure 7.8: Wear volumes for the bionic and smooth surfaces (**group 2**)
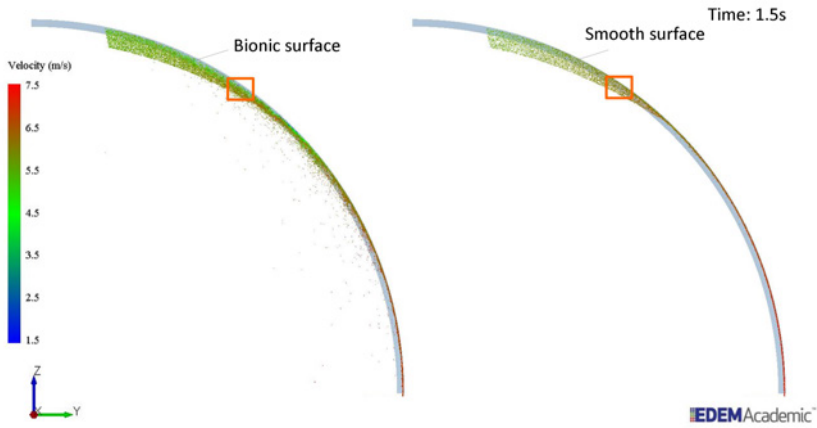
Figure 7.9: Particle velocities on the bionic surface (**group 2**) and smooth surface
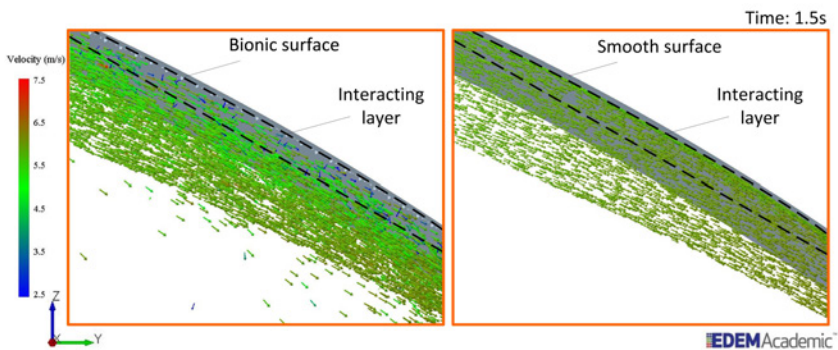
Figure 7.10: Particle velocities of the interaction layers on the bionic surface (**group 2**) and smooth surface

Figures 7.9 and 7.10 imply that bionic surfaces cause trajectories of certain particles to deviate off the main bulk flow. This slightly lowers the transport capacity of the bionic surface chute in comparison with to the smooth surface chute, which is seen in Figure 7.11. However, the deviated particles can fall onto hood of the transfer based on the setup in Figure 2.19 , thus the transport capacity can still be maintained.
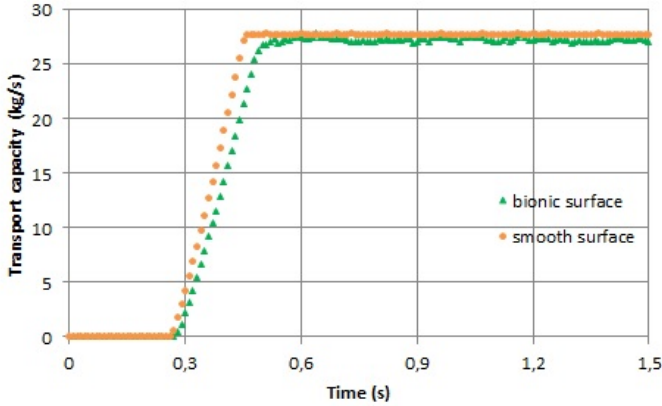
Figure 7.11: Comparison of transport capacity for the bionic surface (**group 2**) and smooth surface

Therefore the wear reduction mechanism maybe interpreted as: the ridges and spikes on the bionic surface enable random direction of particles after impact. As a result, the random direction of particles promote more impact relative to successive particles and thus the kinetic energy of bulk solids is reduced. This confirms the prediction of particle behavior as shown in Figure 3.18.

Up to now, the wear reduction by a bionic surface is demonstrated. To assess the effects of geometrical parameters on wear volume, the sensitivity of geometrical parameters on wear of bionic surfaces is studied as below.

7.3.3   Sensitivity study of geometrical parameters

To carry out a sensitivity study of the six parameters in Table 7.3, the parameters of group 2 are used as reference case. For each parameter, three other simulations are done by using the values in group 2 with that from the groups 1, 3 and 4. The wear energy for each simulation is calculated. The absolute wear volumes can be estimated by applying wear factors $\varepsilon_c = 1.3 \times 10^7$ J/kg and $\varepsilon_d = 2.8 \times 10^7$ J/kg (Λ = 0.46).

It is examined that all six parameters enable a reduction of the cutting energy but cause an increase of the deformation energy. For the first three parameters: namely, spike radius (e_0), the horizontal and vertical distances between spikes (f_0 and g_0), the effect on cumulative cutting or the cumulative deformation energy is negligible. This is due to the fact that the greatest chances of wear occur

through ridges instead of spikes within the varied values of spike parameters. Thus the wear energy and volumes for the three parameters can also be illustrated by Figures 7.6 and 7.8. However, the other three parameters (h_0, i_0 and j_0) have influences on cumulative cutting and cumulative deformation energy, which are respectively illustrated in the following paragraphs.

Figure 7.12 shows the cumulative cutting energy with respect to the ridge/ridge distance h_0 of a bionic surface and a smooth surface. It can be seen that with increasing ridge/ridge distance h_0 from 16 to 18 mm, the cumulative cutting energy undergoes a minor decrease. This is ascribed to the increasing ridge/ridge distance that allows more particles to impact on spikes which may introduce more deformation energy [94]. Because the total kinetic energy of bulk solids is constant, the cumulative cutting energy on the chute surface is reduced. However, from 18 to 22 mm, the interaction between bulk solids and bionic surface maintains a stable state. The reason is suggested to be that there is no more increase of particles impact on the spikes, and thus the cutting energy remains the same.
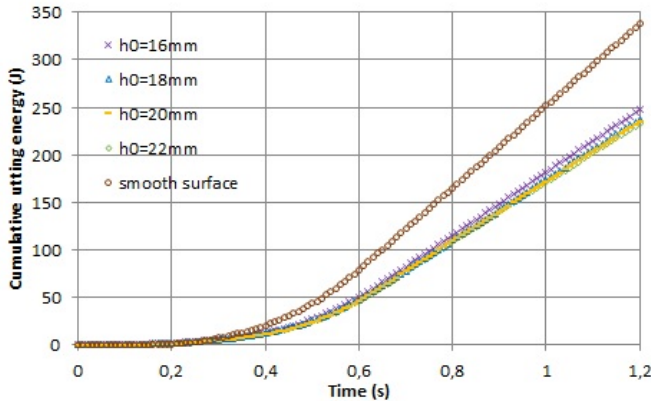
Figure 7.12: Cumulative cutting energy with respect to ridge/ridge distance h_0 of bionic surfaces and a smooth surface

Figure 7.13 shows the cumulative deformation energy with respect to the ridge/ridge distance h_0 of a bionic surface and a smooth surface. It can be seen that the cumulative deformation energy experiences an increase with increasing ridge/ridge distance h_0 from 16 to 18 mm. This is because more particles impact on the convex spikes when the ridge/ridge distance is larger. Similar to the character of the cumulative cutting energy (Figure 7.12), the cumulative deformation energy remains constant when changing the distance from 18 and 22 mm.

Using Equation 5.18, the calculated wear volumes for the variation of ridge/ridge distance h_0 is given in Figure 7.14. It infers that with increasing the distance for ridge/ridge, a slight reduction of wear can be achieved. The minimum wear volume is obtained at h_0 = 18, 20 or 22 mm, which is 1.99 $\times 10^{-5}$ m^3. By using Equation 6.4, the corresponding ratio of wear reduction is calculated at 24%.
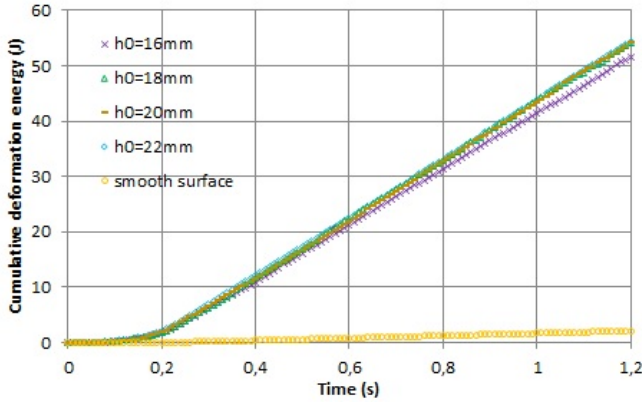
Figure 7.13: Cumulative deformation energy with respect to ridge/ridge distance h_0 of bionic surfaces and a smooth surface
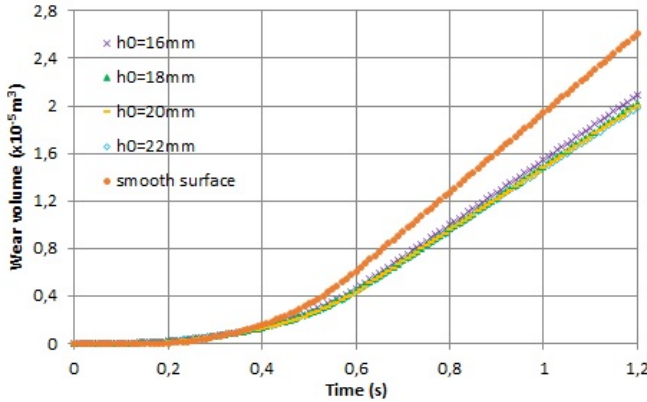
Figure 7.14: Wear volumes as functions of ridge/ridge distance h_0 of bionic surfaces and a smooth surface

Figures 7.15 illustrates the cumulative cutting energy with respect to the ridge width of a bionic surface and a smooth surface. It can be seen that the cumulative cutting energy increases with the increase of ridge width. This is due to the fact that with increasing width of the ridges, particle impact angle is reduced as is illustrated in Figure 7.16, i.e, from $i_0 = 3.0$ to 4.5 mm, the impact angle β increases. As a result of the decrease of impact angle, the cumulative cutting energy increases according to the result shown in Figure 5.31.

Figure 7.17 presents the cumulative deformation energy with respect to the ridge width of a bionic surface and a smooth surface. It can be observed that the cumulative deformation energy reduces with the increase of ridge width. This is due to the fact that the total kinetic energy is constant, thus when the tangential velocity is increased, the normal velocity will be reduced.
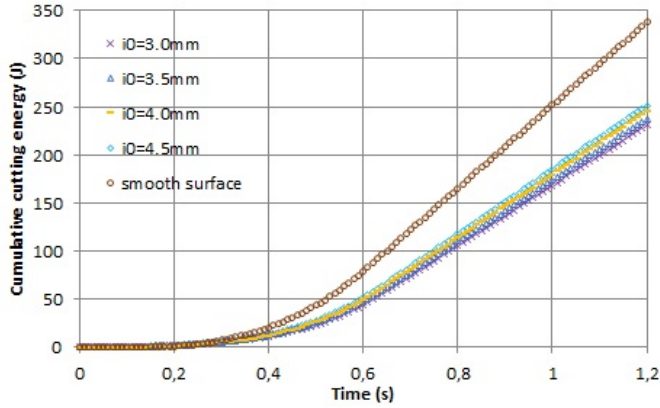
Figure 7.15: Cumulative cutting energy with respect to ridge width i_0 and a smooth surface
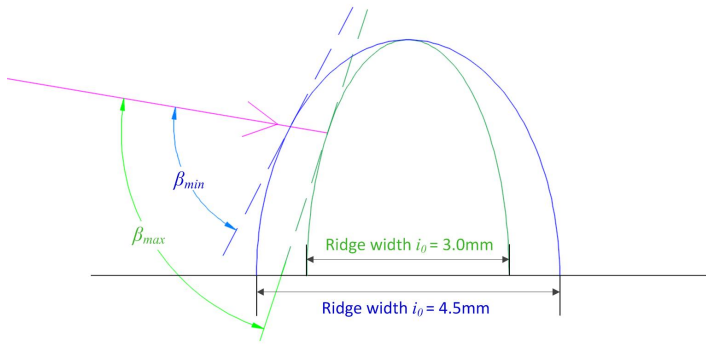
Figure 7.16: Variation of impact angle by increasing ridge width i_0
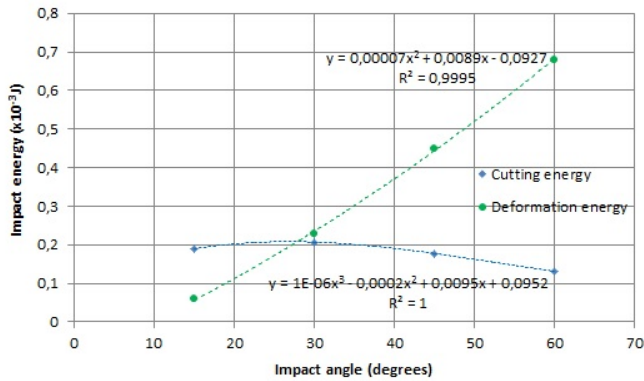
Figure 5.31: Impact wear energy as a function of impact angle

Using Equation 5.18, the calculated wear volumes with respect to ridge width are plotted in Figure 7.18. It shows that the least wear is achieved at the smallest ridge width, i_0 = 3.0 mm. The corresponding volume is 1.98 $\times 10^{-5}$ m^3 and promotes the ratio of wear reduction also at 24%.
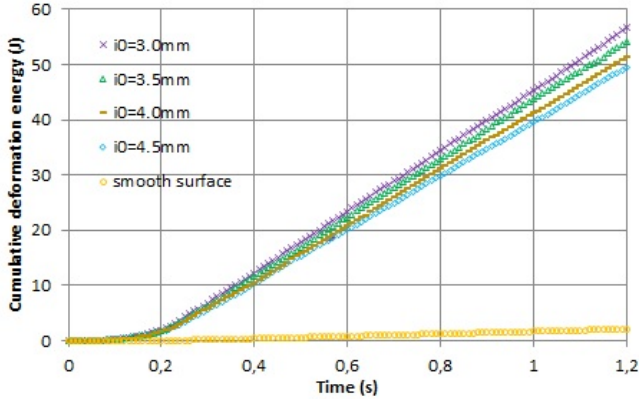
Figure 7.17: Cumulative deformation energy with respect to ridge width i_0 and a smooth surface
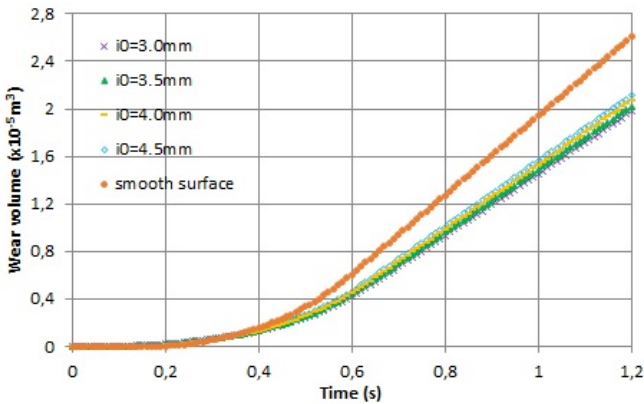
Figure 7.18: Wear volumes as functions of ridge width i_0 of bionic surfaces and a smooth surface

Figure 7.19 presents the cumulative cutting energy with respect to ridge height of the bionic surfaces and a smooth surface. It is seen that the cumulative cutting energy decreases slightly with increasing ridge height. This can be ascribed to the fact that when increasing the ridge height, the impact angle also increases, as shown in Figure 7.20, i.e, from i_0= 3.0 to 4.5 mm, the impact angle β increases. As a result, the cumulative cutting energy decreases. This result can be also observed in Figure 5.31.
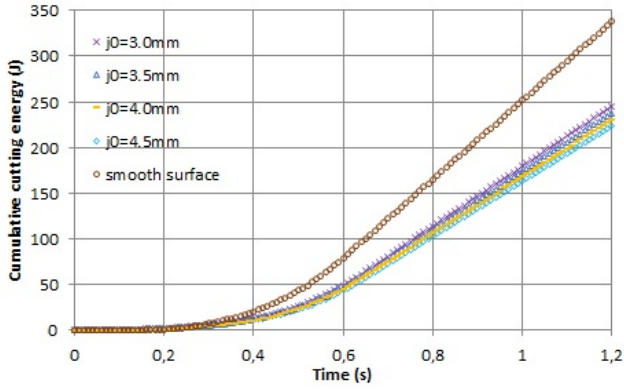
Figure 7.19: Cumulative cutting energy with respect to ridge height j_0 of bionic surfaces and a smooth surface
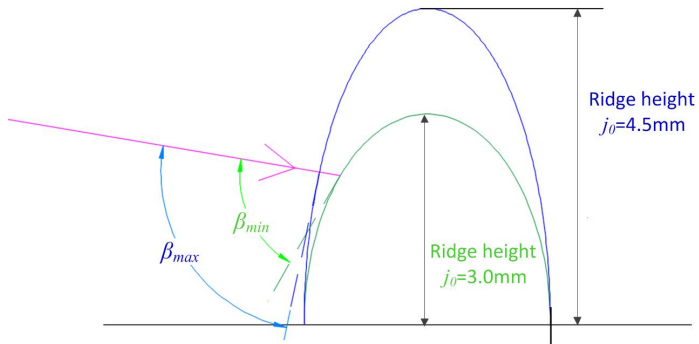
Figure 7.20: Variation of impact angle by increasing ridge height
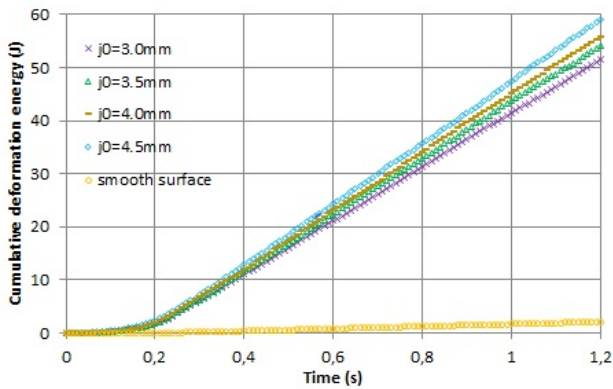
Figure 7.21: Cumulative cutting energy with respect to ridge height j_0 of bionic surfaces and a smooth surface

Figure 7.21 illustrates the cumulative deformation energy with respect to ridge height of the bionic surfaces and a smooth surface. It shows that the cumulative deformation energy shows a steady growth with the variation of the ridge height from 3.0 to 4.5 mm. This is due to the fact that with a decrease of the tangential velocity. The deformation velocity becomes larger and thus the cumulative deformation energy increases.

Using Equation 5.18, the calculated wear volumes for the variation of the ridge height are shown in Figure 7.22. It can be observed that the wear volumes on the bionic surfaces decrease with the increase of ridge height. The minimum wear volume is 1.93 $\times 10^{-5}$ m^3 obtained at the ridge width j_0 = 4.5 mm and the wear volume is reduced by 26%.
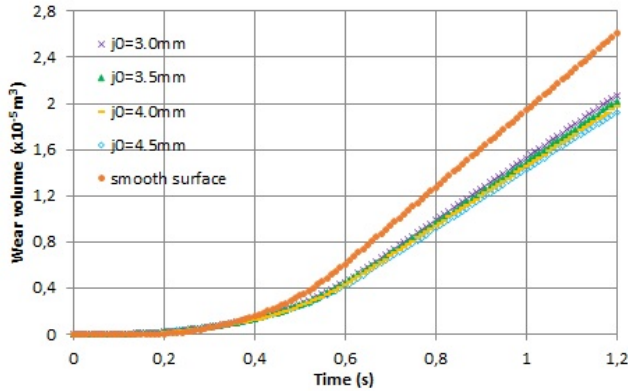
Figure 7.22: Wear volumes as functions of four ridge heights j_0 and a smooth surface

In summary, the sensitivities of geometrical parameters on erosive wear of bionic surfaces are predicted. It was observed that the spike radius (e_0), and the horizontal and vertical distances between spikes (f_0 and g_0) have negligible influences on erosive wear. However, increasing ridge/ridge distance h_0 gives a maximum reduction of wear. The increase of ridge width (i_0) causes a higher wear volume. In addition, increasing ridge height (j_0) decreases wear volume. The maximum reduction of wear (26%) over the tested values (Table 7.3) is achieved from the highest ridge j_0 = 4.5 mm.

7.4 Conclusions

To answer the subquestion of *"What are the effects of applying bionic surfaces on erosive wear reduction?"*, this chapter investigated a bionic model for erosive wear reduction of a chute bottom surface. Four conclusions can be drawn as below.

(1) The DEM simulation model for predicting erosive wear of a curved impact chute is theoretically verified. It can be used for predicting erosive wear in bulk solids handling.

(2) This research demonstrated that by applying the wear reduction mechanism occurring in biology, wear reduction of a chute surface can be achieved.

(3) The effects of geometrical parameters on wear predictions are demonstrated. In addition, it is shown that the maximum reduction of erosive wear that can be achieved from a bionic surface is 26% in comparison to a smooth surface.

(4) This research shows high significance for applying bionic design method to reduce erosive wear in bulk solids handling.

This chapter has demonstrated that bionic design can also be used for the reduction of erosive wear. In the next chapter, the conclusions and recommendations of this thesis are presented.

8 CHAPTER

Conclusions and recommendations

8.1 Conclusions

The main research question of this thesis is *"Can bionic design reduce wear of bulk solids handling equipment surfaces?"*. This question is answered by answering six subquestions:

(1) Which analytical wear models can be used to quantify the surface wear of bulk solids handling equipment?

(2) How to develop a bionic design method to reduce the surface wear of bulk solids handling equipment?

(3) What experiments can be used to determine the DEM parameters for modeling wear in bulk solids handling?

(4) How to predict the surface wear of bulk solids handling equipment by using the DEM simulations?

(5) What are the effects of applying bionic surfaces on abrasive wear reduction?

(6) What are the effects of applying bionic surfaces on erosive wear reduction?

Chapter 2 provided the answers to the first subquestion: *"Which analytical wear models can be used to quantify the surface wear of bulk solids handling equipment?"*

- In bulk solids handling, two main wear types are identified, namely, the abrasive wear and erosive wear. Both wear types generally trigger ductile failures on the ductile and brittle surfaces of bulk solids handling equipment. However, equipment with a brittle surface can also suffer from brittle failures.

- With respect to ductile and brittle surfaces, the equations for quantifying absolute wear by bulk solids are developed on the basis of the absolute wear volume loss for single particle. Wear factors can also be used for comparing wear rates by bulk solids.

- Based on simplifications of the three aspects, namely, particulate solids, equipment surface and wear conditions, the abrasive and erosive wear in bulk solids handling can be theoretically predicted using analytical wear models.

- The parameters for wear equations can be determined by selecting appropriate test apparatuses. Nevertheless, due to disadvantages of wear test apparatuses, discrepancies of parameter determinations by experiments have to be reconciled.

Chapter 3 answered the subquestion on: *"How to develop a bionic design method to reduce the surface wear of bulk solids handling equipment?"*

- The biological morphologies from biological wear-resistant surfaces are non-smooth, which have important effects on the ability of wear reduction. The wear-resistant mechanisms provide possible solutions for surface wear reduction of bulk solids handling equipment.

- The available bionic models used for wear reduction can be analyzed from three aspects: bionic surface, particulate solids and wear conditions. The experimental validations demonstrate that both abrasive and erosive wear reduction can be achieved using biological morphologies.

- The analogies of wear aspects from biology to agricultural and bulk materials handling industries are identified. This indicates significant potential for using bionic design for wear reduction of bulk solids handling equipment surfaces.

- In combination with the analysis of the available bionic design methods, a bionic design method is formulated for the wear reduction of bulk material handling equipment. In addition, two possible bionic models, for reduction of abrasive and erosive wear respectively, are proposed.

Chapter 4 made response on: *"What experiments can be used to determine the DEM parameters for modeling wear in bulk solids handling"*

Mainly three tests were done to determine DEM parameters for modeling wear in bulk solids handling and the findings are:

- The hardness number of Sishen particle varied by measured locations and also by particles. Using a 95% confidence interval, the Vickers hardness number for Sishen particles is determined as: 476 ± 19.

- The average coefficients of sliding wear are determined for particle and mild steel are determined at $\alpha_{s,p} = (8.83 \pm 0.67) \times 10^{-13}$ m^2/N and $\alpha_{s,e} = (2.99 \pm 0.36) \times 10^{-13}$ m^2/N respectively. Furthermore, the sliding wear volumes for particle and mild steel are determined with respect to transient state and steady state.

- The coefficient of sliding friction is varied by particles and distances. In addition, two types of friction characteristics are distinguished: namely, friction increases to a peak value at transient state and friction maintains increasing trend at transient state.

- At an open test environment, the contact temperature rise for single particle sliding is between 1.3 and 2.2^{o}C. This range of temperature rise has no impact on the wear rate.

- The coefficients of static friction for discrete particles and bonded particles are $0.43 \pm 0.01s$ and 0.49 ± 0.03 respectively. It shows that the coefficient of static friction for discrete particles is approximately 14% lower than that of bonded particles.

Chapter 5 answered the subquestion of *"How to predict the surface wear of bulk solids handling equipment by using the DEM simulations? "*

- Using the Hertz-Mindlin no-slip contact model, the sliding wear at steady state for a single particle can be accurately predicted.

- The effects of the selected DEM parameters on the prediction of the wear volume are obtained by conducting a sensitivity study. This provides significant references for modeling the sliding wear in bulk solids handling.

- Using the Hertz-Mindlin no-slip contact model, the DEM predictions are 11% smaller than the theoretical estimation. Under this deviation, the prediction of the corresponding particle impact energy is acceptable.

- The effects of the DEM parameters on the predictions of particle impact energy are revealed. This is useful to the selections of appropriate values for modeling the erosive wear in bulk solids handling.

Chapter 6 replied the subquestion of "What are the effects of bionic surfaces on abrasive wear reduction?

The main findings regarding investigating the wear of bionic surfaces are:

- Using the values determined from experimental tests, the sliding wear at steady state in iron ore handling is accurately predicted.

- In comparison with a conventional smooth surface, the wear reduction of a bionic surface is successfully demonstrated.

- The effects of geometrical parameters on the wear prediction of bionic surface are obtained. It is shown that the maximum reduction of wear achieved is 63% from hemispheric convexes of a bionic surface.

- This research provides significant value for applying bionic design method to reduce abrasive wear in bulk solids handling.

Chapter 7 provided the answer to the last key question: *"What are the effects of bionic surfaces on erosive wear reduction?*

- The DEM simulation model for predicting erosive wear of a curved impact chute is theoretically verified. It can be used for predicting erosive wear in bulk solids handling.

- This research demonstrated that by applying the wear reduction mechanism occurring in biology, wear reduction of a chute surface can be achieved.

- The effects of geometrical parameters on wear predictions are demonstrated. In addition, it is shown that the maximum reduction of erosive wear that can be achieved from a bionic surface is 26% in comparison to a smooth surface.

- This research shows high significance for applying bionic design method to reduce erosive wear in bulk solids handling.

To conclude, bionic design is an innovative method that can be used for surface wear reduction of bulk solids handling equipment.

8.2 Recommendations

To improve this research of applying bionic design for surface wear reduction of bulk solids handling equipment, five recommendations are presented:

(1) The wear predictions as functions of geometrical parameters can be further investigated using increased an range of parameter values. By analyzing the results of wear predictions, an optimal design can be recommended for applications in the bulk solids handling industry.

(2) To improve the outcome of the simulation of the angle of repose Ψ_3, more realistic particle sizes as that of the tested bulk material can be applied. Meanwhile, other contact models such as Linear-Spring-Dashpot (LSD) and Hertz-Mindlin Johnson -Kendall-Roberts (JKR) can be explored.

(3) To improve the prediction of erosive wear, the LSD or Hertz-Mindlin JKR contact model can be investigated. In addition to the verification of the predicted impact forces, it is recommended that the correlation between wear volume and impact energy is determined.

(4) The predicted wear volume is based on the assumption that the coefficient of wear is constant. However, due to the fact that the coefficient of wear changes in practice, the experimental validation on wear prediction is required .

(5) To maintain the biological morphologies during wear processes, a bionic model can be improved by applying different substances to the bionic elements (i.e. convexes, ridges) and the matrix of a wear body. Alternatively, removable bionic elements can be fabricated to replace the worn ones.

A | APPENDIX

Appendix A

For a particle sliding against a ductile surface, the sliding wear volume for a distance l is given by Equation 2.2,

$$W_V = \alpha_{s,e} \cdot F_n \cdot l_s \tag{2.2}$$

Alternatively, the wear volume for the equal wear distance l based on the illustration in Figure 5.5 is give by,

$$W_V = \phi_4 \cdot A_1 \cdot l_s \tag{A.1}$$

in which ϕ_4 is the fraction of material removal from the indented groove; A_0 is the cross-sectional area of indented groove. Combining Equations 2.2 and A.1, it gives

$$\alpha_{s,e} F_n = \phi_4 A_1 \tag{A.2}$$

Then,

$$\alpha_{s,e} = \frac{\phi_4 A_1}{F_n} \tag{A.3}$$

Using Figure 5.5, A_1 is expressed as,

$$A_1 = \frac{\theta_3 r_p^2}{2} - a_1(r_p - \delta_n) \tag{A.4}$$

where θ_4 the indention angle. a_1 is the radius of contact area, which is given by [160],

$$a_1 = \sqrt{r_p \delta_n} \tag{A.5}$$

θ_3 can be obtained from,

$$\sin \frac{\theta_3}{2} = \frac{a_1}{r_p} \tag{A.6}$$

Substituting a_1 by using Equation A.5, Equation A.6 gives,

$$\theta_3 = 2arc\sin\left(\frac{\delta_n}{r_p}\right)^{1/2} \tag{A.7}$$

Using Equations A.5 and A.7, A_1 becomes,

$$A_1 = \left[arc\sin\left(\frac{\delta_n}{r_p}\right)^{1/2} - \left(\frac{\delta_n}{r_p}\right)^{1/2} + \left(\frac{\delta_n}{r_p}\right)^{3/2}\right]r_p^2 \tag{A.8}$$

In combination with the normal force F_n,

$$F_n = \frac{4}{3}E^*r_p^{1/2}\delta_n^{3/2} = \frac{4}{3}E^*\left(\frac{\delta_n}{r_p}\right)^{3/2}r_p^2 \tag{A.9}$$

The coefficient of sliding wear $\alpha_{s,e}$ is then obtained by substituting Equations A.8 and A.9 into Equation A.4.

$$\alpha_{s,e} = \frac{3\phi_4\left[arc\sin\left(\frac{\delta_n}{r_p}\right)^{1/2} - \left(\frac{\delta_n}{r_p}\right)^{1/2} + \left(\frac{\delta_n}{r_p}\right)^{3/2}\right]}{4E^*\left(\frac{\delta_n}{r_p}\right)^{3/2}} \tag{A.10}$$

Noted that Equation A.10 was presented as Equation 5.10 in chapter 5.

Bibliography

[1] Dietmar Schulze. *Powders and bulk solids: behavior, characterization, storage and flow*. Springer Science & Business Media, 2007.

[2] Sishen Iron Ore Company. "kolomela iron ore mine, northern cape, south africa". [Online; http://www.mining-technology.com/projects/kolomela-iron-ore-mine-northern-cape; accessed on Febrary 19, 2016].

[3] Mingming Hu, Stefan Pauliuk, Tao Wang, Gjalt Huppes, Ester van der Voet, and Daniel B Müller. Iron and steel in chinese residential buildings: A dynamic analysis. *Resources, Conservation and Recycling*, 54(9):591–600, 2010.

[4] Alan W Roberts. Chute performance and design for rapid flow conditions. *Chemical engineering & technology*, 26(2):163–170, 2003.

[5] Brian G Mellor. *Surface coatings for protection against wear*. Taylor & Francis US, 2006.

[6] Luquan Ren, Jin Tong, Shujan Zhang, and Bingcong Cheng. Reducing sliding resistance of soil against bulldozing plates by unsmoothed bionics surfaces. *Journal of Terramechanics*, 32(6):303–309, 1995.

[7] Jin Tong, Tie-biao Lü, Yun-hai Ma, Heng-kun Wang, Lu-quan Ren, and RD Arnell. Two-body abrasive wear of the surfaces of pangolin scales. *Journal of Bionic Engineering*, 4(2):77–84, 2007.

[8] Alexander Filippov and Stanislav N Gorb. Frictional-anisotropy-based systems in biology: structural diversity and numerical model. *Scientific reports*, 3, 2013.

[9] Gao Ke, Sun Youhong, Gao Runfeng, Xu Liang, Wang Chuanliu, and Li Yumin. Application and prospect of bionic non-smooth theory in drilling engineering. *Petroleum Exploration and Development*, 36(4):519–541, 2009.

[10] R Arvind Singh and Eui-Sung Yoon. Biomimetics in tribology-recent developments. *Journal of Korean Physical Society*, 52:656, 2008.

[11] Christian Greiner and Michael Schäfer. Bio-inspired scale-like surface textures and their tribological properties. *Bioinspiration & Biomimetics*, 10(4):044001, 2015.

[12] Zhendong Dai, Jin Tong, and Luquan Ren. Researches and developments of biomimetics in tribology. *Chinese Science Bulletin*, 51(22):2681–2689, 2006.

[13] LuQuan Ren. Progress in the bionic study on anti-adhesion and resistance reduction of terrain machines. *Science in China Series E: Technological Sciences*, 52(2):273–284, 2009.

[14] Julian FV Vincent, Olga A Bogatyreva, Nikolaj R Bogatyrev, Adrian Bowyer, and Anja-Karina Pahl. Biomimetics: its practice and theory. *Journal of the Royal Society Interface*, 3(9):471–482, 2006.

[15] LH Shu, K Ueda, I Chiu, and H Cheong. Biologically inspired design. *CIRP Annals-Manufacturing Technology*, 60(2):673–693, 2011.

[16] Mohd Syahrul Hisyam Mohd Sani, Fadhluhartini Muftah, and Tan Cher Siang. Biomimicry engineering: New area of tranformation inspired by the nature. In *Business Engineering and Industrial Applications Colloquium (BEIAC), 2013 IEEE*, pages 477–482. IEEE, 2013.

[17] R Arvind Singh and Eui-Sung Yoon. Friction of chemically and topographically modified si (100) surfaces. *Wear*, 263(7):912–919, 2007.

[18] Meng Zou, Shucai Xu, Cangang Wei, Huixia Wang, and Zhenze Liu. A bionic method for the crashworthiness design of thin-walled structures inspired by bamboo. *Thin-Walled Structures*, 101:222–230, 2016.

[19] LQ Ren, ZW Han, JQ Li, and Jin Tong. Experimental investigation of bionic rough curved soil cutting blade surface to reduce soil adhesion and friction. *Soil and Tillage Research*, 85(1):1–12, 2006.

[20] I.C. Gebeshuber, B.Y. Majlis, and H. Stachelberger. Tribology in biology: Biomimetic studies across dimensions and across fields. *International Journal of Mechanical and Materials Engineering*, 4(3):321–327, 2009. cited By 7.

[21] AW Roberts and SJ Wiche. Prediction of lining wear life of bins and chutes in bulk solids handling operations. *Tribology international*, 26(5):345–351, 1993.

[22] A Jourani and S Bouvier. Friction and wear mechanisms of 316l stainless steel in dry sliding contact: Effect of abrasive particle size. *Tribology Transactions*, 58(1):131–139, 2015.

[23] A Miszewski, S.W Lommen, D.L Schott, and G Lodewijks. Effect of moisture content on the angle of repose of iron ore. In *Proceedings of 7th International Conference on Conveying and Handling of Particulate Solids*, 2012.

[24] KL Johnson. The correlation of indentation experiments. *Journal of the Mechanics and Physics of Solids*, 18(2):115–126, 1970.

[25] GB Stachowiak and GW Stachowiak. The effects of particle characteristics on three-body abrasive wear. *Wear*, 249(3):201–207, 2001.

[26] Tong Deng, Mark S Bingley, and Michael SA Bradley. The influence of particle rotation on the solid particle erosion rate of metals. *Wear*, 256(11):1037–1049, 2004.

[27] R Macchini, MSA Bradley, and T Deng. Influence of particle size, density, particle concentration on bend erosive wear in pneumatic conveyors. *Wear*, 303(1):21–29, 2013.

[28] D Tabor. The hardness of metals, clarendon, 1951.

[29] NB Dube and IM Hutchings. Influence of particle fracture in the high-stress and low-stress abrasive wear of steel. *Wear*, 233:246–256, 1999.

[30] E Bousser, L Martinu, and JE Klemberg-Sapieha. Effect of erodent properties on the solid particle erosion mechanisms of brittle materials. *Journal of Materials Science*, 48(16):5543–5558, 2013.

[31] Martin J Rhodes. *Introduction to particle technology*. John Wiley & Sons, 2008.

[32] Iain Finnie. Erosion of surfaces by solid particles. *Wear*, 3(2):87–103, 1960.

[33] K-H Zum Gahr. *Microstructure and wear of materials*, volume 10. Elsevier, 1987.

[34] Brian Lawn and Rodney Wilshaw. Indentation fracture: principles and applications. *Journal of materials science*, 10(6):1049–1081, 1975.

[35] Hilgraf P. Wear in bulk materials handling. *Bulk Solids Handling*, 27(7):464–477, 2007.

[36] J Halling. Toward a mechanical wear equation. *Journal of Lubrication Technology*, 105(2):212–219, 1983.

[37] JJ Coronado, SA Rodríguez, and Amilton Sinatora. Effect of particle hardness on mild–severe wear transition of hard second phase materials. *Wear*, 301(1):82–88, 2013.

[38] Arthur W Ruff and SM Wiederhorn. Erosion by solid particle impact. Technical report, DTIC Document, 1979.

[39] Kerry Johanson, Chris Eckert, Dev Ghose, Millorad Djomlija, and Mario Hubert. Quantitative measurement of particle segregation mechanisms. *Powder technology*, 159(1):1–12, 2005.

[40] Martina J Baum, Lars Heepe, and Stanislav N Gorb. Friction behavior of a microstructured polymer surface inspired by snake skin. *Beilstein journal of nanotechnology*, 5(1):83–97, 2014.

[41] T Deng, AR Chaudhry, M Patel, I Hutchings, and MSA Bradley. Effect of particle concentration on erosion rate of mild steel bends in a pneumatic conveyor. *Wear*, 258(1):480–487, 2005.

[42] IM Hutchings. Mechanisms of wear in powder technology: a review. *Powder Technology*, 76(1):3–13, 1993.

[43] David A Rigney. *Fundamentals of friction and wear of materials: papers presented at the 1980 ASM Materials Science Seminar, 4-5 October 1980, Pittsburgh, Pennsylvania*. American Society for metals, 1981.

[44] HC Meng and KC Ludema. Wear models and predictive equations: their form and content. *Wear*, 181:443–457, 1995.

[45] LJ Yang. Determination of steady-state adhesive wear rate. *Journal of tribology*, 128(4):725–734, 2006.

[46] JeFoa Archard. Contact and rubbing of flat surfaces. *Journal of applied physics*, 24(8):981–988, 1953.

[47] MS Bingley and S Schnee. A study of the mechanisms of abrasive wear for ductile metals under wet and dry three-body conditions. *Wear*, 258(1):50–61, 2005.

[48] AG Atkins and D Tabor. Plastic indentation in metals with cones. *Journal of the Mechanics and Physics of Solids*, 13(3):149–164, 1965.

[49] AG Evans and To R Wilshaw. Quasi-static solid particle damage in brittle solidsi. observations analysis and implications. *Acta Metallurgica*, 24(10):939–956, 1976.

[50] AG Evans. The science of ceramic machining and surface finishing ii. *Washington (DC). US Government Printing Office*, pages 1–14, 1979.

[51] DB Marshall, BR Lawn, and AG Evans. Elastic/plastic indentation damage in ceramics: the lateral crack system. *Journal of the American Ceramic Society*, 65(11):561–566, 1982.

[52] Aw G EVans and E Arn Charles. Fracture toughness determinations by indentation. *Journal of the American Ceramic society*, 59(7-8):371–372, 1976.

[53] Iain Finnie. The mechanism of erosion of ductile metals. In *3rd US national congress of applied mechanics*, 1958.

[54] I Finne. Some observations on the erosion of ductile materials. *Wear*, 19:81–90, 1972.

[55] I Finnie and DH McFadden. On the velocity dependence of the erosion of ductile metals by solid particles at low angles of incidence. *Wear*, 48(1):181–190, 1978.

[56] JGA Bitter. A study of erosion phenomena part i. *wear*, 6(1):5–21, 1963.

[57] JGA Bitter. A study of erosion phenomena: Part ii. *Wear*, 6(3):169–190, 1963.

[58] JH Neilson and A Gilchrist. Erosion by a stream of solid particles. *Wear*, 11(2):111–122, 1968.

[59] Seiichi Sato, Akihiko Shimizu, and Takehiko Yokomine. Numerical predic-
     tion of erosion for suspension flow duct. *Wear*, 186:203–209, 1995.

[60] DJ OFlynn, MS Bingley, MSA Bradley, and AJ Burnett. A model to predict
     the solid particle erosion rate of metals and its assessment using heat-treated
     steels. *Wear*, 248(1):162–177, 2001.

[61] JG Mbabazi, TJ Sheer, and R Shandu. A model to predict erosion on mild
     steel surfaces impacted by boiler fly ash particles. *Wear*, 257(5):612–624,
     2004.

[62] IM Hutchings. A model for the erosion of metals by spherical particles at
     normal incidence. *Wear*, 70(3):269–281, 1981.

[63] G Sundararajan and PG Shewmon. A new model for the erosion of metals
     at normal incidence. *Wear*, 84(2):237–258, 1983.

[64] Kim Pang, Ahmed Cenna, Shengming Tan, and Mark Jones. Experimental
     determination of cutting and deformation energy factors for wear predic-
     tion of pneumatic conveying pipeline. In *Engineering Asset Lifecycle Manage-
     ment*, pages 877–885. Springer, 2010.

[65] J Li, T Deng, MS Bingley, and MSA Bradley. Prediction of particle rotation in
     a centrifugal accelerator erosion tester and the effect on erosion rate. *Wear*,
     258(1):497–502, 2005.

[66] AA Cenna, NW Page, E Kisi, and MG Jones. Single particle impact tests
     using gas gun and analysis of high strain-rate impact events in ductile ma-
     terials. *Wear*, 271(9):1497–1503, 2011.

[67] Z Korzen. The dynamics of bulk solids flow on impact plates of belt con-
     veyor systems. *Bulk solids handling*, 8(6):689–697, 1988.

[68] ASTM Standard et al. Standard test method for wear testing with a pin-on-
     disk apparatus. *Annual Book of ASTM Standards, G99-05*, 3, 2000.

[69] G ASTM. 99–95a standard test method for wear testing with a pin-on-disk
     apparatus. *ASTM International*, 2000.

[70] AA Cenna, J Doyle, NW Page, A Beehag, and P Dastoor. Wear mechanisms
     in polymer matrix composites abraded by bulk solids. *Wear*, 240(1):207–214,
     2000.

[71] AA Cenna, S Allen, NW Page, and P Dastoor. A polyethylene-reinforced
     polymer composite abraded by bulk solids. *Wear*, 249(8):663–671, 2001.

[72] SJ Wiche, S Keys, and AW Roberts. Abrasion wear tester for bulk solids
     handling applications. *Wear*, 258(1):251–257, 2005.

[73] AJ Burnett, SR De Silva, and Alan R Reed. Comparisons between sand blast
     and centripetal effect accelerator type erosion testers. *Wear*, 186:168–178,
     1995.

[74] T Deng, MS Bingley, MSA Bradley, and SR De Silva. A comparison of the gas-blast and centrifugal-accelerator erosion testers: The influence of particle dynamics. *Wear*, 265(7):945–955, 2008.

[75] Tong Deng, Mark S Bingley, and Mike SA Bradley. Understanding particle dynamics in erosion testersa review of influences of particle movement on erosion test conditions. *Wear*, 267(11):2132–2140, 2009.

[76] T Deng, MSA Bradley, and MS Bingley. An investigation of particle dynamics within a centrifugal accelerator type erosion tester. *Wear*, 247(1):55–65, 2001.

[77] Guangming Chen, Dingena L Schott, and Gabriel Lodewijks. Bionic design methodology for wear reduction of bulk solids handling equipment. *Particulate Science and Technology*, 35(4):p. –, 2017.

[78] A. Chumber. Handling aggressive goods: Using wear resistant linings to ensure material flow and reduce abrasion. *Bulk Solids Handling*, 33(2):32–33, 2013. cited By 0.

[79] P. Hilgraf. Basic principles of wear protection technology for bulk materials (part 1) [grundlagen der verschleischutz-technik fr schttg ter (teil 1)]. *ZKG International*, 62(10):53–63, 2009.

[80] P. Hilgraf. Basic principles of wear protection technology for bulk materials (part 2) [grundlagen der verschlei-bschutztechnik fr schttgter (teil 2)]. *ZKG International*, 62(11):56–72, 2009.

[81] Michael D Bryant, Atul Tewari, and Jau-Wen Lin. Wear rate reductions in carbon brushes, conducting current, and sliding against wavy copper surfaces. *IEEE Transactions on Components, Packaging, and Manufacturing Technology: Part A*, 18(2):375–381, 1995.

[82] Christian Greiner, Tobias Merz, Daniel Braun, Andrea Codrignani, and Franco Magagnato. Optimum dimple diameter for friction reduction with laser surface texturing: the effect of velocity gradient. *Surface Topography: Metrology and Properties*, 3(4):044001, 2015.

[83] Kalpraxis. "economic wear protection for the mining and processing industry worldwide", 2016. [http://www.verstegen.net/grabs/; accessed on Febrary 19, 2016].

[84] Rui ZHANG, Zhi-li LU, and Jian-qiao LI. Abrasive wear of geometrical surface structures of scapharca subcrenata and burnt-end ark against soil. *Advances in Natural Science*, 3(2):213–217, 2010.

[85] XiMei Tian, ZhiWu Han, XiuJuan Li, ZhaoGuo Pu, and LuQuan Ren. Biological coupling anti-wear properties of three typical molluscan shellsscapharca subcrenata, rapana venosa and acanthochiton rubrolineatus. *Science China Technological Sciences*, 53(11):2905–2913, 2010.

[86] Werner Baumgartner, Friederike Saxe, Agnes Weth, David Hajas, Darwin Sigumonrong, Jens Emmerlich, Martin Singheiser, Wolfgang Böhme, and Jochen M Schneider. The sandfish's skin: morphology, chemistry and reconstruction. *Journal of bionic engineering*, 4(1):1–9, 2007.

[87] Zhiwu Han, Junqiu Zhang, Chao Ge, You Lü, Jialian Jiang, Qingping Liu, and Luquan Ren. Anti-erosion function in animals and its biomimetic application. *Journal of Bionic Engineering*, 7:S50–S58, 2010.

[88] Stephanie B Crofts and Adam P Summers. Biomechanics: Swimming in the sahara. *Nature*, 472(7342):177–178, 2011.

[89] Han Zhiwu, Zhang Junqiu, Ge Chao, Wen Li, and Luquan Ren. Erosion resistance of bionic functional surfaces inspired from desert scorpions. *Langmuir*, 28(5):2914–2921, 2012.

[90] He Huang, Yan Zhang, and Luquan Ren. Particle erosion resistance of bionic samples inspired from skin structure of desert lizard, laudakin stoliczkana. *Journal of Bionic Engineering*, 9(4):465–469, 2012.

[91] Jun-qiu Zhang, Zhi-wu Han, Rong-feng Ma, Wei Yin, You Lü, and Lu-quan Ren. Scorpion back inspiring sand-resistant surfaces. *Journal of Central South University*, 20:877–888, 2013.

[92] F Gao, LQ Ren, H Huang, and YL Yu. Biology coupling characteristics of anti-erosive wear of desert lizards skin. *Trans Chin Soc Agr Mach*, 40:180–183, 2009.

[93] Sandboa Sandfisch and Sandschleiche als Vorbild. Tribologie im dünensand.

[94] Ingo Rechenberg and Abdullah Regabi El Khyari. "the sandfish of the sahara: A model for friction and wear reduction". [http://www.bionik.tu-berlin.de/institut/safiengl.htm; accessed on April 11, 2016].

[95] Jacquelyn KS Nagel, Robert L Nagel, Robert B Stone, and Daniel A McAdams. Function-based, biologically inspired concept generation. *AI EDAM*, 24(4):521–535, 2010.

[96] LuQuan Ren and YunHong Liang. Biological couplings: Function, characteristics and implementation mode. *Science China Technological Sciences*, 53(2):379–387, 2010.

[97] Luquan Ren, Zhiwu Han, Jianjiao Li, and Jin Tong. Effects of non-smooth characteristics on bionic bulldozer blades in resistance reduction against soil. *Journal of Terramechanics*, 39(4):221–230, 2002.

[98] Benard Chirende, JianQiao Li, LiGe Wen, and Timothy Emmanuel Simalenga. Effects of bionic non-smooth surface on reducing soil resistance to disc ploughing. *Science China Technological Sciences*, 53(11):2960–2965, 2010.

[99] Jin Tong, Zhihong Zhang, Yunhai Ma, Donghui Chen, Bingyun Jia, and Carlo Menon. Abrasive wear of embossed surfaces with convex domes. *Wear*, 274:196–202, 2012.

[100] BJ RONG. Biomimetic geometrical structure surfaces with anti-abrasion function and their abrasive wear against soil. *Jilin University*, 2008.

[101] Barbara Colombo. Biomimetic design for new technological developments. *Cumulus Working Papers, Helsinki, Finland: University of Art and Design Helsinki*, pages 29–36, 2007.

[102] Michael Helms, Swaroop S Vattam, and Ashok K Goel. Biologically inspired design: process and products. *Design studies*, 30(5):606–622, 2009.

[103] W Junior, A Guanabara, E Silva, and E Platcheck. Proposta de uma metodologia para o desenvolvimento de produtos baseados no estudo da biónica. *Brasília: P&D-Pesquisa e Design*, 2002.

[104] Denis A Coelho and Carlos AM Versos. A comparative analysis of six bionic design methods. *International Journal of Design Engineering*, 4(2):114–131, 2011.

[105] Jens Gramann. *Problemmodelle und Bionik als Methode*. PhD thesis, Universität München, 2004.

[106] Julian Sartori, Ujjwal Pal, and Amaresh Chakrabarti. A methodology for supporting transfer in biomimetic design. *Artificial Intelligence for Engineering Design, Analysis and Manufacturing*, 24(04):483–506, 2010.

[107] Bernd Hill. Goal setting through contradiction analysis in the bionics-oriented construction process. *Creativity and Innovation Management*, 14(1):59–65, 2005.

[108] The Biomimicry Institute. "the power of the biomimicry design spiral". https://biomimicry.org/biomimicry-design-spiral/. Accessed on accessed on March 2, 2017.

[109] Torben A Lenau et al. Biomimetics as a design methodology-possibilities and challenges. In *DS 58-5: Proceedings of ICED 09, the 17th International Conference on Engineering Design, Vol. 5, Design Methods and Tools (pt. 1), Palo Alto, CA, USA, 24.-27.08. 2009*, 2009.

[110] KJ Rossin. Biomimicry: natures design process versus the designers process. *WIT Transactions on Ecology and the Environment*, 138:559–570, 2010.

[111] Sujeet Ganesh Kore, MI Sakri, and LN Karadi. Design and analysis of a machine tool structure based on structural bionics. *International Journal of Mechanical Engineering and Robotics Research*, 3(3):731, 2014.

[112] Genrikh Saulovich Altshuller, Lev Shulyak, and Steven Rodman. *The innovation algorithm: TRIZ, systematic innovation and technical creativity*. Technical Innovation Center, Inc., 1999.

[113] Julian FV Vincent and Darrell L Mann. Systematic technology transfer from biology to engineering. *Philosophical Transactions of the Royal Society of London A: Mathematical, Physical and Engineering Sciences*, 360(1791):159–173, 2002.

[114] Katharina Schild, Cornelius Herstatt, and Christian Lüthje. How to use analogies for breakthrough innovations. Technical report, Working Papers/Technologie-und Innovationsmanagement, Technische Universität Hamburg-Harburg, 2004.

[115] Stephen M Hsu, Yang Jing, Diann Hua, and Huan Zhang. Friction reduction using discrete surface textures: principle and design. *Journal of Physics D: Applied Physics*, 47(33):335307, 2014.

[116] MS Powell, NS Weerasekara, S Cole, RD LaRoche, and J Favier. Dem modelling of liner evolution and its influence on grinding rate in ball mills. *Minerals Engineering*, 24(3):341–351, 2011.

[117] Hossein Ashrafizadeh and Fakhreddin Ashrafizadeh. A numerical 3d simulation for prediction of wear caused by solid particle impact. *Wear*, 276:75–84, 2012.

[118] Guangming Chen, Yueting Liu, Gabriel Lodewijks, and Dingena L Schott. Determination of the coefficient of sliding wear under iron ore handling conditions. *Under review*.

[119] *Micro/macro hardness tester*. Struers, 2016.

[120] CJ Studman, MA Moore, and SE Jones. On the correlation of indentation experiments. *Journal of Physics D: Applied Physics*, 10(6):949, 1977.

[121] Paul C Okonkwo, Georgina Kelly, Bernard F Rolfe, and Michael P Pereira. The effect of sliding speed on the wear of steel–tool steel pairs. *Tribology International*, 97:218–227, 2016.

[122] MATLAB. *version 8.4.0 (R2014b)*. The MathWorks Inc., Natick, Massachusetts, 2014.

[123] G Straffelini, D Trabucco, and A Molinari. Oxidative wear of heat-treated steels. *Wear*, 250(1):485–491, 2001.

[124] M Amiri, MM Khonsari, and S Brahmeshwarkar. On the relationship between wear and thermal response in sliding systems. *Tribology letters*, 38(2):147–154, 2010.

[125] JF Archard. The temperature of rubbing surfaces. *wear*, 2(6):438–455, 1959.

[126] S Lingard. Estimation of flash temperatures in dry sliding. *Proceedings of the Institution of Mechanical Engineers, Part C: Journal of Mechanical Engineering Science*, 198(2):91–97, 1984.

[127] The Engineering ToolBox brown iron ore. http://www.EngineeringToolBox.com. Accessed: 1-10-2016.

[128] Paul C Okonkwo, Georgina Kelly, Bernard F Rolfe, and Michael P Pereira. The effect of temperature on sliding wear of steel-tool steel pairs. *Wear*, 282:22–30, 2012.

[129] Gabriel KP Barrios, Rodrigo M de Carvalho, Arno Kwade, and Luís Marcelo Tavares. Contact parameter estimation for dem simulation of iron ore pellet handling. *Powder technology*, 248:84–93, 2013.

[130] Geoffroy Lumay, Frédéric Boschini, K Traina, S Bontempi, J-C Remy, R Cloots, and N Vandewalle. Measuring the flowing properties of powders and grains. *Powder Technology*, 224:19–27, 2012.

[131] Andrew Grima and Peter Wypych. Effect of particle properties on the discrete element simulation of wall friction. 2013.

[132] Guangming Chen, Dingena Schott, and Gabriel Lodewijks. Sensitivity analysis of dem prediction for sliding wear by single iron ore particle. *Engineering Computations*, 34(6):p. –, 2017.

[133] Peter A Cundall and Otto DL Strack. A discrete numerical model for granular assemblies. *Geotechnique*, 29(1):47–65, 1979.

[134] EDEM Team. *EDEM 2.6 Theory Reference Guide*. DEM Solutions, 2015.

[135] Paul W Cleary. Predicting charge motion, power draw, segregation and wear in ball mills using discrete element methods. *Minerals Engineering*, 11(11):1061–1080, 1998.

[136] Andrew P Grima and Peter W Wypych. Investigation into calibration of discrete element model parameters for scale-up and validation of particle–structure interactions under impact conditions. *Powder Technology*, 212(1):198–209, 2011.

[137] Kevin Francis Malone and Bao Hua Xu. Determination of contact parameters for discrete element method simulations of granular systems. *Particuology*, 6(6):521–528, 2008.

[138] O Baran, A DeGennaro, E RamÃcopyright, and A Wilkinson. Dem simulation of a schulze ring shear tester. In *AIP Conference*, volume 32, pages 0–3, 2013.

[139] KL Johnson, K Kendall, and AD Roberts. Surface energy and the contact of elastic solids. In *Proceedings of the Royal Society of London A: Mathematical, Physical and Engineering Sciences*, volume 324, pages 301–313. The Royal Society, 1971.

[140] Paul W Cleary, Phil Owen, David I Hoyer, and Steve Marshall. Prediction of mill liner shape evolution and changing operational performance during the liner life cycle: Case study of a hicom mill. *International journal for numerical methods in engineering*, 81(9):1157–1179, 2010.

[141] Johnny T Kalala and Michael H Moys. Discrete element method modelling of liner wear in dry ball milling. *Journal of the South African Institute of Mining and Metallurgy*, 104(10):597–602, 2004.

[142] M Rezaeizadeh, M Fooladi, MS Powell, SH Mansouri, and NS Weerasekara. A new predictive model of lifter bar wear in mills. *Minerals engineering*, 23(15):1174–1181, 2010.

[143] Akira Sato, Junya Kano, and Fumio Saito. Analysis of abrasion mechanism of grinding media in a planetary mill with dem simulation. *Advanced Powder Technology*, 21(2):212–216, 2010.

[144] Paul W Cleary, Matthew D Sinnott, and Rob D Morrison. Separation performance of double deck banana screens–part 2: Quantitative predictions. *Minerals Engineering*, 22(14):1230–1244, 2009.

[145] Akbar Jafari and Vahid Saljooghi Nezhad. Employing dem to study the impact of different parameters on the screening efficiency and mesh wear. *Powder Technology*, 297:126–143, 2016.

[146] Liyu Xie, Wenqi Zhong, Hao Zhang, Aibing Yu, Yujun Qian, and Yougong Situ. Wear process during granular flow transportation in conveyor transfer. *Powder Technology*, 288:65–75, 2016.

[147] Hao Zhang, Yuanqiang Tan, Dongmin Yang, Francesc Xavier Trias, Shengqiang Jiang, Yong Sheng, and Assensi Oliva. Numerical investigation of the location of maximum erosive wear damage in elbow: Effect of slurry velocity, bend orientation and angle of elbow. *Powder Technology*, 217:467–476, 2012.

[148] Stef Willem LOMMEN. Virtual prototyping of grabs. 2016.

[149] *EDEM 2.7*. DEM Solutions, 2016.

[150] C Thornton. Interparticle sliding in the presence of adhesion. *Journal of Physics D: Applied Physics*, 24(11):1942, 1991.

[151] KL Johnson. 1985, contact mechanics, cambridge university press, cambridge, uk.

[152] Junya KANO, Eiki KASAI, Fumio SAITO, and Takazo KAWAGUCHI. Numerical simulation model for granulation kinetics of iron ores. *ISIJ international*, 45(4):500–505, 2005.

[153] DEM Solutions. *EDEM 2.6 Programming Guide*. DEM Solutions, 2015.

[154] A Minoru and O Yasuo. Determination of young's modulus and poisson ratio of lump ores. *Tetsu-to-Hagane*, 69(7):739–745, 1983.

[155] DJC Taylor, DC Page, and P Geldenhuys. Iron and steel in south africa. *J. S. Afr. Inst. Min. Metall.*, 88(3):73–95, 1988.

[156] George E Dieter. Jr.: Mechanical metallurgy, 1961.

[157] Nicholas J Brown, Jian-Fei Chen, and Jin Y Ooi. A bond model for dem simulation of cementitious materials and deformable structures. *Granular Matter*, 16(3):299–311, 2014.

[158] *ANSYS Workbench 16.2*. ANSYS Inc., 2015.

[159] Shane E Flores, Michael G Pontin, and Frank W Zok. Scratching of elastic/plastic materials with hard spherical indenters. *Journal of Applied mechanics*, 75(6):061021, 2008.

[160] Valentin Popov. *Contact mechanics and friction: physical principles and applications*. Springer Science & Business Media, 2010.

[161] DEM Solutions. *EDEM 2.6 User Guide*. DEM Solutions, 2015.

[162] Fan Li, Jingzhe Pan, and Csaba Sinka. Contact laws between solid particles. *Journal of the Mechanics and Physics of Solids*, 57(8):1194–1208, 2009.

[163] Guangming Chen, Dingena L. Schott, and Gabriel Lodewijks. Numerical investigation of a bionic model for abrasive wear reduction of bulk-solids-handling equipment. In *Proceedings of the 5th International Conference of Bionic Engineering*, pages 1–15. International Society of Bionic Engineering (ISBE), 2016.

[164] YC Zhou, BH Xu, AB Yu, and P Zulli. An experimental and numerical study of the angle of repose of coarse spheres. *Powder technology*, 125(1):45–54, 2002.

[165] Z Yan, SK Wilkinson, EH Stitt, and M Marigo. Discrete element modelling (dem) input parameters: understanding their impact on model predictions using statistical analysis. *Computational Particle Mechanics*, 2(3):283–299, 2015.

[166] D Geldart, EC Abdullah, A Hassanpour, LC Nwoke, and I Wouters. Characterization of powder flowability using measurement of angle of repose. *China Particuology*, 4(03n04):104–107, 2006.

[167] Pascale C Rousé. Comparison of methods for the measurement of the angle of repose of granular materials. 2013.

[168] Scribd: Overview of materials for acrylic. `https://www.scribd.com/doc/8637812/Acrylic-Material-Data-from-PARSGLASS`. Accessed: 17-10-2016.

[169] Sayed M Derakhshani, Dingena L Schott, and Gabriel Lodewijks. Calibrating the microscopic properties of quartz sand with coupled cfd-dem framework. *Engineering Computations*, 33(4):1141–1160, 2016.

[170] Rui Zhang, Bin Chen, Jian-qiao Li, and Shu-cai Xu. Dem simulation of clod crushing by bionic bulldozing plate. *Journal of Bionic Engineering*, 5:72–78, 2008.

Nomenclature

Latin letters

$a_0 - j_0$	geometrical parameters of bionic models [m]
a_1	radius of the contact area [m]
b_1	height of bulk solids on loading chute [m]
b_2	height of bulk solids on conveying belt [m]
c_l	half crack length [m]
d_a	Arithmetic mean of the two diagonals (d_1, d_2) [m]
d_g	maximum face size of geometry mesh [m]
d_{50}	the median diameter of bulk solids [m]
d_p	Ferret's diameter of a particle [m]
e	coefficient of restitution [–]
e_1	eccentricity caused from the tilting conveyor [m]
e_2	horizontal distance between the two centers of pulley and arc of the curved impact chute [m]
e_3	vertical distance between the two centers of pulley and arc of the curved impact chute [m]
$f_{a,s}$	abrasive factor for straight surface [m/s]
$f_{a,c}$	abrasive factor for chutes [N/(m× s)]
$f_{e,b}$	factor of erosive wear [N/(m× s)]
g	gravitational acceleration [m/s^2]
g_i	gravitational acceleration for the verification of particle impact wear [m/s^2]
h_c	contact length between particle and equipment surface [m]
h_s	specific heat [J/(Kg ×^{o}C)]
$h_1 - h_4$	dimensions of the transfer equipment for studying abrasive wear [m]
h_5	height of the side of curved impact chute [m]

h_6	a dimension for the setup of impact chute [m]
k_0	a constant in Neilson and Gilchrist's equation [–]
k	conductivity [W/(m $\times^o$C)]
$l_1 - l_2$	horizontal distances for the feeder and the acceleration belt [m]
l_3	horizontal distance that bulk solids travel before impact
l_r	rolling distance [m]
l_s	sliding distance [m]
$l_{s,s}$	sliding distance for steady-state [m]
$l_{s,t}$	sliding distance for transient-state [m]
m	mass [kg]
q_b	bulk flow rate [kg/s]
r_0	rotating radius [m]
r_1, r_2	pulley radii [m]
r_p	radius of particle [m]
s_1	horizontal distance for the bulk solids feeder [m]
s_2	length between chute side and chute bottom [m]
t	time [s]
t_c	contact time [s]
t_R	Rayleigh time step [s]
v_0	initial velocity of bulk solids at the inlet of transfer chute [m/s]
v_a	average bulk flow velocity at the curved part of the transfer chute [m/s]
v_e	maximum particle velocity at which the impact is still purely elastic [m/s]
v_p	particle impact velocity [m/s]
v_r	residual parallel component of particle velocity at small angles of attack [m/s]
v_s	relative sliding velocity of bulk solids with respect to equipment [m/s]
v_t	tangential velocity of an impacting particle [m/s]
v_x	relative bulk velocity in horizontal direction [m/s]
v_y	relative bulk velocity in vertical direction [m/s]
x	displacement of particle in x-axial direction [m]
x_t	cutting length in cutting wear model of ductile failure [m]
y	displacement of particle in y-axial direction [m]
y_t	cutting depth in cutting wear model of ductile failure [m]

z_1 indentation depth under a conical particle tip [m]

z_2 cracking depth of brittle failure [m]

A_0 constant in the equation for calculating transient wear [m^3]

A_1 area of cross section by spherical particle indentation [m^2]

A_2 real loss of area from displace groove for one revolution [m^2]

A_3 real loss of area from displace groove for N_r revolutions [m^2]

A_b wear area by the bulks solids in contact with equipment surface [m^2]

A_n circle contact area of single particle in contact with equipment surface [m^2]

B_0 constant in the equation for calculating transient wear [–]

B_1 chute bottom width [m]

B_c chute width [m]

C_0 ratio of the vertical force to the horizontal force [–]

C_1 empirical constant which is defined as the fraction of particles cutting in an idealized manner

C_2 constant in Bitter's cutting wear equation [m$^{3/2}$ × $s^{1/2}$/N]

C_3 constant in Bitter's cutting wear equation [m$^{1/2}$/s$^{1/2}$]

D damping coefficients [s × N/m]

E Young's modulus of equipment surface [Pa]

E_k kinetic energy [J]

F total force applied by bulk solids [N]

F_n normal force [N]

$F_{n,C}$ The critical value of normal force that triggers a brittle fracture [dimensionless]

F_p load applied on a test surface [N]

F_D drag force in the chute flow model [N]

F_N normal force applied by bulk solids [N]

F_T tangential force applied by bulk solids [N]

$F_N^{'}$ reaction force with respect to the normal force in chute flow model [N]

G shear modulus [Pa]

H hardness [GPa]

H_v Vickers hardness number [–]

I_p moment of inertia of impacting particle [kg× m^2]

J_n	normal acceleration of bulk material to contact of the transfer chute surface [m/s^2]
K_e	kinetic energy [J]
K_I	stress intensity factor [Pa $\times$ m$^{1/2}$]
$K_{I,C}$	critical fracture toughness in model I [Pa $\times$ m$^{1/2}$]
L	particle cutting width [m]
M	torque acts on a impact particle [N $\times$ m]
N_c	cumulative circles of particle indentations [–]
N_i	number of indentations per particle perimeter [–]
N_p	number of particles with contact of equipment surface [–]
N_r	number of wear revolutions in a pin-on-disk test [–]
P_1	contact pressure in Archard wear model [P$_a$]
P_2	contact pressure for a conical tip indentation [P$_a$]
$\bar{P}$	average pressure on equipment surface [P$_a$]
P_h	horizontal component of the contact pressure [P$_a$]
P_m	maximum indentation pressure by spherical particle [P$_a$]
$Q_{q_b,s}$	sliding wear rate by bulk solids [m^3/s]
$Q_{q_b,e}$	erosive wear rate by bulk solids [m^3/s]
R_0	radius of pulley [m]
R_1	radius of curved chute for accelerating bulk solids [m]
R_2	radius of curved impact chute [m]
R_3	radius of pulley near the point of discharging bulk solids [m]
S	stiffness [N/m]
T	temperature [^{o}C]
T_0	parameter for evaluating temperature [^{o}C]
T_d	temperature increase for disk assuming all generated heat flow into disk [^{o}C]
U_r	heat generation rate [J/(s$\times$ m^2)]
$W_{\Delta m_b,s}$	wear volume on the chute surface by the sliding of element mass [m^3]
W_M	wear loss in mass [kg]
W_r	ratio of wear reduction [–]
W_V	wear loss in volume [m^3]
Y_e	elastic load limit [Pa]
Z_s	width of simulation domain [m]

Greek letters

$\alpha_{s,e}$	overall coefficient of sliding wear of equipment surface [m²/N]
$\alpha_{s,p}$	overall coefficient of sliding wear of particle [m²/N]
β	angle of particle impact [^{o}]
β_0	critical value that determines a low or a high impact angle [^{o}]
γ_1	angle between the side and the bottom of loading chute [^{o}]
γ_2	angle between the side and the bottom of impact chute [^{o}]
δ	overlap of indentation depth [m]
ϵ_C	critical plastic strain [–]
ϵ_P	mean plastic strain per particle indentation [–]
$\zeta(\beta)$	function of impact angle [m/N]
η_0	material dependency of the efficiency of material removal [–]
η_1	overall coefficient of the erosive wear in the equation derived by Mbabazi, et al. [–]
η_2	overall coefficient of the erosive wear in the equation derived by Hutchings [–]
η_3	ratio of the volume of material which is plastically strained by each particle impact [–]
θ_1	semi-angle of conical particle tip [^{o}]
θ_2	angle between the directions of the tangent line at the intersection of particle impact and the gravity [^{o}]
θ_3	angle in regard to the chord geometry of particle indentation model [^{o}]
θ_a	average value of chute slope angle measured from the gravitational direction [^{o}]
θ_L	angle between directions of tangential velocity of bulk solids and gravity in chute flow model [rad]
$\theta_{L,0}$	angle between direction of initial velocity v_0 of bulk solids and gravity in chute flow model [rad]
$\theta_{L,m}$	angle between direction of outlet velocity of bulk solids and gravity in chute flow model [rad]
θ_w	wall friction angle [^{o}]
κ_1	coefficient of sliding wear by single particle with respect to ductile failure

	[–]
κ_2	coefficient of rolling wear by single particle with respect to ductile failure [–]
κ_c	a constant for the cutting mechanism in the erosive wear equation from O′Flynn et al. [–]
κ_d	a constant for the lip or platelet formation mechanism in the erosive wear equation from O′Flynn et al. [–]
λ_i	coefficient of sliding wear by single particle with respect to brittle failure [–]
μ_b	coefficient of friction between bulk solid and an equipment surface [–]
μ_e	equivalent friction factor that adopts coefficient of friction [–]
μ_s	sliding friction between Sishen and steel [–]
μ_{st}	static friction between Sishen and steel [–]
ν	Poisson′s ratio [–]
$\xi(\Pi)$	function of parameter Π [–]
ρ_b	the density of bulk solids [kg/m³]
ρ_p	the density of a particle [kg/m³]
ρ_e	the density of equipment surface [kg/m³]
σ_e	normal pressure on equipment surface [kPa]
σ_l	linear wear factor [GPa]
τ_0	inclining angle of discharging belt [^{o}]
υ	power exponent for estimating fatigue failure [–]
ϕ_1	fraction of material removal with respect to displaced volume in Archard′ model [–]
ϕ_2	fraction of material removal with respect to displaced volume by conical particle tip [–]
ϕ_3	fraction of material removal with respect to indentation volume by conical particle tip [–]
ϕ_4	fraction of material removal with respect to indentation volume by spherical particle tip [–]
χ_j	overall coefficient in the equation of erosive wear of brittle failure [–]
ψ	ratio of the length of contact to the cutting depth [–]
ϖ	pressure ratio [–]
ω_d	rotating velocity of disk [^{o}/s]

ω_p	rotating velocity of particle [^{o}/s]
ω_s	rotating velocity of inclining surface [$^o/s$]
ε_c	cutting wear factor [m^3/J]
ε_d	deformation wear factor [m^3/J]
φ	angle of particle rotation during a particle impact [^{o}]
Γ	coefficient for estimating bulk velocity of any chute position when $\theta_{L,0} \neq 0$ [m^2/s^2]
Π	parameter for temperature evaluation [–]
Φ	chute cutting angle [^{o}]
Ψ	slope angles in modeling iron ore bulk flow behaviors [^{o}]
Λ	coefficient to relate cutting factor and deformation factor [–]
Ω	coefficient for calculating lower shear modulus [–]

Superscripts

r	relative
$*$	equivalent

Subscripts

b	bulk solids
e	equipment surface
max	maximum value
min	minimum value
n	normal
p	particle
t	tangential

Acknowledgments

Doing a PhD research abroad was my biggest dream. This is not only because I can work with people from different education background, but also I can widen my views on different cultures. I was so excited when received the admission letter by my supervisors Dr. Dingena Schott and Professor Gabriel Lodewijks. I am indebted to my daily supervisor Dingena and my promoter Gabriel for providing me such precious experience and putting lots of efforts on my PhD research.

During years of my PhD research, Dingena spent quite much time on discussing research questions with me. Also, she used her much time to read my papers. To help me submit a paper in time, she read and corrected my papers in evenings and weekends. Thus I am really thankful for her help.

Besides Dingena's efforts on helping me make progress on my research, she also put energy to encourage me and increase my work efficiency. Furthermore, she provides me opportunities as teaching assistance to build my confidence in interpreting my research. Last but not least, she organized some activities for us to relax and interact with each other out of university environment.

I own a lot to my supervisor Dingena. I will remember the valuable research experience under her supervision, and I sincerely wish her a happy life.

Secondly, I must definitely acknowledge my promoter Prof. Gabriel Lodewijks. He is open to everyone and ready to help us and spare some time for us from his intensive schedule. He enjoys the time with us not only in offices or classrooms, but also at other networking occasions. He is such a kind person whom you can always turn to. I am proud of being one of his PhD students.

Over my PhD years, Gabriel put a lot of energy on developing my research quali-

ties. He also carefully did a lot of corrections on my papers. During our meetings, he gave me constructive suggestions and enlightened me to reflect my research. From time to time, he also kindly pushed and encouraged me to strive for my research targets.

I am also grateful that Gabriel continues to help me on finishing my PhD after he began his work in Australia. I heartily wish him many new friends and nice experience for his new career.

Apart from my supervisors, I am eager to express my thanks to my most important officemate Kanu Jain. He helped me a lot to overcome difficult situations over the three years that we have shared the same office. He is always ready to listen what I want to say and provide me help. He gave me so many important suggestions which helps me move forward on my research and also my life. I am so lucky I have such a nice officemate for three years.

I hope my officemate and also a close friend Kanu would have a very good future, and wish him a very happy life.

In addition, I want to thank my other officemates Maria, Marcela, Mashoud, Peijuan and Breno for the enjoyable time of sharing the same office.

I should specially express my acknowledgments to the colleagues and friends, Stef, Jianbin, Francesco, Victoria, Daijie, Qinqin, Huy, Elena, Xiangwei, Dick, Xiao, Wenbin, Wenjing, Ali, Rudy, Yusong, Jozephina, Patty, Dineke, Freek and Ed.

Hereby I would thank these people who helped me on my research: Zilong, Tao Zou, Tao Lv, Jie, Mukunda, Yueting, Sander, Ankit, Jun, Baris, Ershad, Dave and Alfareeq.

During my PhD years, I must remember the friends who encouraged me: Guangwu, Qujiang, Fulin, Haojie, Cong, Yue, Victor, Morgen, Karina, Xuelei, Xing, Henk, Avin, Waltraut, Ashish, Arun and many others I forget their names.

Finally, I will express my thanks to my family: my father and mother, my brother and sister.

Guangming Chen

6th June. 2017

Curriculum Vitae

Guangming Chen did his bachelor study (BSc) on Mechanical Engineering and Automation in the Jilin University of China from September 2005 to June 2009. He did his master study (MSc) of Agricultural mechanization Engineering from September 2009 to June 2012 in the Key Laboratory of Bionic Engineering (Jilin University), Ministry of Education, China.

He was granted TU Delft/CSC Scholarship for doctoral research in May 2012. From September, he started doctoral research at the Section of Transport Engineering and Logistics, Faculty of Mechanical, Maritime and Materials Engineering, Delft University of Technology, the Netherlands.

His research interest is discrete element method, bionic design, wear modeling and wear reduction.

Publications

- Journal papers

Guangming Chen, Dingena L. Schott, and Gabriel Lodewijks. "Tensile test simulation of high-carbon steel by discrete element method." *Engineering Computations* 33.4 (2016): 1224-1245.

Guangming Chen, Dingena L. Schott, and Gabriel Lodewijks. "Bionic design methodology for wear reduction of bulk solids handling equipment." *Particulate Science and Technology* 35.4. p.- (2017).

Guangming Chen, Dingena L. Schott, and Gabriel Lodewijks. "Sensitivity analysis of DEM prediction for sliding wear by iron ore particle." *Engineering Computations* 34.6. p.- (2017).

Guangming Chen, Yueting Liu, Gabriel Lodewijks and Dingena L. Schott. "Determination of the coefficient of sliding wear under iron ore solids handling conditions." Under review.

- Conference papers

Guangming Chen, Dingena L. Schott, and Gabriel Lodewijks. " Theoretical study of bionic design on wear reduction of bulk materials handling equipment." The 8th International Conference for Conveying and Handling of Particulate Solids (2015): Tel-Aviv, Israel.

Guangming Chen, Dingena L. Schott, and Gabriel Lodewijks. " Predicting the sliding wear of mild steel by iron ore particle using discrete element method simulation." Joint Conference of 5th UK-China and 13th UK Particle Technology Forum (2015): Leeds, UK.

Guangming Chen, Dingena L. Schott, and Gabriel Lodewijks. " Numerical investigation of a bionic model for abrasive wear reduction of bulk-solids-handling equipment." International Conference of Bionic Engineering (2016): Ningbo, China.

TRAIL Thesis Series

The following list contains the most recent dissertations in the TRAIL Thesis Series. For a complete overview of more than 150 titles see the TRAIL website: www.rsTRAIL.nl.

The TRAIL Thesis Series is a series of the Netherlands TRAIL Research School on transport, infrastructure and logistics.

Chen, G., *Surface Wear Reduction of Bulk Solids Handling Equipment Using Bionic Design*, T2017/8, June 2017, TRAIL Thesis Series, the Netherlands

Kurapati, S., *Situation Awareness for Socio Technical Systems: A simulation gaming study in intermodal transport operations*, T2017/7, June 2017, TRAIL Thesis Series, the Netherlands

Jamshidnejad, A., *Efficient Predictive Model-Based and Fuzzy Control for Green Urban Mobility*, T2017/6, June 2017, TRAIL Thesis Series, the Netherlands

Araghi, Y., *Consumer Heterogeneity, Transport and the Environment*, T2017/5, May 2017, TRAIL Thesis Series, the Netherlands

Kasraian Moghaddam, D., *Transport Networks, Land Use and Travel Behaviour: A long term investigation*, T2017/4, May 2017, TRAIL Thesis Series, the Netherlands

Smits, E.-S., *Strategic Network Modelling for Passenger Transport Pricing*, T2017/3, May 2017, TRAIL Thesis Series, the Netherlands

Tasseron, G., *Bottom-Up Information Provision in Urban Parking: An in-depth analysis of impacts on parking dynamics*, T2017/2, March 2017, TRAIL Thesis Series, the Netherlands

Halim, R.A., *Strategic Modeling of Global Container Transport Networks: Exploring the future of port-hinterland and maritime container transport networks*, T2017/1, March 2017, TRAIL Thesis Series, the Netherlands

Olde Keizer, M.C.A., *Condition-Based Maintenance for Complex Systems: Coordinating maintenance and logistics planning for the process industries*, T2016/26, December 2016, TRAIL Thesis Series, the Netherlands

Zheng, H., *Coordination of Waterborn AGVs*, T2016/25, December 2016, TRAIL Thesis Series, the Netherlands

Yuan, K., *Capacity Drop on Freeways: Traffic dynamics, theory and Modeling*, T2016/24, December 2016, TRAIL Thesis Series, the Netherlands

Li, S., *Coordinated Planning of Inland Vessels for Large Seaports*, T2016/23, December 2016, TRAIL Thesis Series, the Netherlands

Berg, M. van den, *The Influence of Herding on Departure Choice in Case of Evacuation: Design and analysis of a serious gaming experimental set-up*, T2016/22, December 2016, TRAIL Thesis Series, the Netherlands

Luo, R., *Multi-Agent Control of urban Transportation Networks and of Hybrid Systems with Limited Information Sharing*, T2016/21, November 2016, TRAIL Thesis Series, the Netherlands

Campanella, M., *Microscopic Modelling of Walking Behavior*, T2016/20, November 2016, TRAIL Thesis Series, the Netherlands

Horst, M. van der, *Coordination in Hinterland Chains: An institutional analysis of port-related transport*, T2016/19, November 2016, TRAIL Thesis Series, the Netherlands

Beukenkamp, W., *Securing Safety: Resilience time as a hidden critical factor*, T2016/18, October 2016, TRAIL Thesis Series, the Netherlands

Mingardo, G., *Articles on Parking Policy*, T2016/17, October 2016, TRAIL Thesis Series, the Netherlands

Duives, D.C., *Analysis and Modelling of Pedestrian Movement Dynamics at Large-scale Events*, T2016/16, October 2016, TRAIL Thesis Series, the Netherlands

Wan Ahmad, W.N.K., *Contextual Factors of Sustainable Supply Chain Management Practices in the Oil and Gas Industry*, T2016/15, September 2016, TRAIL Thesis Series, the Netherlands.